Investigation of the Gas Dispersion and Mixing Characteristics in Column Flotation using Computational Fluid Dynamics (CFD)

by

Ikukumbuta Mwandawande

Dissertation presented for the Degree

of

DOCTOR OF PHILOSOPHY

(Extractive Metallurgical Engineering)

in the Faculty of Engineering

at Stellenbosch University

Supervisor

Prof. G. Akdogan

Co-Supervisor

Prof. S.M. Bradshaw

March 2016

Declaration

By submitting this dissertation electronically, I declare that the entirety of the work contained therein is my own, original work, that I am the sole author thereof (save to the extent explicitly otherwise stated), that reproduction and publication thereof by Stellenbosch University will not infringe any third party rights and that I have not previously in its entirety or in part submitted it for obtaining any qualification.

Date: March 2016

Abstract

In this thesis, Computational Fluid Dynamics (CFD) was applied to study gas dispersion and mixing characteristics of industrial and pilot scale flotation columns. An Eulerian-Eulerian multiphase modelling approach with appropriate interphase momentum exchange terms was applied to simulate the multiphase flow inside the column while turbulence in the continuous phase was modelled using the k-ϵ realizable turbulence model. The CFD simulations in this research were performed using the Ansys Fluent 14.5 CFD solver.

In the first part of the research, CFD was used to predict the average gas holdup and the axial gas holdup variation in the collection zone of a 0.91 m diameter pilot flotation column operated in batch mode. The axial gas holdup profile was achieved in the simulations using the Ideal Gas law to impose compressibility effects on the air bubbles. With mean absolute relative error (MARE) ranging from 6.2 to 10.8%, the predicted average gas holdup values were in good agreement with experimental data. The axial gas holdup prediction was generally good for the middle and top parts of the column where the mean absolute relative error values were less than 10% while the gas holdup was over-predicted for the bottom part of the column (MARE exceeding 20%), especially at lower superficial gas velocities. The axial velocity of the air bubbles decreased with height along the column. The axial decrease in the bubble velocity may be due to the increase in the drag force resulting from the upward increase in gas holdup in the column. Simulations were also conducted to compare the gas holdup predicted with three different drag models, the Universal drag coefficient, the Schiller-Naumann, and the Morsi-Alexander drag models. The gas holdup predictions for the three drag models were not significantly different.

Flotation columns are known for their improved metallurgical performance compared to conventional flotation cells. However, increased mixing in the column can adversely affect its grade/recovery performance. In the second part of this research, the mixing characteristics of the collection zone of industrial flotation columns were investigated using CFD. Liquid and particle residence time distribution (RTD) data were computed from CFD simulations and subsequently used to determine the mixing parameters (the mean residence time and the vessel dispersion number). Liquid RTD was modelled using the Species Model available in Ansys Fluent while the particle RTD was modelled using a user defined scalar (UDS) transport equation that computes the age of the particles in the column. The mean residence time of particles in the column was well predicted with a mean absolute relative error equal to

7.8%. The results obtained showed that particle residence time decreases with increasing particle size. The residence time of the coarser particles (125 µm) was found to be about 50% of the liquid residence time while the finer particles (44 µm) had residence time similar to the liquid one. These findings are in agreement with experimental data available in the literature. The relationship between the liquid and solids axial dispersion coefficients was also investigated by comparing the water and the solids flow patterns. The flow patterns between the phases revealed that their dispersion coefficients were similar. In addition, the effects of the bubble size and particle size of the solids on the liquid dispersion were investigated. It was found that increasing particle size of the solids resulted in a decrease in the liquid vessel dispersion number. On the other hand, a decrease in the bubble size caused a significant increase in the liquid vessel dispersion number.

Flotation columns are normally operated at optimal superficial gas velocities to maintain bubbly flow conditions. However, with increasing superficial gas velocity, loss of bubbly flow may occur with adverse effects on column performance. It is therefore important to identify the maximum superficial gas velocity above which loss of bubbly flow occurs. The maximum superficial gas velocity is usually obtained from a gas holdup versus superficial gas velocity plot in which the linear portion of the graph represents bubbly flow while deviation from the linear relationship indicates a change from the bubbly flow to the churn-turbulent regime. However, this method is difficult to use when the transition from bubbly flow to churn-turbulent flow is gradual as happens in the presence of frothers. Two alternative methods are presented in the final part of the present research in which the flow regime prevailing in the column is related to radial gas holdup profiles and gas holdup versus time plots obtained from CFD simulations. The results showed that radial gas holdup profiles can be used to distinguish bubbly flow (saddle shaped gas holdup profiles) from churn turbulent flow (steep parabolic gas holdup profiles). However, the transitional regime between these two extremes was difficult to characterize due to its gradual nature. Another important finding of this research was that different radial gas holdup profiles could result in opposite liquid flow patterns. For example, a liquid circulation pattern with upward flow in the centre and downward flow near the column walls was always present when the radial gas holdup profile is parabolic. On the other hand, an inverse flow pattern was observed in which the liquid rises near the column wall but descends in the centre and adjacent to the wall. This profile was accompanied by corresponding saddle shaped radial gas holdup profiles.

Opsomming

In hierdie tesis word berekeningsvloeidinamika (CFD) gebruik om die gasdispersie- en vermengingskenmerke van flottasiekolomme op industriële en proefskaal te bestudeer. 'n Meerfasige Euler-Euler-modelleringsbenadering met toepaslike momentumuitruiling tussen fases is gebruik om die meerfasige vloei in die kolom te simuleer. Die turbulensie in die kontinue fase is op sy beurt met die realiseerbare k-ε-turbulensiemodel gemodelleer. Die CFD-simulasies in hierdie navorsing is met behulp van die CFD-oplossingsagteware Ansys Fluent 14.5 uitgevoer.

In die eerste deel van die navorsing is CFD gebruik om die gemiddelde en aksiale gasvasvangingsvariasie te voorspel in die versamelsone van 'n proefflottasiekolom met 'n deursnee van 0,91 m wat in lotte bedryf word. Die aksiale gasvasvangingsprofiel in die simulasies is verkry deur van die idealegaswet gebruik te maak om 'n saamdrukbaarheidseffek op die lugborrels uit te oefen. Met 'n gemiddelde absolute relatiewe afwykingswaarde (MARE) van tussen 6.2 en 10.8% het die voorspelde gemiddelde gasvasvangingswaardes sterk ooreenkomste met die eksperimentele data getoon. Die voorspelde aksiale gasvasvangingswaardes was oor die algemeen goed vir die middelste en boonste dele van die kolom, waar die gemiddelde absolute relatiewe afwykingswaardes minder as 10% was. Tog was die voorspelde gasvasvangingswaardes vir die onderste gedeelte van die kolom te hoog (met 'n MARE van meer as 20%), veral teen laer oppervlakkige gassnelhede. Die aksiale snelheid van die lugborrels het afgeneem namate dit hoër op in die kolom beweeg het. Dié aksiale afname in borrelsnelheid kan moontlik toegeskryf word aan die toename in sleurkrag vanweë die verhoogde gasvasvanging hoër op in die kolom. Daar is ook simulasies gedoen om die voorspelde gasvasvangingswaardes met drie verskillende sleurmodelle, naamlik die universele sleurkoëffisiënt, Schiller-Naumann en Morsi-Alexander, te vergelyk. Die voorspelde gasvasvangingswaardes vir die drie sleurmodelle het nie beduidend verskil nie.

Flottasiekolomme is bekend vir hulle beter metallurgiese werkverrigting vergeleke met konvensionele flottasieselle. Tog kan verhoogde vermenging in die kolom 'n negatiewe uitwerking op graad/herwinning hê. In die tweede deel van die navorsing is die vermengingskenmerke in die versamelsone van industriële flottasiekolomme met behulp van CFD ondersoek. Data oor die verblyftydverspreiding (RTD) van vloeistof en deeltjies is op grond van CFD-simulasies bereken en daarná gebruik om die vermengingsparameters

(gemiddelde verblyftyd en houerdispersiewaarde) vas te stel. Die RTD vir vloeistof is gemodelleer met die spesiemodel in die sagteware Ansys Fluent. Die RTD vir deeltjies is op sy beurt met 'n gebruikersomskrewe skalêre (UDS-) vervoervergelyking gemodelleer wat die ouderdom van die deeltjies in die kolom bereken. Die gemiddelde verblyftyd van deeltjies in die kolom is akkuraat voorspel, met 'n gemiddelde absolute relatiewe afwykingswaarde van 7.8%. Die resultate toon dat deeltjieverblyftyd afneem namate deeltjiegrootte toeneem. Die verblyftyd van die growwer deeltjies (125 μm) blyk sowat 50% van die vloeistofverblyftyd te wees, terwyl die verblyftyd van die fyner deeltjies (44 μm) soortgelyk is aan dié van vloeistof. Hierdie bevindinge stem ooreen met die eksperimentele data wat in die literatuur beskikbaar is. Die verwantskap tussen die aksiale dispersiekoëffisiënte vir vloeistof en vaste stowwe is ook ondersoek deur die vloeipatrone van water en vaste stowwe te vergelyk. Die vloeipatrone tussen die fases dui op soortgelyke dispersiekoëffisiënte. Daarbenewens is die uitwerking van die borrelgrootte en deeltjiegrootte van vaste stowwe op vloeistofdispersie ondersoek. Daar is bevind dat 'n toename in die deeltjiegrootte van vaste stowwe 'n afname in die houerdispersiewaarde van vloeistof tot gevolg het. Daarteenoor lei 'n afname in borrelgrootte tot 'n beduidende toename in die houerdispersiewaarde van vloeistof.

Flottasiekolomme word gewoonlik teen optimale oppervlakkige gassnelhede bedryf om borrelvloei-omstandighede te handhaaf. Namate oppervlakkige gassnelheid egter toeneem, kan borrelvloei afneem, wat 'n nadelige uitwerking op die werkverrigting van die kolom kan hê. Daarom is dit belangrik om die maksimum oppervlakkige gassnelheid te bepaal waarbo borrelvloei afneem. Hierdie maksimum oppervlakkige gassnelheid word gewoonlik verkry deur middel van 'n grafiek van gasvasvanging teenoor oppervlakkige gassnelheid, waar die lineêre gedeelte van die grafiek die borrelvloei voorstel, en afwyking van die lineêre verwantskap op 'n verandering van die borrelvloei- na die kolk-turbulente vloeiregime dui. Tog is dit moeilik om hierdie metode te gebruik as die oorgang van borrel- na kolk-turbulente vloei geleidelik plaasvind, soos wanneer daar skuimmiddels betrokke is. In die laaste deel van die navorsing word twee alternatiewe metodes aangebied waarin die heersende vloeiregime in die kolom vergelyk word met die radiale gasvasvangingsprofiele en die gasvasvanging/tyd-grafieke wat uit die CFD-simulasies verkry is. Die resultate toon dat radiale gasvasvangingsprofiele gebruik kan word om borrelvloei (saalvormige gasvasvangingsprofiele) van kolk-turbulente vloei (steil paraboliese gasvasvangingsprofiele) te onderskei. Die oorgangsregime tussen hierdie twee uiterstes was egter moeilik om te tipeer weens die geleidelike aard daarvan. 'n Verdere belangrike bevinding van hierdie navorsing is

dat verskillende radiale gasvasvangingsprofiele tot teenoorgestelde vloeistofvloeipatrone kan lei. 'n Vloeistofsirkulasiepatroon met opwaartse vloei in die middel en afwaartse vloei naby die kolomwande was byvoorbeeld deurentyd teenwoordig toe die radiale gasvasvangingsprofiel parabolies was. Daarteenoor is 'n omgekeerde vloeipatroon waargeneem waarin die vloeistof naby die kolomwand styg, maar in die middel en langs die wand daal, welke profiel met saalvormige radiale gasvasvangingsprofiele gepaardgegaan het.

Acknowledgements

I would like to acknowledge several people who have provided support or advice during the course of my PhD research. First and foremost I would like to acknowledge the Centre for International Cooperation at VU University Amsterdam (CIS-VU) and the Copperbelt University (CBU) for offering me a PhD scholarship through the Nuffic-HEART Project. I would also like to convey my sincere gratitude to my supervisors Professor Guven Akdogan and Professor Steven Bradshaw for their valuable advice and encouragement throughout my research programme.

I would also like to thank my colleagues and fellow research students, Mohsen, Deside, Bawemi, Arthur, Henri, Clyde and Edson for the advice and friendships during my research journey.

My gratitude also goes to Stephan Schmitt and Dawie Marais at Qfinsoft for their willingness to provide advice regarding the ANSYS FLUENT software.

Finally, let me thank my wife Lenny and my son Michael for their valued support, love, understanding and patience.

Dedication

This thesis is dedicated to the late Professor Glasswell Nkonde for supporting me to come and study at Stellenbosch University. May His Soul Rest In Peace.

Table of Contents

List of Figures

List of Tables

Nomenclature

Symbols

C_D	Drag coefficient, dimensionless
D	Axial Dispersion Coefficient
d_b/d_B	Bubble diameter, mm
d_C	Column diameter
$\mathbf{g}$	Gravitational acceleration, 9.81 m/s^2
H	Height, m
J_g	Superficial gas velocity, cm/s
$J_{g,max}$	Maximum superficial gas velocity, cm/s
J_l	Superficial liquid velocity, cm/s
k	Turbulence kinetic energy, m^2/s^2
N_d	Vessel dispersion number, Dimensionless
P	Pressure, Pa
Pe	Peclet number, Dimensionless
R	Universal Gas Constant
Re	Reynolds number, Dimensionless
S_q	Mass source term for phase q, kg/m^3-s
T	Temperature
U	Velocity, m/s
u_i	Interstitial liquid velocity
U_{sb}	Slip velocity or relative velocity between the bubble swarm and the liquid
U_t	Bubble terminal rise velocity
V	Volume, m^3
ΔH	Separation distance for gas holdup measurement
ΔP	Pressure difference

Greek letters

σ_k	Turbulent Prandtl number for turbulence kinetic energy, k
ε	Phase volume fraction (holdup)
ϵ	Turbulence dissipation rate, m^2/s^3
ε_g	Gas holdup
μ	Viscosity, kg/m-s
μ_t	Turbulent viscosity, kg/m-s
ρ	Density, kg/m^3
ρ_{sl}	Slurry density
σ^2	Variance
σ_ϵ	Turbulent Prandtl number for turbulence dissipation rate, ϵ
σ_Θ^2	Relative variance
τ	Mean residence time
$\overline{\overline{\tau q}}$	Stress-strain tensor

Subscripts

B	Bubble
D	Drag
G, g	Gas
i, j	Spatial directions
L, l	Liquid
q	Phase

Abbreviations

ADM	Axial Dispersion Model
CFD	Computational Fluid Dynamics
DNS	Direct Numerical Simulation
DPM	Discrete Phase Model
LES	Large Eddy Simulation
LSTS	Large and Small Tanks in Series
MAC	Marker and Cell
MARE	Mean Absolute Relative Error

PDE	Partial Differential Equation
QUICK	Quadratic Upstream Interpolation for Convective Kinetics
RANS	Reynolds-Averaged Navier Stokes
RTD	Residence Time Distribution
SIMPLE	Semi-Implicit Method for Pressure-Linked Equations
TSTE	Taylor Series Truncation Error
UDF	User Defined Function
UDS	User Defined Scalar
VOF	Volume of Fluid

Chapter 1   Introduction

1.1   Background

Column flotation was invented in 1962 [1]. However, the first commercial size unit, a 36 inch diameter column was unsuccessful due to mechanical problems. It was only after several years that another unit, an 18 inch square column, was built in order to carry out tests and modifications to subsequently improve the larger column. The development work on the 18 inch column was successfully completed in 1967 and an identical 18 inch column was later installed in the first commercial operation at Mines Gaspé (in Quebec, Canada) in 1980 for Mo cleaning. The flotation column proved to perform better than conventional flotation cells, with a single column stage replacing several stages of conventional cells [2].

Over the years, column flotation has become a very important concentration technology used in mineral processing and coal beneficiation industries. However, flotation columns have also found other applications outside mineral processing such as de-inking of recycled paper [3]. The concentration process in column flotation is achieved through the collection of the valuable hydrophobic mineral particles by a rising swarm of air bubbles in counter-current flow against a slurry feed. The bubbles, which are formed by bubble generators (spargers) located near the column bottom then transport the mineral particles to the froth zone where the particles are eventually recovered in the overflow. Wash water is added continuously at the top of the column in order to maintain a net downward flow of water that eliminates entrained unwanted particles and stabilizes the froth. This net downward flow of water is referred to as positive bias flow [2]. A schematic diagram of the flotation column is presented in Figure 1.1.

The column volume is divisible into two sections: the collection zone in which bubbles collect the floatable mineral particles, and the cleaning zone (or froth zone) where wash water removes the unwanted particles entrained in the water crossing with bubbles from the collection zone. The two zones are separated by an interface which defines the froth depth or the interface level. Column flotation differs from conventional flotation in three major aspects:

- Addition of wash water to eliminate entrainment
- Absence of mechanical agitation

1

- Use of air spargers for bubble generation
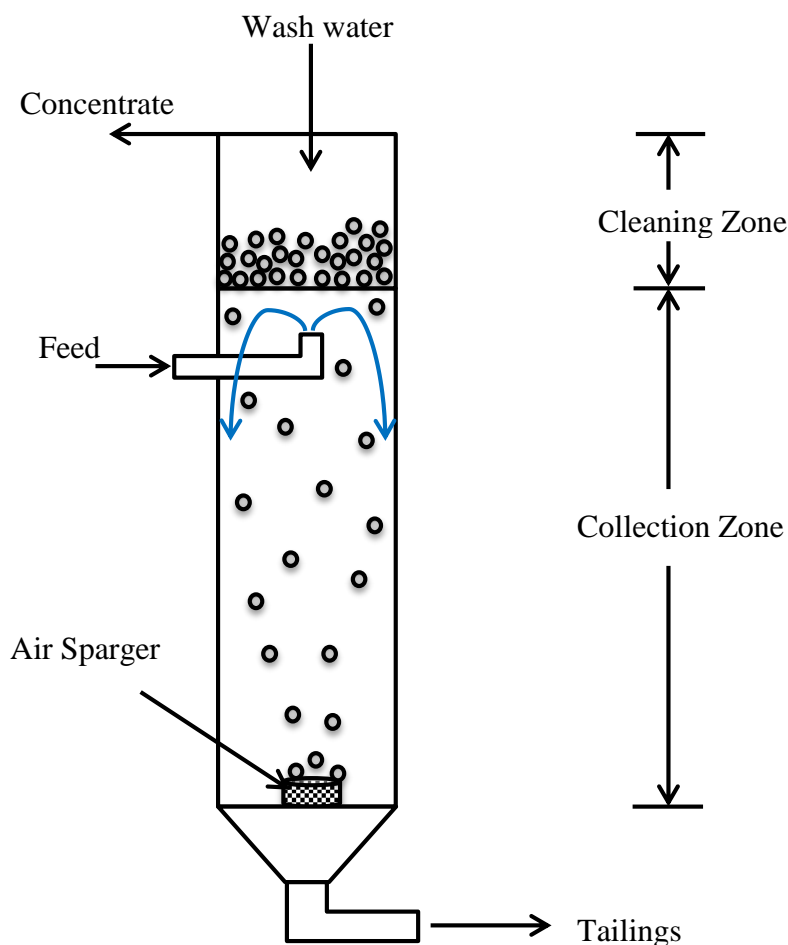
Figure 1.1: Schematic diagram of a flotation column.

The addition of wash water makes column flotation the preferred alternative to conventional flotation, which usually has lower grades due to particle entrainment. In addition, column flotation can achieve a higher grade concentrate in a single stage process compared with conventional flotation, which requires several stages to obtain a suitable grade [2].

The performance of flotation columns, in terms of grade and recovery depends largely on the gas dispersion and mixing characteristics of the column. Detailed knowledge of the gas dispersion and mixing parameters is therefore very important for the design, scale up, and optimization of flotation columns. Gas dispersion parameters include the superficial gas velocity (J_g), gas holdup (ε_g), bubble size (d_B), and bubble surface area flux (S_b). The gas holdup and the bubble surface area flux have a linear relationship with the flotation rate

constant [4] suggesting that these two parameters affect flotation column performance. The bubble surface area flux has been recognised as the key factor that can be used to characterise flotation machines. However, some researchers have found a linear relationship between the gas holdup and the bubble surface area flux [5, 6]. The gas holdup was therefore suggested to be used in place of the bubble surface area flux to characterise the flotation process. This could be advantageous since gas holdup is easier to measure.

On the other hand, the bubble surface area flux and the gas holdup are both determined by the superficial gas velocity and the bubble size. The superficial gas velocity also determines the prevailing flow regime in the column. There are two types of flow conditions that can occur in a flotation column, the bubbly flow regime characterized by uniform flow of bubbles of uniform size, and the churn-turbulent flow regime characterized by large bubbles rising rapidly in the collection zone causing liquid circulation. The bubbly flow regime is the optimal condition for flotation column operation [2, 7, 8]. However, excessive superficial gas velocity may cause loss of bubbly flow and subsequently cause a reduction in column performance. Excessive superficial gas velocity may also result in loss of the collection zone/cleaning zone interface, resulting in poor concentrate grade.

Mixing of the various phases in the flotation column has also emerged as one of the important factors which affect both the particle-bubble attachment and detachment processes [9, 10]. A high degree of mixing will therefore have a detrimental effect on the overall performance of a flotation column. The mixing parameters which are used to characterise axial mixing in the collection zone include the vessel dispersion number and the mean residence time of the liquid and solid phases. Mixing parameters are used to quantify the effect of mixing upon recovery [2].

Because of their significance in column flotation, gas dispersion and mixing parameters have been the focus of a large number of research publications in the mineral processing field. On the other hand, Computational Fluid Dynamics (CFD) has emerged as a numerical modelling tool that can be used to increase the understanding of the complex hydrodynamics pertaining to flotation cells [11-14]. However, there are a limited number of research publications on CFD modelling of column flotation. The earliest CFD model of column flotation was a two-dimensional two-phase fluid dynamic model presented by Deng et al. [11]. The model was used to simulate liquid and gas flow patterns in the column using the MAC (Marker and Cell)

3

numerical method. Subsequent CFD based models of column flotation have been published focusing on different aspects of the process [13-17].

In general, the existing CFD research on column flotation seems to have adequately addressed bubble-particle interaction processes such as collision efficiencies, attachment, and detachment [13, 16]. On the other hand, the gas dispersion and mixing parameters have not been adequately studied. The aim of the present research was therefore to apply CFD methodology to investigate the gas dispersion and mixing parameters in industrial and pilot scale flotation columns.

1.2   Objectives

The main objective of this research was to apply CFD modelling to investigate the gas dispersion and mixing parameters as well as their relationship to flotation column performance. In order to accomplish this main objective the research was divided into smaller objectives as outlined below:

- To formulate a CFD model capable of predicting gas dispersion and mixing in the flotation column
- To carry out CFD simulations to determine the following gas dispersion parameters
  - Gas holdup and its distribution in the column
  - Maximum superficial gas velocity for flotation column operation
- To perform CFD simulations of mixing in the column in order to determine the following parameters
  - The liquid residence time distribution RTD
  - The liquid mean residence time
  - The vessel dispersion number for the liquid phase
  - The Particle mean residence time
- To investigate the effects of gas dispersion parameters on the liquid flow patterns and mixing conditions in in the column
- To validate the CFD results with experimental data that is available in the literature

1.3   Scope and Limitations

The focus of this research is on the hydrodynamics and mixing characteristics of the collection zone in flotation columns. In the hydrodynamics part of the research, CFD

modelling is applied to predict both the average and local gas holdup, and bubble velocities in the collection zone of the column. CFD simulations are also used to investigate regime transition from bubbly flow to churn-turbulent flow in order to determine the maximum superficial gas velocity for column flotation.

The experimental work of Gomez et al. [18] is used in the present research for validation of the gas holdup predictions while the maximum superficial gas velocity predictions are compared against different experimental and theoretical results available in the literature [19-21]. Since the corresponding experimental research was performed in two-phase systems with water and air only (in the presence of frother), two-phase simulations are conducted in the hydrodynamics part of the present study in order to simulate the actual conditions that were used in the experiments.

On the other hand, the second part of the present research involves three-phase CFD simulations which are conducted in order to investigate liquid and solids mixing in industrial flotation columns. The actual flotation process in terms of bubble-particle collisions, attachment, and detachment is beyond the scope of the present research. However, these aspects have already been adequately studied by previous researchers notably Nadeem et al. [16] and Kho and Schwarz [13]. The present work therefore simulates the multiphase flow occurring in column flotation without incorporating bubble-particle interactions. The mixing parameters in flotation columns are mostly determined by the gas holdup (i.e., gas rate and bubble size) and the superficial liquid velocities. However, the presence of solids in bubble columns has been reported to have an influence on gas holdup due to its effects on bubble coalescence [22]. The predicted gas holdup in the CFD simulations is therefore limited to the influence from the superficial gas velocity, superficial liquid velocity, and bubble size used in the simulations.

The collection zone and the cleaning zone of a flotation column are known to have different hydrodynamic characteristics. Although it would be desirable to formulate a CFD model that includes both zones, the differences in turbulence and flow behaviour and the complex mass transfer occurring at the interface will make it difficult to obtain a single simulation that combines the two zones [23]. The CFD models applied in the present research therefore consider the collection zone of the columns while the froth zone is not modelled. Similarly, Deng et al. [11] did not include the froth zone in their CFD model. For column scale up purposes, previous researchers have suggested that the recovery in the distinct zones can be

modelled independently and then combined into the overall recovery for the column [24, 25]. In the same way, it is also acceptable in the present CFD model to consider the collection zone independent of the froth zone.

In terms of operating conditions and column geometry, the information available in the literature for the flotation columns simulated in the present work is limited to superficial velocities calculated over the entire column cross-section. Air spargers are therefore not included in the CFD model geometry in the present work. Instead, the air bubbles are introduced into the model over the entire cross section of the column. This is a valid representation considering that the sparging systems in industrial flotation columns are characteristically designed to provide an even distribution of air bubbles over the entire column cross section [26]. Uniform gas holdup distribution has also been experimentally confirmed for these sparging systems in laboratory and pilot scale flotation columns [27, 28]. The air bubbles are introduced into the collection zone in the model by means of mass and momentum source terms derived from the given superficial gas velocities.

The liquid phase (pulp) is also introduced into the column in similar fashion as the air bubbles, i.e, over the entire column cross section at the top part of the collection zone. This is also a legitimate representation considrering that the superficial liquid velocity at the liquid inlet boundary at the top of the collection zone must include both the bias water from the wash-water distribution system and the feed being introduced near the top of the collection zone.

In this work, a single and constant bubble size was assumed in all the subsequent CFD simulations. In other words each air bubble is assumed to have a constant diameter throughout its trajectory in the column. However, air bubbles rising in pilot and industrial scale flotation columns experience change in diameter as a result of the expansion caused by the decreasing hydrostatic pressure with increasing height along the column [29, 30]. This increase in bubble size results in an increase in the gas holdup and also increases the bubble rise velocity. Sam et al. [31] reported about 10% bubble expansion over a 4m height in an experimental water column. It is therefore important to highlight the constant bubble size assumption as one of the limitations of this work. However, using a constant bubble size not only simplifies the CFD model but it will also reduce the computational effort required to perform the simulations.

In the simulations where axial gas holdup profiles were of interest, compressibility effects were implemented using the ideal gas law to calculate the density of the air bubbles as a function of the local hydrostatic pressure values. However, since the actual hydrostatic expansion of the bubbles was not implemented in the CFD model, the bubble size is held constant in the simulations while allowing bubble density to vary in response to the changing hydrostatic pressure. This indirect method was earlier used by previous researchers in order to obtain the correct phase distribution in bubble columns [22, 32].

1.4   Scientific contributions and Novelty

There has been previous work conducted on CFD modelling of column flotation such as Deng et al. [11], Nadeem et al. [16], Kho and Schwarz [13] and Rehman et al. [17]. However, the unique contribution of the present work is the introduction of a detailed study of the gas dispersion and mixing characteristics of the collection zone of industrial and pilot scale flotation columns.

In terms of the gas dispersion in the column, this study applies CFD to predict the average gas holdup as well as the axial gas holdup distribution in the column. This provides a further opportunity to validate the CFD work with not only the average gas holdup data, but also the axial variation of gas holdup in the column. The axial variation of gas holdup has not been adequately investigated in the previous CFD modelling of flotation columns in the literature.

Numerical simulations are further applied in the present work to determine the maximum superficial gas velocity for transition from bubbly flow to churn-turbulent flow conditions in a flotation column. This is an important aspect for the application of CFD in column optimization which has also not been studied in previous column flotation CFD research. In particular, CFD has been used in the present research to confirm and demonstrate the relationship between the prevailing flow regime and the radial gas holdup profiles observed in the column. Radial gas holdup profiles can therefore be used to determine the change of flow regime from bubbly flow to churn-turbulent flow in the column. The use of Gas holdup versus Time graphs to determine the prevailing flow regime has equally been demonstrated using CFD.

Also in this study, residence time distributions (RTDs) for the liquid phase in the column are predicted and compared with experimental data available in the literature. In addition, solids mean residence time in the column is predicted using user defined scalar (UDS) transport

equations that calculate the age of the particles in the column. This method has been applied in studies of mixing in different reactors in the chemical engineering field [33-37]. However, this study is the first one to introduce particle age transport equations in column flotation modelling.

The introduction of the particle age UDS offers an attractive method for predicting both the solids and liquid mean residence time at lower computational cost compared to other methods that are based on Lagrangian particle tracking. In addition, the numerical solution of the particle age UDS gives the distribution of particle (solids) residence time in the column which can be used to understand the effect of liquid recirculation on the mixing behaviour of solids in column flotation. The predicted liquid RTDs and particle mean residence times can also become useful to compare and validate CFD work against experimental data.

1.5   Thesis Structure

The thesis consists of seven chapters. Each chapter begins with an introduction to give an overview or summary of its contents. In Chapter 1, column flotation technology is introduced together with a summary of literature findings that are used to define the objectives and scope of the present research.

Chapter 2 reviews the available literature focussing on gas dispersion and mixing characteristics of flotation columns. An overview of various modelling approaches applicable to column flotation is also included in this chapter.

In Chapter 3, the methodology that was used to simulate multiphase flow in both batch and continuous column operation is summarized. This includes geometry and mesh generation, choice of multiphase model, turbulence model, and numerical solution procedure.

In Chapter 4, Chapter 5, and Chapter 6, the CFD modelling work conducted in this research is described. The results of CFD simulations are presented and discussed under the respective 'Results and Discussion' sections included in the chapters. Each of these chapters ends with a conclusion summarizing the key findings from CFD simulations.

Chapter 4 describes the application of CFD to study gas holdup and axial gas holdup distribution in a flotation column. The simulation of mixing characteristics of industrial flotation columns is described in Chapter 5. In Chapter 6, the issue of flow regime transition

and maximum Superficial gas velocity is investigated. Chapter 7 concludes the present research and recommendations are outlined for future work.

Chapter 2   Literature Review

2.1   Introduction

This chapter provides a review of previous research on CFD modelling of column flotation. However, since the focus of the present research is on the application of CFD to investigate gas dispersion and mixing in column flotation, it is instructive to first introduce previous theoretical, experimental and industrial research focussing on gas dispersion and mixing parameters. The effects of the gas dispersion and mixing characteristics on the performance of the flotation column were briefly discussed in Chapter 1. On the other hand, a more detailed discussion is presented in this chapter in order to provide a sufficient background to place the present research in context. This literature review will therefore be structured according to the following themes: gas dispersion in column flotation, mixing characteristics of flotation columns, and finally a review of CFD models of column flotation in the literature.

2.2   Gas dispersion

Gas dispersion is the collective term encompassing three parameters in mineral flotation: the superficial gas velocity (or simply gas rate), gas holdup, and bubble size. The other parameter, bubble surface area flux, is derived from these and has emerged as a key parameter which is used to characterise the performance of flotation machines. The gas dispersion parameters are discussed in this section together with their relationship to the performance of flotation columns.

2.2.1   Superficial gas velocity and its effects on flotation column performance

Superficial gas velocity is defined as the volumetric flow rate of gas divided by the column cross-sectional area and is measured in cm/s [2]. The rate of flotation depends on the availability of bubble surface area in the column. However, the bubble surface area is controlled by the superficial gas velocity [38]. It has been observed generally that flotation column performance deteriorates when the superficial gas velocity is increased beyond a certain limit [20]. The identification of this maximum superficial gas velocity is therefore required for design, scale up, and effective operation of flotation columns.

2.2.1.1   *Maximum superficial gas velocity in column flotation*

The maximum superficial gas velocity in column flotation has been studied by a number of researchers [19, 20, 38, 39]. Dobby and Finch [39] investigated the interaction between

bubble size and superficial gas and liquid velocities together with their collective effect on the rate of particle collection in a column. They demonstrated that the maximum superficial gas velocity was dependent upon the bubble size and the superficial liquid velocity. The maximum superficial gas velocity was observed to decrease as bubble size decreased. The maximum gas velocity also decreased with increasing superficial liquid velocity. The dependence of the maximum superficial gas velocity on bubble size was further investigated by Xu et al. [20]. They found that the maximum gas velocity decreased with increasing frother concentration (or decreasing bubble size). Xu et al. [19] had earlier identified three phenomena that can be used to characterise the maximum superficial gas velocity: loss of bubbly flow, loss of interface, and loss of positive bias. These phenomena can therefore be used as a criteria for determing the maximum superficial gas velocity.

2.2.1.1.1 Loss of bubbly flow

Two types of flow have been distinguished in flotation columns, the bubbly flow regime characterised by uniform flow of bubbles of uniform size, and the churn-turbulent flow regime characterised by large bubbles rising rapidly causing liquid circulation in the collection zone [2, 20]. In small columns of diameter less than 0.1 m, the large bubbles may fill the column cross section giving rise to a slug flow regime. The flow regime, whether bubbly flow regime or churn-turbulent flow regime, depends on the superficial gas velocity or gas rate. Flotation columns are normally operated in the bubbly flow regime which is the optimal condition for the performance of the column [2, 7, 8]. However, excessive superficial gas velocity may change the flow regime from bubbly flow to churn-turbulent flow thereby affecting the performance of the flotation column. The increased mixing associated with the churn-turbulent flow regime results in a decrease in the recovery [40].

2.2.1.1.2 Loss of interface

Excessive gas rate or superficial gas velocity may also cause loss of collection zone/froth zone interface resulting in the loss of the cleaning effect of the froth zone[20]. As the gas velocity increases, the gas holdup in the collection zone increases while the gas holdup in the froth zone decreases [2]. The observed decrease in gas holdup in the froth zone is as a result of an increase in entrained water being transferred from the collection zone across the interface into the froth zone as the gas velocity increases. Loss of interface occurs when the gas holdup in the collection zone equals the gas holdup in the froth zone [2, 20]. In other

words, loss of interface occurs when sufficient water is transferred from the collection zone into the froth zone to make the water holdup become equal in the two zones [40]. This results in the loss of the cleaning effect of the froth zone. The loss of interface occurs at approximately the same superficial gas velocity as the loss of bubbly flow [20].

2.2.1.1.3 Loss of positive bias

Flotation columns are normally operated with a net positive flow (positive bias) of liquid from the froth to the collection zone. However, excessive superficial gas velocity may result in loss of positive bias and adversely affect the performance of the column. The role of the positive bias is to minimise entrainment in order to maximise the concentrate grade. Loss of positive bias will therefore cause deterioration in grade.

2.2.1.1.4 Effect of column diameter on the maximum superficial gas velocity

Ityokumbul [38] pointed out the possible dependency of the maximum gas velocity on the size or diameter of the flotation column. He derived an expression for the maximum gas velocity for bubbly flow conditions in the column including the effect of the column diameter. The first step was to determine the critical Froude number for bubbly flow conditions. The maximum gas velocity for transition from the bubbly flow regime was then related to the column diameter according to the following equation:

$$J_{g,max} = 0.109 d_C^{0.5} \tag{2.1}$$

2.2.2 Gas Holdup

Gas holdup is defined as the volumetric fraction (or percent) occupied by gas at any point in a column [2]. It is one of the most important parameters affecting the metallurgical performance of flotation columns. In this regard, some studies have reported that gas holdup affected both the recovery and grade in industrial and pilot scale flotation columns [41, 42]. These studies reported a linear relationship between gas holdup and recovery. It has been observed that the gas holdup has a linear relationship with both the flotation rate constant and the bubble surface area flux [4, 5, 41-43]. However, increasing gas holdup may also lower the concentrate grade because the subsequent increase in bubble surface area will also favour the collection of gangue and non-liberated particles either by true flotation or entrainment or both [42]. Some studies have suggested that gas holdup could be used for control purposes in column flotation [44].

Apart from its potential in control, gas holdup also has diagnostic applications. For example, rapid changes in gas holdup might indicate transition from bubbly flow to churn-turbulent flow conditions in the column. Another example is the sudden drop in gas holdup that occurs when a sparger is malfunctioning [44].

2.2.2.1 Gas holdup measurement techniques

The methods of determining gas holdup experimentally have been elaborated by Finch and Dobby [2] as shown in Figure 2.1.

a) Level rise   b) Pressure difference   c) Sensor (e.g. conductivity)
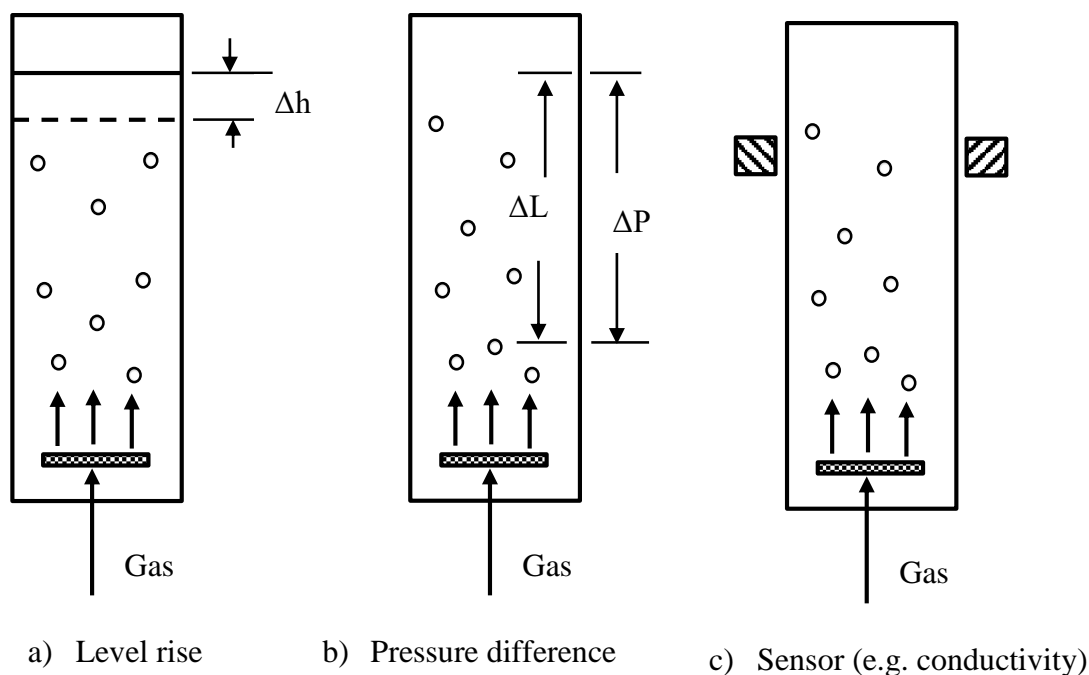
Figure 2.1: Methods of measuring gas holdup (adapted from Finch and Dobby [2]).

The pressure difference method is the most commonly used method in which gas holdup is measured over an interval between two positions along the column height as:

$$\varepsilon_g = 1 - \frac{\Delta P}{\rho_{sl} g \Delta L} \qquad (2.2)$$

where ΔP is the pressure difference, ρ_{sl} is the slurry density, and ΔL is the distance between the two pressure measurement positions. By taking pressure measurements at different locations along the column, the method can be used to determine the axial gas holdup profile. The gas holdup sensor method such as conductivity sensor can also be used to obtain axial gas holdup measurements in the column. On the other hand, the level rise method is

13

impractical in flotation columns where the froth phase occupies the top part of the column [2].

2.2.2.2 *Axial gas holdup distribution*

Gas holdup has been observed to vary with height along the collection zone of the flotation column – increasing by almost 100% from the bottom to the top part of the column [18]. The increase in gas holdup with height has been attributed to the hydrostatic expansion of air bubbles resulting from the decreasing hydrostatic pressure with increasing height along the column. Zou and Egiebor presented a force balance method describing the changes in gas holdup with column height [30]. They observed the existence of an exponential relationship between gas holdup and column height.

Gomez and co-workers [45] also measured gas holdup variations in a laboratory column and a pilot scale flotation column operated with water and air only. They obtained axial gas holdup profiles in which gas holdup approximately doubled over a distance of 8 to 10 m. The gas holdup profiles were not linear and had a gradient that increased towards the top of the collection zone.

2.2.2.3 *Radial gas holdup distribution*

Two general gas holdup profiles are known to exist, the parabolic profile and the saddle-shaped profile. Xu et al. [27] conducted measurements of radial gas holdup profiles in a flotation column using a conductivity technique. They found that two different types of profiles occurred depending on superficial gas velocity, a W-shaped profile at low superficial gas rates, and saddle- shaped profiles at higher superficial gas velocities. On the other hand, Serizawa and co-workers[46] observed that radial gas holdup profiles were a strong function of the prevailing flow pattern. The saddle-shaped profiles were thus associated with bubbly flow conditions, while parabolic profiles occurred under slug flow regime.

Subsequent investigations by other researchers have demonstrated the relationship between radial gas holdup profiles and the prevailing flow regime in bubble/flotation columns. Bennett et al. [47] used electrical capacitance tomography (ECT) to distinguish homogeneous (bubbly) flow from churn-turbulent flow. They reported that radial gas concentration (holdup) profiles changed from being initially flat at low gas flow rates to become more bow shaped and steep at the edges as the flow regime changed from bubbly flow to churn-turbulent flow. The radial gas concentration profiles showed that the transition between the two flow regimes was a gradual one.

14

2.2.2.4 *Liquid Circulation in the Column*

Liquid circulation and non-uniform radial gas holdup profiles in bubble/flotation columns are intimately related [48]. The density difference produced by non-uniform radial gas holdup profiles provides the driving force for the liquid circulation in the column. One particular liquid circulation pattern known as "gulf-streaming" in which the liquid flows up in the centre of the column and descends near the walls has been reported by a number of authors [48-50]. However, an inverse circulation pattern has also been proposed which is associated with saddle-shaped radial gas holdup profiles [51].

2.2.3 Bubble Size

Bubble size is one of the most important parameters affecting the performance of a flotation column. The rate of bubble-particle collision increases with decreasing bubble size. Particle collection is therefore a function of bubble size. It is therefore important to have a flotation process in which the bubble generation system produces smaller bubbles in order to increase the probability of bubble-particle collision. If large bubbles are produced, the recovery will be hindered because there will be fewer bubbles, less bubble surface area, and higher bubble velocity [1]. Typical bubble sizes in flotation columns are in the range $0.5 - 2$ mm.

Bubble diameter can be estimated from drift flux analysis. The method of estimating bubble diameter by drift flux analysis has been described in several publications including Dobby et al.[52], Yianatos et al.[53], Banisi and Finch [54], and López-Saucedo et al. [55]. In drift flux analysis, the slip velocity or relative velocity (U_{sb}) between the bubble swarm and the liquid (or slurry) depends on the superficial gas velocity (Jg), the slurry rate J_l and the gas holdup (ε_g) according to:

$$U_{sb} = \frac{J_g}{\varepsilon_g} \pm \frac{J_l}{\left(1 - \varepsilon_g\right)} \qquad (2.3)$$

where the +/- signs denotes countercurrent flow/cocurrent flow, respectively.

The slip velocity is then related to the bubble terminal rise velocity (U_t) and gas holdup (ε_g) according to the following relationship:

$$U_{sb} = U_t\left(1 - \varepsilon_g\right)^{m-1} \qquad (2.4)$$

where m is a function of the Reynolds number.

15

Banisi and Finch [54] determined that m = 3 fits the conditions encountered in flotation. The terminal velocity (U_t) estimated from equation (*2.4*) is used to calculate the bubble diameter (d_B) as:

$$d_B = \left[\frac{18\mu_{sl}U_t}{g(\rho_{sl} - \rho_b)} * \left(1 + 0.15Re_s^{0.687}\right) \right]^{1/2} \qquad (2.5)$$

where μ_{sl} is the slurry viscosity, Re_s is the Reynold's number of the bubble swarm, and ρ_{sl} and ρ_b are the slurry density and bubble density, respectively.

In summary, the method of estimating bubble size using drift flux analysis involves the use of experimental measurements of Jg and ε_g to find the value of d_B at which the U_{sb} calculated from equation (*2.3*) above is equal to the U_{sb} calculated from the following equation (*2.6*):

$$U_{sb} = \frac{g d_B^2 \left(1 - \varepsilon_g\right)^2 (\rho_{sl} - \rho_b)}{18\mu_{sl}\left(1 + 0.15Re_s^{0.687}\right)} \qquad (2.6)$$

López-Saucedo et al. [55] reported the results of an extensive programme to test the drift flux model at the industrial scale. With a relative error of approximately 15%, the bubble size estimated in industrial flotation columns in the range of 1.3 – 2.7 mm was found to be in good agreement with the experimentally determined bubble size. Hitherto, the drift flux model had only been validated at laboratory and pilot scale.

2.2.4   Bubble surface area flux (S_b)

The bubble surface area flux is the bubble surface area per unit time per unit cross-sectional area of the flotation cell. Flotation performance is related to the bubble size and bubble surface area flux since the flotation rate constant is related to the bubble surface area flux (which is calculated from the bubble diameter and superficial gas velocity).

Hernandez et al. [4] explored the relationship between the flotation rate constant (K_C) and gas dispersion parameters using de-inking of recycled paper in a flotation column. The rate constant was estimated from a mixing model (the axial dispersion model). The bubble size that was used to calculate the bubble surface area flux was estimated from drift flux analysis. A linear relationship between the flotation rate constant (K_C) and bubble surface area flux was found. A similar linear dependence of the flotation rate constant on gas holdup has also been reported suggesting that these two gas dispersion parameters can be interchanged. The

bubble surface area flux is related to the bubble size and gas holdup according to the following equations, respectively:

$$S_b = \frac{6J_g}{d_B} \tag{2.7}$$

$$S_b \cong 5.5\varepsilon_g \tag{2.8}$$

2.3   Mixing

Considering the particle collection process in a column as a first-order rate process, the recovery of particles in the collection zone is dependent upon three variables [2]:

- the rate constant k_c
- the mean residence time, and
- a mixing parameter

The mixing conditions within the flotation column are therefore important for scale-up and design purposes. In the extreme case, mixing can be considered as either plug flow transport or a perfectly mixed reactor. In plug flow, the residence time of all elements of the fluid (and mineral particles) is the same. Plug flow in a column will mean there is a concentration gradient of floatable mineral along the axis of the column. In a perfectly mixed reactor, there is a distribution of retention time and the concentration is the same throughout the reactor.

Transport conditions in the plant flotation column are usually between those of plug flow and perfectly mixed flow. In this case, the one-dimensional (axial) plug flow dispersion model is used to describe the axial mixing process in the collection zone of the flotation column [2]. The degree of mixing is quantified by the axial dispersion coefficient D (units of length^2/time). The mixing conditions can also be described in terms of two mixing parameters: the mean residence time τ and the dimensionless vessel dispersion number N_d. The vessel dispersion number is given by:

$$N_d = \frac{D}{uH} \tag{2.9}$$

where u is either the liquid interstitial velocity or the particle velocity and H is the height of the collection zone. For plug flow conditions $N_d = 0$ while $N_d = \infty$ represents perfectly mixed flow. The inverse of N_d, called the Peclet number Pe is sometimes used in place of N_d to describe mixing conditions in a column.

17

Mixing parameters are used to quantify the effect of mixing upon recovery. This relationship is given by Levenspiel's equation as [2]:

$$R = 1 - \frac{4\,a\,exp\left(\frac{1}{2N_d}\right)}{(1+a)^2 exp\left(\frac{a}{2N_d}\right) - (1-a)^2 exp\left(\frac{-a}{2N_d}\right)} \qquad (2.10)$$

where

$$a = (1 + k\tau N_d)^{1/2}$$

Equation (2.10) is plotted in Figure 2.2 for various N_d values as function of the dimensionless parameter, kτ. It can be sseen that the recovery R increases with kτ at fixed N_d. However, it can also be seen that R decreases with increasing N_d. In other words, the recovery decreases as conditions move from plug flow towards perfectly mixed flow. Mixing in column flotation therefore has a detrimental effect on flotation performance since it reduces mineral recovery.
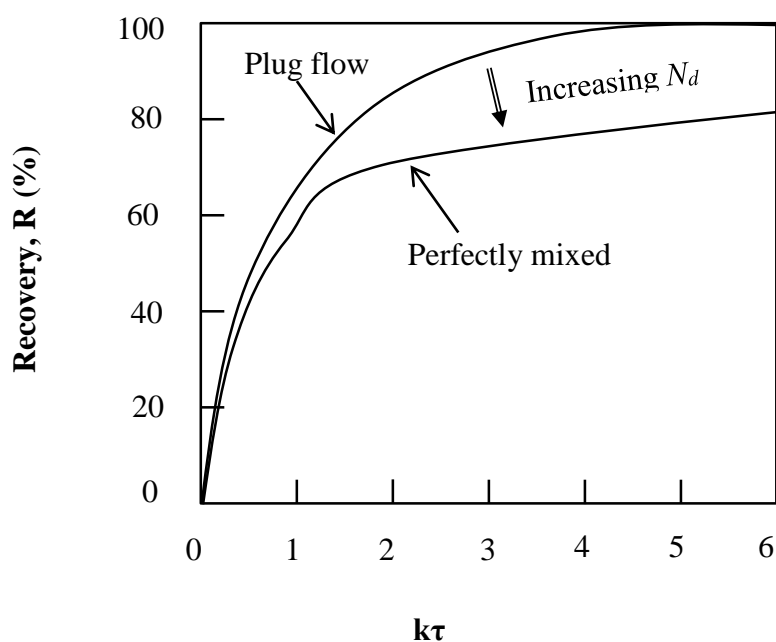
Figure 2.2: Recovery as a function of the dimensionless product kτ for different values of N_d (Redrawn from Luttrell et al. [56]).

Mixing in flotation columns has been studied by several researchers [57-66]. However, there are still unresolved issues particularly with regard to a suitable mixing model and solids mixing characteristics. Dobby and Finch [58] measured the axial dispersion parameters of

large industrial columns as an initial step towards the development of a scale-up methodology for flotation columns. Their work involved pulsed tracer tests using liquid and solid tracers on 0.46 and 0.91 m square columns, each 13 m high. The axial dispersion coefficient of solids (D_s) was found to be equal to the liquid dispersion coefficient (D_l). The axial dispersion coefficient (in m²/s) was also found to be linearly dependent on column diameter according to the following relationship:

$$D_s = D_l = 0.063 d_C \qquad (2.11)$$

Mavros [9] reviewed different liquid phase axial dispersion coefficient data available in the literature. The existing correlations were tested and a new correlation covering data for different column sizes was derived. The axial dispersion coefficient was found to be related to the column diameter and superficial gas velocity according to the following expression:

$$D = (9.3 d_C - 30.1) J_g^{0.603} \qquad (2.12)$$

The expression was able to estimate the axial dispersion coefficient reasonably. However, the expression does not account for the effect of the superficial liquid velocity and is only applicable to a limited range of liquid superficial velocities.

Mavros and Daniilidou [10] performed residence time distribution measurements of the liquid phase in four flotation columns with increasing diameters. The measurements were presented and analysed according to the axial dispersion model. The mixing of the liquid phase was studied systematically in order to determine the effect of the column diameter and the superficial liquid and gas velocities on the mixing process. The dispersion number, characterising mixing, was determined in flotation columns of internal diameters varying from 2.5 to 11.0 cm and the results were compared with literature data to obtain the following correlation:

$$N_d = 0.0194 \exp (0.267 d_C) J_l^{-0.56} \qquad (2.13)$$

where J_l = superficial liquid velocity.

Their experimentally obtained dispersion number data indicated that mixing in a flotation column depends mostly upon the column diameter and the superficial liquid velocity. For the usual range of velocities, the narrower the column, the less mixed are its contents, since plug flow conditions are approached. The larger the column is, the more mixed will be its contents

leading to intense recirculation phenomena. It was also observed that the gas velocity (J_g) does not affect the dispersion number considerably, while liquid velocity (J_l) seems to have a limiting effect. In other words, the effect of J_l will at some stage begin to diminish until a limit is reached beyond which it will no longer have any effect on the liquid dispersion number.

Mankosa et al. [63] investigated mixing in column flotation and used RTD data to derive expressions relating column operating and design parameters to axial dispersion. These authors found that the axial dispersion increased with increasing gas rate and column diameter while an increase in either liquid flow rate or column length caused a decrease in axial dispersion. Using dimensional analysis an expression was obtained in which the Peclet number (*Pe*) is related to column flow rates and geometry as follows:

$$Pe = 0.7 \left[(H/d_C)^{0.63} \left(u_i/J_g \right)^{0.5} \right] \qquad (2.14)$$

The above expression was found to be useful for a wide range of design and operating parameters.

Yianatos and Bergh [65] measured the residence time distribution of the liquid and solid particles in an industrial flotation column in order to compare the hydrodynamic behaviour of the liquid and mineral phases. The residence time of liquid (or fine particles) was found to be about half the residence time of the coarse particles. It was also confirmed that the solids and liquid axial dispersion coefficients were equal.

Yianatos et al. [66] evaluated the mixing characteristics and the effective residence time of liquid and solid particles in industrial flotation equipment including mechanical cells and flotation columns. In their work the mixing characteristics in flotation columns were modelled using the Axial Dispersion Model (ADM) and the Large and small tanks in series model (LSTS). The LSTS model consists of one large perfect mixer in series with two small perfect mixers plus a dead time. The two small perfect mixers correspond to the feed input and bubble generation zones while the large perfect mixer is related to volume extending from below the feed enterance to the bubble generation level.

The analytical solution of this model was given by Yianatos et al. [66]. The LSTS model was found to provide a more adequate description of the liquid mixing in flotation columns compared to the ADM (using closed-closed boundaries). It was also found that despite the

presence of baffles, the mixing conditions in industrial columns are close to well mixed. Their results further showed that the vessel dispersion number for the solid particles was similar with the liquid one. However, the overall solids residence time was 11% smaller than the liquid one despite the fact that the average particle size was finer (25% w/w with particle sizes > 24 μm). These observations are similar to earlier findings by Dobby and Finch [58] and Yianatos and Bergh [65].

Massinaei et al. [67] studied the mixing conditions in industrial rougher columns using residence time distribution (RTD) data. They used a radioactive liquid tracer (Br-82) to trace the material reporting to tailings and concentrate streams. It was found from the RTD analysis that the large and small tanks in series (LSTS) model was the best model for representing the liquid transferred to tailings while the N perfect mixers in series model best represented the liquid going to the concentrate stream. A theoretical model for counter-current columns was used to estimate the solids mean residence time. The results obtained showed a ratio of 1.4:1 between the liquid and solids residence times. This work also showed that despite the presence of vertical baffles in the columns, the mixing conditions were close to well mixed.

Massinaei et al. [67] further described the possible causes of mixing in industrial columns. Mixing or turbulence in industrial flotation columns was attributed to convective pulp recirculation and turbulent dispersion resulting from the counter-current contact between the bubble swarm and the pulp. The feed and air entrances also cause mixing near the top and bottom parts of the column, respectively. In addition, operating variables can also affect the mixing conditions in an industrial flotation column. For example, increasing the superficial gas velocity may result in increase in the extent of mixing in the column while increasing the pulp density will result in a reduction in the degree of mixing.

2.4   CFD models of column flotation in the literature

The use of mathematical modelling in research aimed at achieving improvements in mineral processing and extractive metallurgy has been growing in importance. The models that are being applied for this purpose range in complexity from those based on statistical regression of experimental data (empirical models) to detailed micro-phenomenological models representing all the physical and chemical phenomena associated with the process being modelled [68].

In linear regression models, the process performance criteria are expressed as simple linear functions of the process variables. However, such empirical models are usually case sensitive and cannot be extrapolated beyond the range of data from which the model was derived. Inspite of these limitations, empirical models have very useful features: they are easy to construct, easy to apply, and they provide helpful information about the process which can be used to develop more general models [69]. On the other hand, phenomenological models provide a realistic representation of the process and are capable of being extrapolated. The information required to develop this type of models can be obtained by means of fluid flow simulation using Computational Fluid Dynamics (CFD) modelling [68].

Computational Fluid Dynamics (CFD) can be described as the study of fluid flow, heat transfer and related phenomena using computer-based numerical simulations. CFD is based on a set of governing equations derived from the laws of conservation of mass, momentum, and energy. These equations form a system of non-linear partial differential equations (PDEs) which usually have no analytical solutions. Numerical methods are therefore needed to solve the governing equations in CFD simulations.

The derivation of these equations can be found in several texts such as Anderson [70] and Versteeg and Malalasekera [71]. As described by Anderson [70], CFD involves replacement of the partial differential equations with discretized algebraic equations that approximate the partial differential equations. These algebraic equations are then solved to obtain flow field values at discrete points in space and/or time. The discrete points define the grid or mesh of the solution. The process of developing a set of algebraic equations that can be used in place of partial differential equations is known as discretization. The algebraic equations are then solved at discrete points in the flow domain.

Over the last few years, CFD has emerged as a powerful tool that can be used to predict the complex hydrodynamics as well as the performance of mineral flotation cells. In CFD modelling, the flotation cell is discretized into finite control volumes or grid cells where local values of flow field variables are calculated. The detailed understanding of flow physics that is achieved by using this method allows modifications to existing equipment and operating conditions to improve flotation performance.

Mineral flotation is a multiphase process involving three phases: liquid, air bubbles, and mineral particles. Multiphase models are therefore required in order to carry out CFD simulations of a flotation cell. Some of the most widely used multiphase models include the

Eulerian-Lagrangian, the Eulerian-Eulerian, and the Volume-of-fluid (VOF) models. In the Eulerian-Lagrangian approach, the liquid phase is modelled as a continuum while the dispersed phase is modelled by tracking the individual trajectories of a large number of particles. This approach is therefore limited to systems with a low volume fraction of dispersed particles.

On the other hand, the Eulerian-Eulerian modelling approach treats all the different phases as continuous phases. The momentum and continuity equations are then solved for each phase separately. The Eulerian-Eulerian model can be applied to simulate very complex flows. However, it does not always give the best results since empirical information is required to close the momentum equations [72].

The VOF model is a Eulerian-Eulerian model in which the interface between the different phases is tracked. The model can be used to simulate stratified flows, free surface flows, and the movement of large bubbles in a liquid phase. Since the interface between the fluids must be resolved, the VOF model is not suitable for a system with a large number of bubbles.

Despite CFD being one of the most widely used numerical modelling methods, literature on CFD modelling of column flotation is rather scarce. One of the earliest CFD models of column flotation was reported by Deng et al. [11] who presented a two-dimensional, two-phase, fluid dynamic model of a flotation column. The model was used to simulate liquid and gas flow patterns in the collection zone of the column using the MAC (Marker and Cell) numerical method. The numerical computations were performed only for one half of the column since the system was assumed to be axis-symmetric. The simulated liquid axial velocity profile revealed a liquid circulation flow pattern in which the liquid flows upwards in the center part of the column and downwards near the column walls. This study further concluded that liquid mixing in flotation columns was primarily caused by the liquid circulation resulting from gas flow rather than dispersion. However, only laminar flow was considered in the study hence the model did not consider the effect of turbulent fluctuations or turbulent eddies on liquid mixing in the column. Moreover, the actual mixing characteristics of the column were not investigated in terms of residence time distribution simulations. The model was also not validated with experimental data due to limited published results at the time of their work.

Subsequent CFD based models of column flotation have been published focusing on different aspects of the process. Building upon the work of Deng et al. [11], a two-dimensional Euler-

23

Lagrangian model was used by Xia et al. [15] to simulate the alleviation of liquid back-mixing by baffles and packings in a flotation column. These authors studied the liquid flow patterns in three different column geometries in order to compare the liquid back-mixing in an open column, a horizontally perforated plate baffled column, and a regular structured packed column. The simulated results revealed that the liquid back-mixing effect in bubble columns could be alleviated using baffles or packings. In addition, the effects of operating conditions such as uneven aeration, gas velocity, and bubble size on liquid flow patterns in the column were also studied. A decrease in bubble size was reported to have caused an increase in the upward axial liquid velocity resulting in a possible increase in liquid back-mixing in the column. However, similar assumptions were applied as in Deng et al. [11] where turbulence effects were not considered. The actual mixing processes in terms of liquid RTD were also not included in the simulations.

A similar study was also conducted by Rehman et al. [17] who investigated the effect of various perforated baffle designs on air holdup and mixing in a flotation/bubble column using CFD. To reduce the computational cost, simulations were performed only for one quarter of the column geometry using a rotational periodic boundary condition to periodically repeat the results for the entire column. The Eulerian-Eulerian multiphase model was utilized in the simulations together with the standard k-epsilon turbulence model. The trays (baffles) were observed to significantly increase the overall air holdup compared to the column without baffles. A similar observation was also reported by Xia et al. [15] who suggested that the presence of baffles and packing would hinder the upward movement of bubbles and therefore increase the bubble retention time or gas holdup. Rehman et al. [17] further reported a slight decrease in gas holdup with height or axial direction which was attributed to the increase in bubble size as a result of reduction in static pressure. However, this trend is quite the opposite of the well known axial increase in gas holdup that has been previously reported by several researchers [18, 30, 45, 73].

Another study was conducted by Chakraborty et al. [14] in which the effect of air flow rate, height-to-diameter ratio, column taper angle, and sparger configuration on the hydrodynamics of the column flotation cell was investigated. The Eulerian-Eulerian or two fluid model was was employed to simulate the gas-liquid two phase flow in the column while turbulence in the continuous phase was modelled using the well known single phase standard k-ϵ turbulence model. In addition, the model suggested by Sato and Sekoguchi [74] was used to account for bubble induced turbulence. This study concluded that increasing air flow rate

24

resulted in an increase in gas holdup and complexity in the bubble plume structure. In addition, increasing column height-to-diameter ratio was also observed to bring about a complex flow pattern with multiple staggered vortices in the column. A low height-to-diameter ratio was therefore recommended as one of the required conditions for obtaining good separation in a column flotation cell. However, previous studies [63] have also reported that increasing height-to-diameter ratio actually results in a decrease in axial mixing in the column. Increasing column height-to-diameter ratio will therefore result in improved recovery and performance of the column. In terms of the effect of sparger configuration, the work by Chakraborty et al. [14] found that uniform gas distribution was essential for column flotation. Xia et al. [15] also recommended uniform aeration across the cross section of the column.

Other recent CFD models of column flotation have focussed more on bubble-particle interactions such as collision, attachment and detachment processes in the collection zone of flotation columns. Some of the research reported in this category include the work by Nadeem et al. [16]. and Koh and Schwarz [13]. Nadeem et al. [16] presented their work on CFD simulation of bubble-particle collision probabilities in quiescent flotation conditions similar to the conditions prevailing in column flotation. The simulations were conducted using an Euler-Lagrange approach in which the velocity field was solved for steady state conditions. The solid particles were introduced as a discrete phase injection and the subsequent particle tracks were used to calculate collision probabilities. Turbulence was modeled for the continuous phase using the standard k-ϵ turbulence model. The bubble-particle collision probability was then modeled in a small rectangular geometry with a stationary bubble positioned at its centre. A trap boundary condition was applied on the bubble in order for the particles to become trapped upon collision. The collision probability was then obtained as the ratio of trapped particles to the total number of particles. An important finding of Nadeem et al. was that the probability of collision was higher for a smaller (1 mm) bubble than for a larger (1.5 mm) bubble.

Koh and Schwarz [13] studied hydrodynamics in coal flotation using computational fluid dynamics. They applied an Eulerian-Eulerian multi-fluid model to simulate a microcel column and a Jameson cell using the CFD code CFX-4.4. The standard k-ϵ turbulence model was used to model turbulence in the continuous pulp phase. The flotation effect was modeled by considering three sub-processes including collision, attachment, and detachment. A significant finding of their work was that the local particle-bubble detachment rate was

determined by the local value of the turbulent dissipation rate. The importance of identifying those regions of high turbulent dissipation rates was therefore highlighted by these authors.

In a recently published paper, Sarhan et al. [75] have studied the impact of the presence of solid particles on bubble coalescence and breakup in column flotation using Computational Fluid Dynamics (CFD). They employed the commercial CFD software package AVL FIRE 2009.2 to model the hydrodynamics in the flotation column cell. The two-fluid or Eulerian-Eulerian multiphase model was used together with the standard k-ϵ turbulence model which was used for calculating the turbulent viscosity in the continuous (liquid) phase. In addition, the population balance equation (PBE) was used to predict the number density of different bubble size classes in the column. This study found that the presence of solids reduced the gas holdup in the flotation cell (column). The authors also reported that the size of gas bubbles decreased with increasing superficial gas velocity causing the gas holdup to increase. Their results further showed that the sauter mean bubble diameter decreased with increasing solids concentration.

The CFD models of column flotation discussed above have all focussed on the processes occurring in the collection zone of the column. However, some CFD models of froth behaviour in flotation cells are also available in the literature [23, 76]. Cilliers [23] presented a paper in which the use of CFD in foam and froth modelling was discussed. The paper included an introduction of the physics of froths and a review of the methodology of combining the models for each phase into a complete description. An example of the use of froth CFD for equipment design was also given in which two alternative methods of wash water addition were compared. The paper concluded by highlighting a number of issues that still need to be addressed, in particular, the failure of bubble films causing coalescence in the froth and the bursting of bubbles on the surface. Cilliers [23] further observed that the combination of pulp and froth models into a single simulation was desired but difficult to accomplish due to the differences in turbulence and flow behaviour, and the complex mass transfer across the pulp-froth interface.

A more recent publication [76] describes a numerical model for the flow of foams in flotation cells that can be used to simulate flowing foams in up to three-dimensions. The numerical model was implemented in *fluidity*, a general purpose finite element method code that allows simulations to be carried out on anisotropic unstructured meshes. The code makes use of the finite elements to solve Laplace's equation for a potential function and is capable of using

anisotropic adapted meshes to accurately solve the foam velocity field. A summary of previous literature on CFD modelling of column flotation is presented in Table 2.1.

Table 2.1: Previous literature on CFD modelling of column flotation.

Reference	Column size	Multiphase model	Turbulence model	Modelled zone
Deng et al. [11]	Diameter – 0.2 m Height – 2.0 m	Eulerian-Eulerian	Laminar	Collection zone
Xial et al. [15]	Width – 0.2 m Height – 1.0 m	Euler-Lagrange	Laminar	Collection zone
Chakraborty et al. [14]	Width – 0.25 m Height 0.25 – 2.0 m	Eulerian-Eulerian	Standard k-ϵ model	Collection zone
Nadeem et al. [16]	-	Euler-Lagrange	Standard k-ϵ model	Collection zone
Koh and Schwarz [13]	Diameter – 4.9 m Height – 10.7 m	Eulerian-Eulerian	Standard k-ϵ model	Collection zone
Rehman et al. [17]	-	Eulerian-Eulerian	Standard k-ϵ model	Collection zone
Sarhan et al. [75]	Diameter – 0.1 m Height – 1.68 m	Eulerian-Eulerian	Standard k-ϵ model	Collection zone
Cilliers [23]	-	-	-	Froth zone
Brito-Parada et al. [76]	-	-	-	Froth zone

2.5   Conclusion

This literature review has discussed the established body of knowledge regarding gas dispersion and mixing characteristics of flotation columns. Previous CFD models of column flotation available in the published literature have also been reviewed. The various approaches that have been used to model column flotation are outlined in Table 2.1. Most of the researchers have used the Eulerian-Eulerian multiphase model together with the standard k-ε turbulence model to simulate the multiphase flows in the flotation column while others have assumed that turbulence was insignificant. It would therefore be instructive to investigate the effect of the different turbulence models in the context of column flotation modelling. However, this might not be possible to do in the present research due to lack of detailed experimental data against which the various models can be compared.

Despite the fact that a number of CFD models have already been reported by previous researchers, this literature review has found that gas dispersion and mixing in column flotation have not been adequately studied. For example, the only study in which the axial gas holdup is investigated reported profiles that contradict the well known axial increase in gas holdup along the column axis [17]. On the other hand, while both Deng et al. [11] and Xia et al. [15] discuss mixing in column flotation, the actual mixing in the column in terms of RTD studies has not been simulated. The conclusions that were made in these studies regarding back-mixing in column flotation were therefore based entirely on the effects of various operational or geometrical conditions on the axial liquid velocity profiles. However, it would be more informative to investigate the effect of operating parameters (such as superficial gas velocity or bubble size) or column geometry on the actual liquid mixing parameters such as the vessel dispersion or axial dispersion coefficient. In addition, the work conducted by Deng et al. [11] and Xia et al. [15] was limited to two phase (gas-liquid) flow in which mineral particles were not considered. The mixing characteristics of solids in column flotation have therefore not been studied in the previous CFD models.

Considering the gaps established in this literature review, the purpose of the present research is to apply CFD methodology to investigate the gas dispersion and mixing chacteristics of pilot and industrial scale flotation columns. In terms of gas dispersion parameters, CFD will be applied to simulate the average gas holdup and the axial gas holdup variation in a pilot column flotation cell. The effect of gas rate and flow regime on radial gas holdup profiles will be investigated in the context of the maximum superficial gas velocity for column flotation. On the other hand, the mixing parameters in column flotation will be studied with

28

particular interest on the solids mixing characteristics and the effects of particle and bubble sizes on the liquid dispersion number.

Chapter 3   Simulation Methodology

3.1   Introduction

This chapter provides the details of the methodology that will be employed in this thesis. The aim of the research, namely to apply CFD simulations to investigate gas dispersion and mixing in flotation columns has been established in the literature review in the previous chapter (Chapter 2). The focus of this methodology chapter is therefore on the development of a CFD methodology that is capable of providing reliable predictions of the gas dispersion and mixing parameters in the column. In general, CFD simulations involve the following six aspects:

- defining a representative model geometry and boundary conditions for the equipment that is to be modelled
- meshing the model geometry in order to generate a grid of cells in which flow variables will be calculated
- selecting suitable modelling approaches for computing the turbulent multiphase flow problem under study
- Setting up the solver solution methods for the computation
- Solving the corresponding partial differential equations for the flow variables
- Analysing the results

This chapter is therefore laid out in such a way that these six themes are addressed in the flotation column CFD model.

3.2   Model geometry, mesh and boundary conditions

3.2.1   Defining the computational domain

Flotation columns are divisible into two distinct zones as described in Chapter 1, the collection zone and the cleaning zone. Since the two zones have different hydrodynamic characteristics, the definition of a relevant computational domain is essential to the simulation of flotation columns. In as much as it would be desirable to formulate CFD simulations that combine the two zones, their inherent differences in the flow and turbulence characteristics would make it difficult to combine the two zones together in a single simulation [23]. In addition, such a CFD model would have to account for the complex mass transfer processes occurring accross the interface between the two zones.

Previous studies have either simulated the collection zone or the froth zone as described in the literature review. The present model therefore considers the collection zone of the columns while the froth zone is not modelled. The resulting simplified model geometry is a vessel of height equal to the collection zone height and radial dimensions similar to the respective industrial or pilot column being simulated.

3.2.2 Modelling of the spargers

The sparging of gas was modelled by means of mass and momentum source terms for the computational cells at the bottom of the column. The model assumes that the gas phase enters the column in form of air bubbles. Since the sparging systems that are used in industrial flotation columns are designed to achieve uniform distribution of air bubbles over the entire column cross section [26], the air bubbles were introduced over the entire column cross section in the present research without including the physical spargers in the model geometry. Uniform air distribution has also been verified in pilot scale flotation columns by means of radial gas holdup measurements [27, 28]. The use of the entire column cross section for bubble introduction into the column is therefore a legitimate albeit simplified representation of the sparging system in the simulated columns. Correspondingly, the information available in the literature for the simulated flotation columns was mostly presented in terms of superficial velocities calculated over the entire column cross-section.

3.2.2.1 *Calculation of mass and momentum source terms*

The mass and momentum source terms were calculated from the superficial gas (air) velocity, J_g as follows:

$$Mass\ source\ =\ \frac{\rho_{air} * A_c * J_g}{V} \tag{3.1}$$

where ρ_{air} is the density of air (1.225 kg/m^3), A_c is the column cross-sectional area (m^2), J_g is the superficial gas (air) velocity (m/s) and V is the volume of the cell zone where the source terms are applied. The momentum source terms were calculated from the respective mass source terms according to the following equation:

$$Momentum\ source\ =\ mass\ source * J_g \tag{3.2}$$

In this study, the air bubbles are assumed to emerge from the sparger in the upward direction. The momentum source terms were therefore introduced in the upward direction, in other words, only the Y momentum component was considered while the X and Z momentum

components were neglected. The calculated mass and momentum source terms for the different columns simulated in this research are provided in Appendix 1 and 3.

3.2.3   Boundary conditions

3.2.3.1   Batch operated columns

For the batch operated column, there are no inlets or outlets for the liquid phase. Boundary conditions were therefore specified for the column wall only. In this case, no slip boundary conditions were applied at the column wall for both the continuous phase (water) and the dispersed phase (air bubbles).

3.2.3.2   Continuously operated columns

For the continuously operated column, inlet and outlet boundary conditions had to be specified at the top (inlet) and bottom (outlet) of the column. For the liquid phase the top of the column was modelled as a velocity inlet boundary where inlet velocity was set equal to the superficial liquid velocity, J_l. Since the computational domain being considered is the collection zone of the column, the superficial liquid velocity must include the feed rate plus the bias water resulting from wash water addition. The superficial liquid velocity is therefore equal to the superficial tailing rate. The bottom part of the column was also modelled as velocity inlet boundary where exit velocity was set equal to superficial liquid velocity but with a negative sign. For the column wall, no slip conditions were applied a for both the liquid (continuous phase) and the air bubbles as well as solids (dispersed phases).

3.2.4   Mesh size and grid independence considerations

In order to eliminate the possibility of errors resulting from coarse mesh sizes, grid dependence studies were undertaken in which the mesh was progressively refined from an initially coarse mesh until there was no significant change in the simulated axial water velocity and bubble velocity profiles.

3.3   Multiphase model

3.3.1   Overview of multiphase models

The models for simulating multiphase flows can generally be grouped into three classes:

- Direct Numerical Simulation (DNS)
- Eulerian-Lagrangian
- Eulerian-Eulerian

Direct numerical simulations (DNS) can be used to obtain a full resolution of the behaviour of bubbles or particles in a carrying fluid. Multiphase DNS therefore involves simulations in which one fully resolves the temporal and spatial scales relevant to the fluid dynamics [77]. One of the most widely used methods in multiphase DNS is the Volume of Fluid (VOF) method. In the VOF model the interface between the different phases is tracked. The VOF model is suitable for simulating stratified flows, free surface flows and the movement of large bubbles in a liquid [78]. Since the interface between the phases must be resolved, VOF is not applicable for systems with a large number of bubbles or liquid droplets.

In the Eulerian-Lagrangian modelling method, the continuous phase is modelled as a continuum by solving the Navier-Stokes equations. On the other hand, the dispersed (secondary) phase is simulated in a Lagrangian frame of reference by tracking the motion of the individual particles (or bubbles) using an equation of motion. However, the computational cost associated with computing individual particle or bubble trajectories is high and increases with an increase in the number of simulated particles. The Eulerian-Lagrangian method is therefore limited to dilute systems in which the dispersed phase volume fraction is less than 10% [78, 79].

In the Eulerian-Eulerian modelling approach, the different phases are considered as continuous phases that are interacting with each other. Conservation equations governing the balance of mass, momentum, and energy are in this case solved for each phase separately. However, the interaction between the different phases must be accounted for through additional models.

3.3.2   Choice of multiphase model for the present research

The multiphase CFD model used in this research was selected after a thorough literature review of CFD models of bubble column reactors and flotation columns. The 'hierarchy of models' concept that was introduced by Delnoij et al. [80] was particularly useful in the selection of a suitable multiphase model for industrial and pilot scale flotation columns.

A range of hydrodynamic phenomena characterised by different length and time scales occur in bubble columns. In addition, a wide range of bubble diameters and shapes can also be encountered depending on the physical properties of the liquid phase and the flow regime in which the bubble column is being operated. Bubble columns also differ in sizes and geometry. It is, therefore, difficult to develop a generalized CFD model that is capable of

resolving all the different hydrodynamic features occurring at the various length and time scales.

The 'hierarchy of models' concept recommends different CFD models depending on the size of the column, the length scales of the particular hydrodynamic phenomena, and the prevailing flow regime. In other words each model is applied for studying specific hydrodynamic phenomena, occurring at a defined scale [81].

According to Delnoij et al. [80] a two-fluid model is recommended to study flow structures occurring in industrial scale bubble columns due to its relatively lower computational cost. An Eulerian-Eulerian two-fluid model was therefore chosen in the present research considering the size of the simulated flotation columns. The Eulerian-Eulerian approach has been applied in several CFD models of pilot-scale bubble columns [22, 32, 82] of similar dimensions as the flotation columns that are simulated in the present research. A review of previous CFD models involving column flotation also found that the Eulerian-Eulerian model was used in most of these studies[11, 13, 14, 17].

3.3.3   Eulerian-Eulerian multiphase model

In the Eulerian-Eulerian approach, both the continuous (primary) phase and the dispersed (secondary) phase are modelled in an Eulerian frame of reference as interpenetrating continua. The gas, solid, and liquid phases are considered as three distinct phases that are interacting with each other. Conservation equations for mass and momentum are therefore solved for each phase separately. Interaction between the phases is then accounted for by means of momentum exchange terms incorporated in their respective momentum equations.

In the present research, the multiphase flow in the flotation columns was modelled considering water as the continuous phase (or primary phase) while air bubbles and solid particles were treated as dispersed phases (or secondary phases). The volume averaged mass and momentum conservation equations are as follows, respectively:

$$\frac{\partial}{\partial t}\left(\varepsilon_q \rho_q\right) + \nabla.\left(\varepsilon_q \rho_q \overrightarrow{\boldsymbol{u_q}}\right) = S_q \tag{3.3}$$

$$\frac{\partial}{\partial t}\left(\varepsilon_q \rho_q \overrightarrow{\boldsymbol{u_q}}\right) + \nabla.\left(\varepsilon_q \rho_q \overrightarrow{\boldsymbol{u_q}} \otimes \overrightarrow{\boldsymbol{u_q}}\right) = -\varepsilon_q \nabla p + \nabla.\varepsilon_q \overline{\overline{\tau_q}} + \varepsilon_q \rho_q \overrightarrow{\boldsymbol{g}} + M_{G,L} \tag{3.4}$$

where q is the phase indicator, $q = L$ for the liquid phase, $q = G$ for the gas phase, ε_q is the volume fraction, ρ_q is the phase density, and u_q is the velocity of the qth phase, while S_q is a

source term. $M_{G,L}$ is the interaction force between the phases and $\varepsilon\rho g$ is the gravity force, while $\overline{\overline{\tau_q}}$ is the qth phase stress-strain tensor given by:

$$\overline{\overline{\tau_q}} = \varepsilon_q \mu_q \left(\nabla \overrightarrow{\boldsymbol{u_q}} + \nabla \overrightarrow{\boldsymbol{u_q}}^T \right) + \varepsilon_q \left(\lambda_q - \frac{2}{3}\mu_q \right) \nabla . \overrightarrow{\boldsymbol{u_q}} \overline{\overline{I}} \tag{3.5}$$

The liquid phase was modelled as incompressible hence its continuity (mass conservation) equation is simplified as follows:

$$\frac{\partial \varepsilon_L}{\partial t} + \nabla . (\varepsilon_L \rho_L \overrightarrow{\boldsymbol{u_L}}) = 0 \tag{3.6}$$

Interaction between the phases is generally accounted for through inclusion of the drag force while non drag forces such as the virtual mass and lift force can be neglected [83-85]. Momentum exchange between the phases was therefore accounted for by means of the drag force only in this research. The different drag models that have been used in this research are described in subsequent chapters.

3.4 Turbulence model

3.4.1 Overview of turbulence modelling methods

Turbulent flows are characterised by velocity fluctuations in which small scale and high frequency fluctuations may occur. It would therefore be too computationally expensive to simulate turbulent flows in detail, especially for high Reynolds number flows. Fortunately, it is not always necessary in most engineering applications to resolve all the details of the turbulent fluctuations. Instead, the small scale and high frequency fluctuations can be removed by manipulating the instantaneous (exact) governing equations to produce modified equations that are computationally less expensive to solve. However, the modified equations contain additional unknown variables that have to be determined using turbulence models.

The choice of turbulence model is crucial for successful CFD simulations. There are numerous turbulence models that have been proposed over the last few decades. In order to select a suitable turbulence model, one has to consider the type of flow that is to be modelled as well as its implications on the computational cost of the simulations. Selecting a particular turbulence model is therefore usually a trade-off between the required accuracy and the computational cost of the simulations.

The methods for turbulence modelling can be grouped in to three categories: Direct numerical simulation (DNS), Large-eddy simulation (LES), and Reynolds-averaged Navier-Stokes (RANS) equations. In DNS, the unsteady 3D Navier-Stokes equations are solved directly to resolve the turbulent flow. A turbulence model is therefore not required since the equations adequately describe the flow. However, DNS requires very dense computational grids and small time steps in order to resolve the entire range of length scales and time scales of the turbulent flow, especially at high Reynolds number. The computational cost of DNS is therefore too high for the method to be applied for industrial computations [71, 78].

On the other hand, Large-eddy simulation (LES) is another form of modelling approach which is less computationally expensive than DNS. In LES, the dynamics of the large turbulent eddies are computed while the smallest scales of the turbulence are unresolved. This is accomplished by space filtering of the unsteady Navier-Stokes equations to separate the larger eddies and eliminate the smaller eddies prior to the computations. The effects of the small unresolved eddies on the resolved flow (mean flow and large eddies) are then included by means of a sub-grid scale model. Since a coarser mesh is used in LES simulations than the mesh required for DNS, LES results in substantial savings in the computational cost of the simulations. However, LES simulations also require a very fine mesh and small time steps. The computational cost of LES is therefore still high compared with other turbulence models.

The most widely used turbulence models for routine engineering simulations are based on the Reynolds-averaged Navier-Stokes (RANS) equations. In this approach, the instantaneous Navier-Stokes equations are time-averaged to produce the RANS equations which are solved to obtain a time averaged or mean flow field. The RANS equations are derived by decomposing the instantaneous variables in the Navier-Stokes equations into a mean part and a fluctuating component and then time averaging the resulting equations to obtain a set of equations for the average flow field (RANS equations). The velocity components are decomposed into a mean part and a fluctuating component according to:

$$u_i = \overline{u_i} + u_i'$$ (3.7)

where $\overline{u_i}$ and u_i' are the mean and fluctuating components, respectively ($i = 1, 2, 3$). Similarly, the scalar quantities such as pressure and energy are decomposed into the following form:

$$\varphi = \overline{\varphi} + \varphi'$$ (3.8)

where φ represents any scalar quantity.

Substituting the decomposed form for the flow variables into the continuity and momentum equations (Navier-Stokes equations) and taking the time average produces the RANS equations. However, the Reynolds-averaged momentum equations contain additional unknowns ($-\rho\overline{u_i' u_j'}$) called Reynolds or turbulent stresses which represent the effects of turbulent fluctuations on the mean flow. The Reynolds stresses are subsequently determined with the help of a turbulence model. RANS turbulence modelling therefore involves the calculation of the mean flow while employing turbulence models to simulate the effect of turbulent fluctuations on the mean flow. RANS turbulence models are classified according to the number of additional transport equations that need to be solved together with the Reynolds averaged flow equations as outlined in Table 3.1 [71].

Table 3.1: RANS based turbulence models.

Number of additional transport equations	Turbulence model
Zero	Mixing length model
One	Sparlart – Allmaras model
Two	k-ϵ model
	k-ω model
	Algebraic stress model
Seven	Reynolds stress model

3.4.2   Choice of turbulence model for the present research

The turbulence model used in this research was selected following a thorough literature survey on CFD modelling of column flotation cells. Most of the studies have utilised the standard k-ϵ turbulence model to simulate turbulence in the continuous (liquid) phase [13, 14, 16, 86, 87] while others have assumed laminar flow conditions [11, 15]. However, the presence of turbulence resulting from bubble motion and the feed and air enterances near the top and bottom of the column has been suggested as the cause of the dispersion which is one of the reasons for mixing in flotation columns [66, 67, 88]. It is therefore necessary to consider turbulence in subsequent CFD models of column flotation.

For flows with recirculation, such as the flows encountered in flotation columns, the realizable k-ϵ turbulence model has been reported to perform better than the widely used

standard k-ϵ model [89]. The present research therefore employs the realizable k-ϵ turbulence model to account for turbulence in the continuous phase (water).

3.4.3   Realizable k-ϵ turbulence model

The k-ϵ model is based on the Eddy Viscosity concept. The Reynolds stresses are therefore related to the velocity gradients through the eddy or turbulent viscosity as presented in the following equation:

$$-\rho\overline{u_i'u_j'} = \mu_t\left(\frac{\partial \boldsymbol{u}_i}{\partial x_j} + \frac{\partial \boldsymbol{u}_j}{\partial x_i}\right) - \frac{2}{3}\left(\rho k + \mu_t\frac{\partial \boldsymbol{u}_k}{\partial x_i}\right)\delta_{ij} \qquad (3.9)$$

where μ_t is the eddy or turbulent viscosity, k is the turbulence kinetic energy and δ_{ij} is the Kronecker delta. The turbulent viscosity is then calculated from the turbulence kinetic energy (k) and the turbulence dissipation rate (ϵ). The k-ϵ model is therefore a two equation turbulence model since two additional transport equations must be solved for the turbulence kinetic energy (k) and dissipation rates (ϵ). For the realizable k-ϵ model, the turbulence kinetic energy (k) and turbulence dissipation rate equations are presented as follows:

$$\frac{\partial}{\partial t}(\rho k) + \frac{\partial}{\partial x_j}(\rho k\boldsymbol{u}_j) = \frac{\partial}{\partial x_j}\left[\left(\mu + \frac{\mu_t}{\sigma_k}\right)\frac{\partial k}{\partial x_j}\right] + G_k + G_b - \rho\epsilon - Y_M + S_k \qquad (3.10)$$

$$\frac{\partial}{\partial t}(\rho\epsilon) + \frac{\partial}{\partial x_j}(\rho\epsilon\boldsymbol{u}_j)$$
$$= \frac{\partial}{\partial x_j}\left[\left(\mu + \frac{\mu_t}{\sigma_\epsilon}\right)\frac{\partial\epsilon}{\partial x_j}\right] + \rho C_1 S\epsilon - \rho C_2\frac{\epsilon^2}{k + \sqrt{v\epsilon}} + C_{1\epsilon}\frac{\epsilon}{k}C_{3\epsilon}G_b + S_\epsilon \qquad (3.11)$$

where

$$C_1 = max\left[0.43, \frac{\eta}{\eta + 5}\right], \eta = S\frac{k}{\epsilon}, S = \sqrt{2S_{ij}S_{ij}} \qquad (3.12)$$

The quantities C_1 and $C_{1\epsilon}$ are empirical constants while σ_k and σ_ϵ are the turbulent Prandtl numbers for k and ϵ, respectively. S_k and S_ϵ are source terms. The term G_k represents the generation of turbulence kinetic energy due to velocity gradients while G_b is the turbulence kinetic energy due to buoyancy. Y_M is the contribution of the fluctuating dilatation in compressible turbulence to the overall dissipation rate. The eddy viscosity or turbulent viscosity, μ_t is then modelled as follows:

$$\mu_t = \rho C_\mu \frac{k^2}{\epsilon} \qquad (3.13)$$

The variable, C_μ is calculated from the following equation:

$$C_\mu = \frac{1}{A_0 + A_s \dfrac{kU^*}{\epsilon}}$$

where

$$U^* \equiv \sqrt{S_{ij}S_{ij} + \widetilde{\Omega_{ij}}\,\widetilde{\Omega_{ij}}}$$

$$\widetilde{\Omega_{ij}} = \Omega_{ij} - 2\epsilon_{ijk}\omega_k \qquad (3.14)$$

$$\Omega_{ij} = \overline{\Omega_{ij}} - \epsilon_{ijk}\omega_k$$

$$A_0 = 4.04$$

$$A_s = \sqrt{6}\cos\emptyset$$

$$\emptyset = \frac{1}{3}\cos^{-1}(\sqrt{6}W), W = \frac{S_{ij}S_{jk}S_{ki}}{S^3}, \tilde{S} = \sqrt{S_{ij}S_{ij}}, S_{ij} = \frac{1}{2}\left(\frac{\partial u_j}{\partial x_i} + \frac{\partial u_i}{\partial x_j}\right)$$

where $\overline{\Omega_{ij}}$ is the mean rate of rotation rate viewed in a rotating reference frame with angular momentum ω_k. The model constants for the Realizable k-ϵ turbulence model are summarized in Table 3.2.

Table 3.2: Turbulence model constants.

σ_k	σ_ϵ	C_1	C_2	C_μ	A_0	$C_{1\epsilon}$
1.0	1.2	Eq.(3.12)	1.9	Eq.(3.14)	4.0	1.44

3.4.4   Turbulence near the column wall

The presence of walls has a profound effect on the behaviour of turbulence in wall bounded turbulent flows. The near wall region is characterised by relatively larger viscous effects and rapid variation of the flow variables. Correct representation of the influence of walls on turbulent flows is therefore an important aspect of CFD simulations involving wall-bounded flows.

The near-wall region is divisible into three sublayers. In the innermost layer, the viscous sublayer, flow is almost laminar and molecular viscosity has a dominant effect on momentum transfer while turbulence plays a major role in the outer layer called the fully turbulent layer. Between the viscous sublayer and the fully turbulent layer is an interim region in which the

molecular viscosity and turbulence are equaly important. This interim layer is known as the buffer layer.

There are two main approaches that can be used to model the near wall region in CFD simulations. In the first approach, the viscosity affected inner region (viscous and buffer layers) is not resolved. Instead, semi-empirical formulae known as wall functions are used to bridge the viscosity affected region between the wall and the fully turbulent region. This approach saves considerable comuptational resources since the the viscosity affected near wall region is not resolved. The wall function approach was therefore used in the present research in order to minimise the computational cost of the simulations.

The standard wall functions used in this research are based on the work of Launder and Spalding [90]. The momentum boundary condition is then obtained from the law-of-the-wall for the mean velocity as follows:

$$U^* = \frac{1}{\kappa}\ln(Ey^*) \tag{3.15}$$

where U^* is the dimensionless velocity and y^* is the dimensionless distance from the wall. These parameters are given by the following expressions:

$$U^* \equiv U_P C_\mu^{1/4} k_P^{1/2} \tag{3.16}$$

$$y^* \equiv \frac{\rho C_\mu^{1/4} k_P^{1/2} y_P}{\mu} \tag{3.17}$$

In equations (3.15) to (3.17), κ is the Von Kármán constant ($= 0.4187$), E is an empirical constant ($= 9.793$), U_P is the mean velocity of the fluid at the near-wall node P, k_P is the turbulence kinetic energy at near-wall node P, y_P is the distance from point P to the wall, and μ is the dynamic viscosity of the fluid.

The second approach, the low Reynolds number model method, employs modified turbulence models which are used to resolve the inner layer up to the wall. The wall function approach and the low Reynolds number model approach are compared in Figure 3.1.

40

Wall function approach

Low Reynolds number model approach

Outer turbulent zone

Wall layer

Wall functions

Wall

Outer turbulent zone

Wall layer
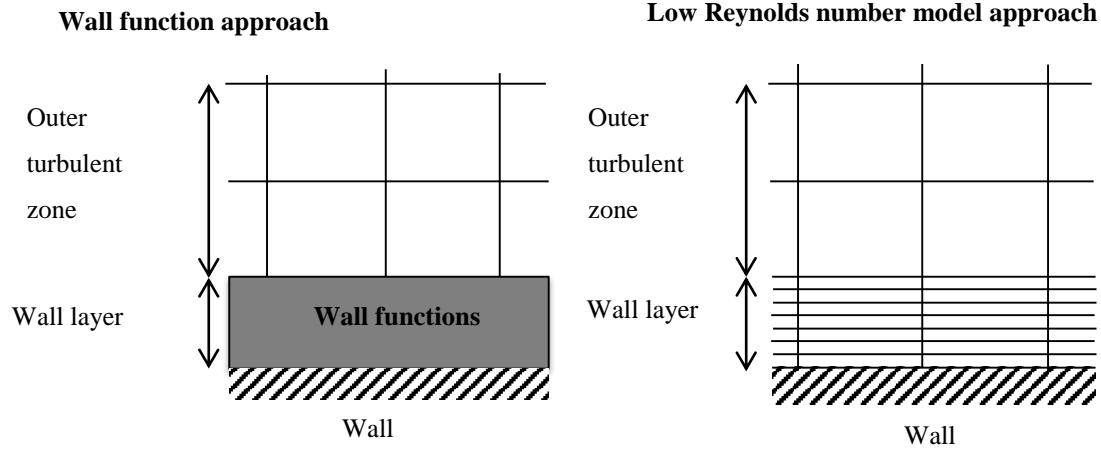
Wall

Figure 3.1: Comparison of the two approaches that can be used for near wall treatment in CFD simulations (Adapted from Bengt et al. [72]).

3.5   Numerical simulation set up and solution methods

The CFD simulations in this study were conducted using the software package ANSYS FLUENT 14.5. The FLUENT CFD solver employs the finite volume method to convert a general partial differential equation into an algebraic equation that can be solved numerically. In the finite volume method, the computational domain is discretised into a finite number of control volumes (cells) where general transport equations for mass, momentum, energy, etc are solved numerically to obtain the solution field. In FLUENT, the solution is stored at the centre of the control volumes. The general form of the transport equations for an arbitrary variable φ is presented as follows:

$$\frac{\partial}{\partial t}\int_V \rho\varphi dV + \oint_A \rho\varphi\boldsymbol{V}.d\boldsymbol{A} = \oint_A \Gamma_\varphi \nabla\varphi.d\boldsymbol{A} + \int_V S_\varphi dV \tag{3.18}$$

where ρ is the density, $\boldsymbol{V}$ is the velocity vector, A is the surface area, Γ_φ is the diffusion coefficient for φ, $\nabla\varphi$ is the gradient of φ, and S_φ is the source of φ per unit volume. The values of the quantity φ at the control volume faces, and the gradients of φ at the grid cells are required in order to solve the transport equations. In this research, the values of φ at the cell faces were extrapolated from the cell centres using either the First Order Upwind discretization scheme or the Quadratic Upstream Interpolation for Convective Kinetics (QUICK) scheme. In the First Order Upwind scheme, the value of φ at the control volume face is taken to be equal to the value of φ at the nearest upstream cell. The computations that are performed with this method are generally stable. However, the First Order Upwind

41

scheme is prone to numerical diffusion errors since it has only first order accuracy in terms of Taylor series truncation error (TSTE).

Alternatively, a higher order discretization scheme such as the QUICK scheme can be employed in order to minimize numerical diffusion errors. In the QUICK scheme, the value of φ at the cell face is obtained from a quadratic function passing through two bracketing nodes (on each side of the face) and a node on the upstream side. For a uniform grid, the value of φ at the cell face between bracketing nodes i and $i - 1$ and upstream node $i - 2$ is given by [71]:

$$\varphi_{face} = \frac{6}{8}\varphi_{i-1} + \frac{3}{8}\varphi_i - \frac{1}{8}\varphi_{i-2} \tag{3.19}$$

In terms of Taylor series truncation error the QUICK scheme is third order accurate on a uniform mesh. The pressure and the velocity components were coupled using the SIMPLE algorithm in an iterative process outlined in Figure 3.2. The Computations were performed using the University of Stellenbosch's Rhasatsha High Performance Computing (HPC) cluster: http://www.sun.ac.za/hpc.
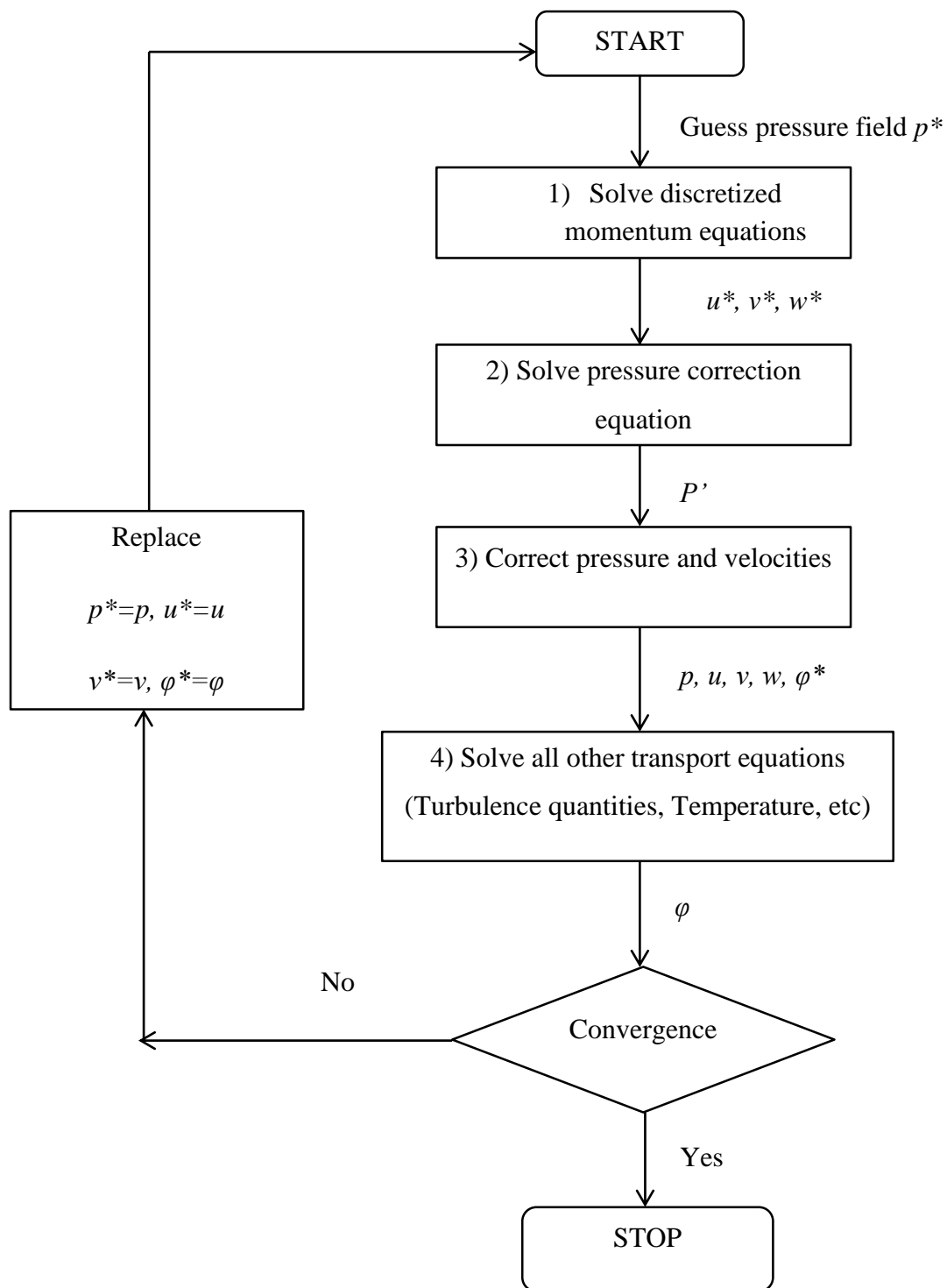
Figure 3.2: The SIMPLE algorithm (adapted from Versteeg and Malalasekera [71]).

Chapter 4   Numerical prediction of gas holdup and its axial variation in a flotation column

4.1   Introduction

In this chapter, Computational Fluid Dynamics (CFD) is applied to predict the average gas holdup and the axial gas holdup variation in the collection zone of a 0.91 m-diameter cylindrical pilot flotation column operated in batch mode. Gas holdup is one of the most important parameters affecting the metallurgical performance of the column. It is defined as the volumetric fraction (or percentage) occupied by gas at any point in a column [2]. Some studies have reported that gas holdup affected both the recovery and grade in industrial and pilot scale flotation columns [41, 42]. These studies reported a linear relationship between gas holdup and recovery. Linear relationships between gas holdup and the flotation rate constant have also been identified highlighting its effect on flotation kinetics [4, 43]. Other researchers have suggested that gas holdup could be used for control purposes in column flotation [44]. However, apart from its potential in control, gas holdup also has diagnostic applications, for example, the sudden drop in gas holdup that occurs when a sparger is damaged [44].

CFD modelling has been applied to predict the average gas holdup for the whole flotation column [13, 14]. However, the gas holdup has been observed to vary with height along the collection zone of the flotation column– increasing by almost 100% from the bottom to the top of the column [18, 45, 73]. The increase in gas holdup with height has been attributed to the hydrostatic expansion of bubbles [30, 73]

In spite of the reported increase in gas holdup along the column height, the CFD literature on column flotation does not account for this phenomenon. This could result in the under-prediction of gas holdup especially in cases where the available experimental measurements were taken near the top of the column. In an attempt to understand the observed axial variations in gas holdup, some researchers conducted experiments in which axial velocity profiles of single bubbles were measured [31]. On the other hand CFD is capable of predicting the entire flow fields of the various phases involved in the flotation process. The axial variation in bubble velocity can therefore be investigated with CFD in order to understand its relationship with the spatial gas distribution in the column.

44

The aim of the work discussed in this chapter was therefore to investigate the application of CFD for predicting not only the average gas holdup but also the axial gas holdup variation in the column. In this regard, CFD was used to model a cylindrical pilot column that was used in previous studies on axial gas holdup distribution [18, 45]. In addition, the axial velocity profiles of the gas phase were studied in order to explain the increase in gas holdup with height along the column.

4.2   Description of the column

The pilot flotation column was used in previous research by Gomez et al. [18, 45] to study gas holdup in the collection zone. It had a diameter of 0.91 m and a height of about 13.5 m. The experimental work was conducted with air and water only in a batch process. Air was introduced into the column through three Cominco-type spargers.

This column was selected for the present CFD modelling studies because axial gas holdup variation had been earlier identified and investigated for the column. The gas holdup data available for the column was therefore used to validate the CFD results in the present work.

In the experimental work [18, 45], the column was divided into three sections over which pressure measurements were taken. An illustration of the column is provided in Figure 4.1 to show the position of the pressure sensing devices and their respective distance from the top of the column.
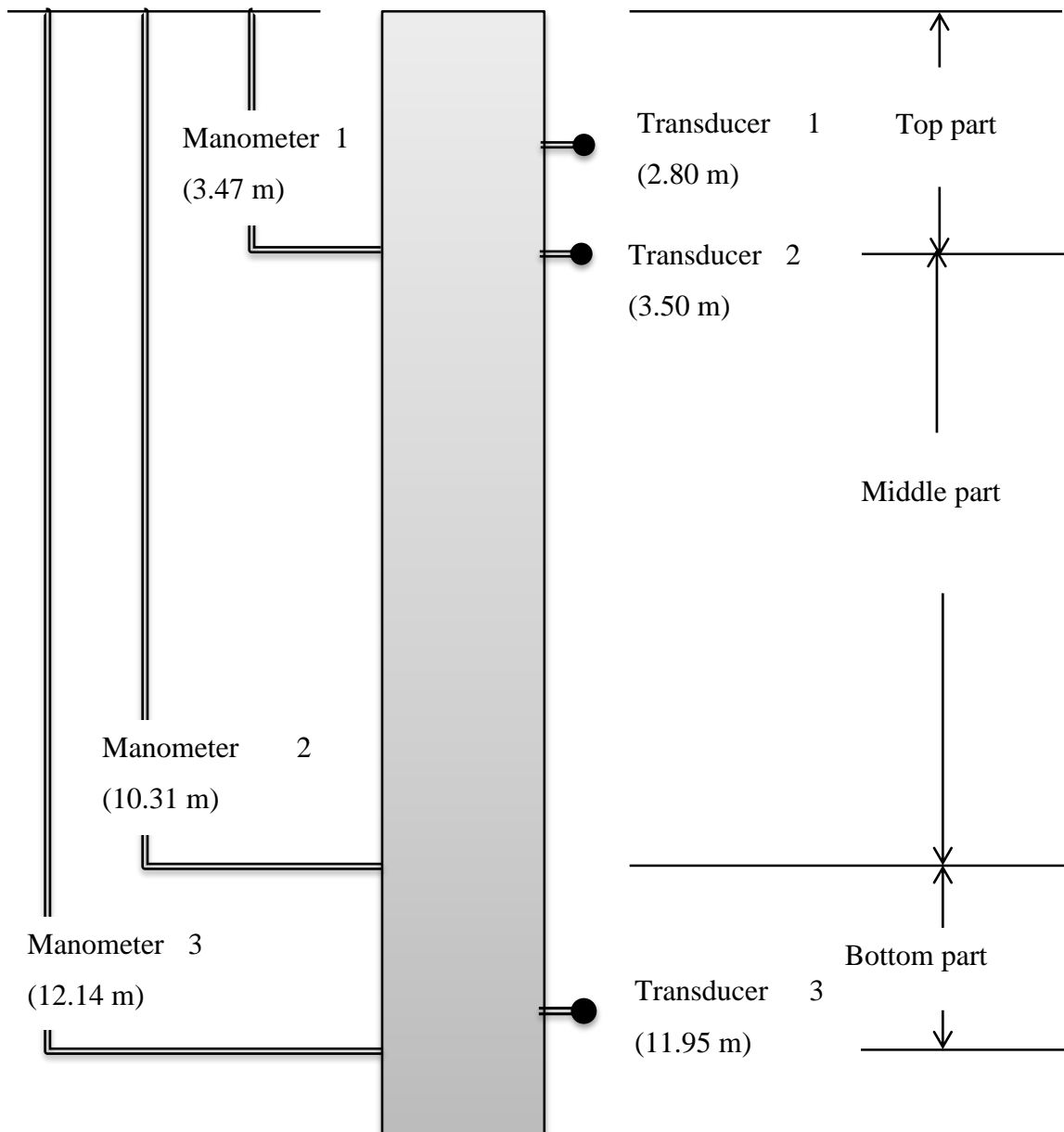
Figure 4.1: position of pressure sensing devices and their distance from the top of the column (adapted from Gomez et al. [18]).

For the air-water system the gas holdup can be determined from the pressure difference Δp between two points separated by a distance ΔH according to the following equation [18]:

$$\varepsilon_G = 100 \left[1 - \frac{\Delta p}{\Delta H}\right] \qquad (4.1)$$

The gas holdup in the experimental work was therefore calculated from pressure measurements taken over the three sections using pressure transducer 2 for the top part, water manometers 1 and 2 for the middle part, and water manometers 2 and 3 for the bottom part.

The average gas holdup for the whole column was calculated using the readings from pressure transducer 3.

The experimental measurements were conducted for different superficial gas velocities namely, J_g; 0.72, 0.93, 1.22, 1.51, 1.67, 2.23, and 2.59 cm/s. Superficial gas velocity is defined as the volumetric flow rate of gas divided by the column cross-sectional area [2] and is measured in cm/s.

4.3   CFD Model description

4.3.1   Model geometry and mesh

The geometry of this column was subsequently developed considering the three sections as shown in Figure 4.2. CFD Simulations were then conducted for five different superficial gas velocities, $J_g = 0.72 – 1.67$ cm/s.
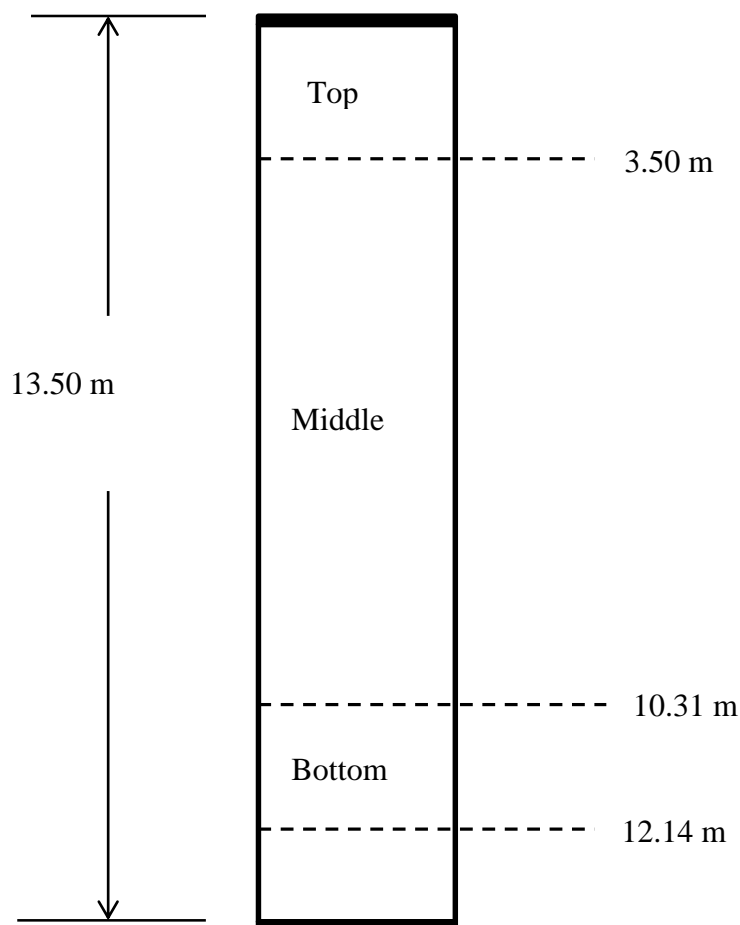
Figure 4.2: CFD model geometry of the experimental pilot column.

47

The meshing application of ANSYS Workbench was used to generate the mesh over the model geometry. The mesh was generated using the Sweep method which creates a mesh comprising mainly hexahedral elements. The computational mesh of the column is presented in Figure 4.3. Grid dependency studies were conducted in order to eliminate the possibility of errors resulting from an unsuitable mesh size. The mesh was therefore progressively refined from an initially coarse mesh of cell size equal to 5 cm and number of cells equal to 97188 until there were no significant changes in the simulated axial water and bubble velocity profiles. The different mesh sizes that were investigated are presented in Table 4.1 while the axial velocity profiles obtained for these meshes are shown in Figure 4.4 and Figure 4.5. It can be seen that the mean axial water and bubble velocity profiles do not change significantly from mesh 3 up to mesh 5. However, the axial velocity for mesh 5 is slightly higher than mesh 3 and mesh 4. Therefore, based on these results, mesh 4 comprising 884601 elements with cell size equal to 2.25 cm was used for all subsequent simulations in this study considering it as a reasonable trade off between the required accuracy and the computational time of the simulations. A Minimum Orthogonal Quality of 0.840 was obtained for the mesh.

Top view   Side view
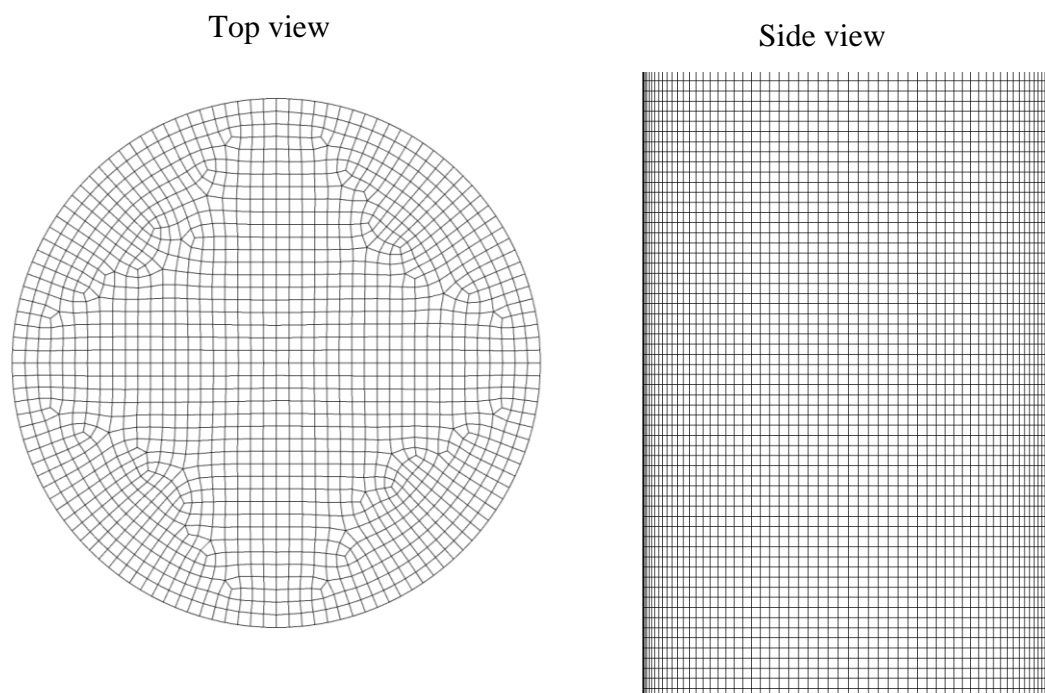
Figure 4.3: CFD mesh for the 0.91 m diameter cylindrical column.

Table 4.1: Mesh sizes investigated in the grid dependence study.

Identification	Element (Cell) Size in cm	Number of elements	Number of nodes
Mesh 1 (coarse mesh)	5.00	97188	106038
Mesh 2	3.75	203280	218764
Mesh 3	2.70	528150	555912
Mesh 4	2.25	884601	925328
Mesh 5	1.85	1611132	1667575
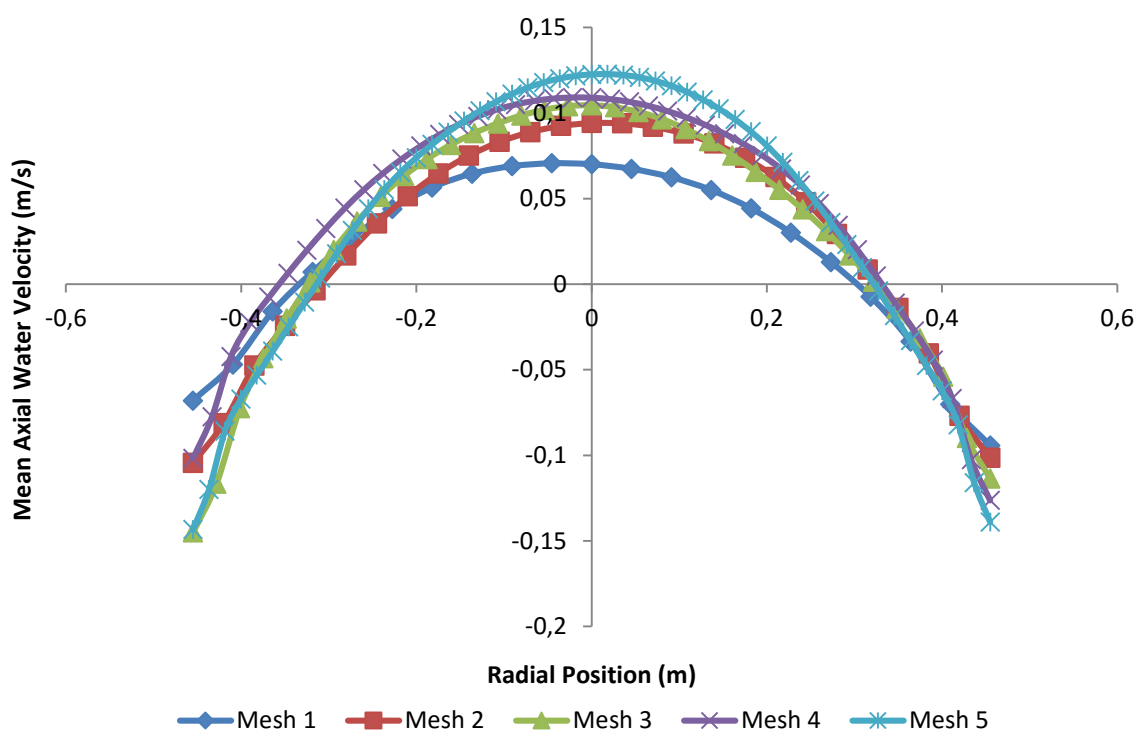
Figure 4.4: Simulated axial water velocity profiles for the investigated mesh sizes (Superficial gas velocity, J_g = 1.51 cm/s).
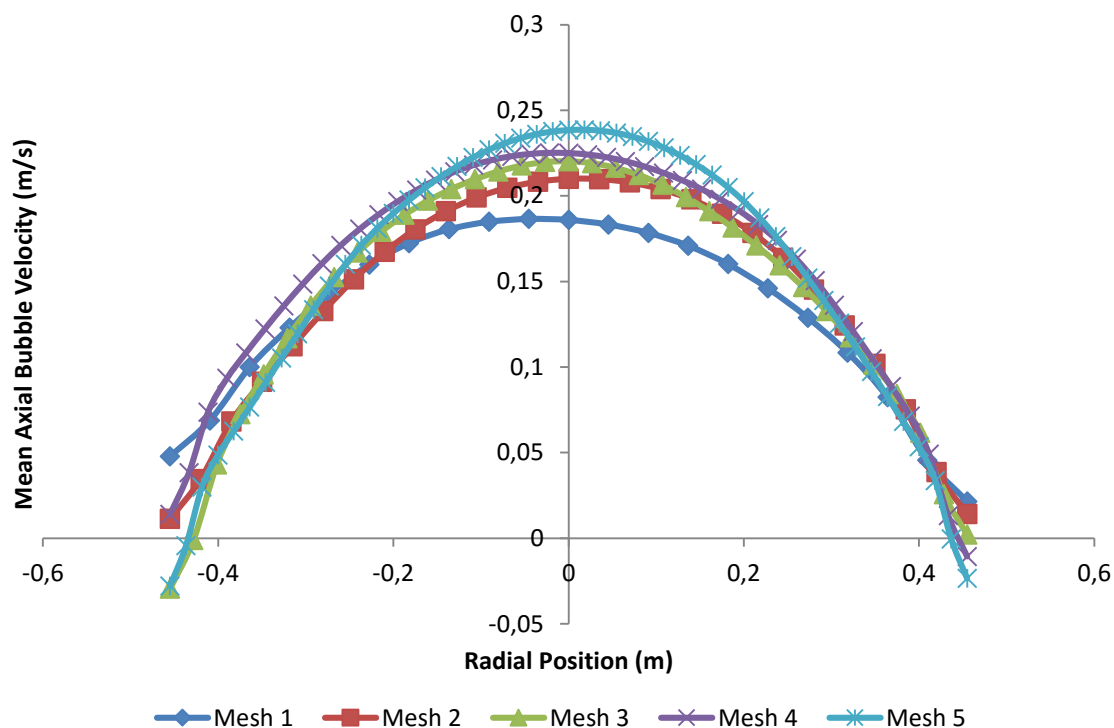
Figure 4.5: Simulated bubble velocity profiles for the different mesh sizes (Superficial gas velocity, J_g = 1.51 cm/s).

4.3.2   Boundary conditions

Air bubbles were introduced into the column through mass and momentum source terms applied at the bottom of the column in the CFD model. Cominco spargers like the ones that were used in the simulated column are known for their uniform bubble distribution over the entire column cross-section [26-28]. The air bubbles were therefore introduced over the entire column cross section in the CFD model without including the physical spargers in the model geometry. The top of the column was modelled as a sink for the air bubbles while no slip conditions were applied at the column wall for both the water (primary phase) and the air bubbles (secondary phase).

4.3.3   Multiphase Model

A two-fluid model has been recommended for studying large-scale flow structures occurring in pilot and industrial scale bubble columns due to its relatively lower computational cost [80]. An Eulerian-Eulerian two fluid model was therefore selected in the present research considering the large size of the pilot flotation column that was to be modelled. In the Eulerian-Eulerian approach both phases, i.e., the primary phase and the secondary phase, are treated as inter-penetrating continua. Momentum and mass conservation equations are then

solved for each of the phases separately. Interaction between the phases was accounted for through inclusion of the drag force between phases. The Eulerian-Eulerian model has been reviewed in Chapter 3. The continuity and momentum equations for the Eulerian-Eulerian model are therefore not repeated here and are given in Chapter 3 as equation (3.3) and equation (3.4), respectively.

In the present research, water was modelled as the primary phase while air bubbles were treated as the secondary phase. The volume fraction (or gas holdup) of the secondary phase was calculated from the mass conservation equations as:

$$\frac{1}{\rho_{rG}}\left(\frac{\partial}{\partial t}(\varepsilon_G \rho_G) + \nabla . (\varepsilon_G \rho_G \overrightarrow{u_G}) = S_G\right) \tag{4.2}$$

where ρ_{rG} is the phase reference density, or volume averaged density of the secondary phase in the solution domain. The volume fraction of the primary phase was calculated from the secondary phase one, considering that the sum of the volume fractions is equal to 1. In order to obtain the correct local distribution of the gas phase, previous researchers implemented compressibility effects in their CFD models using the ideal gas law [22, 32]. Similarly, the axial gas holdup variation in the present study was accomplished in the CFD simulations by applying the ideal gas law to compute the density of the secondary phase (ρ_G) as a function of the local pressure distribution in the column according to the following equation:

$$\rho_G = \frac{p_{op} + p}{\frac{R}{M_w}T} \tag{4.3}$$

where p is the local relative (or gauge) pressure predicted by CFD, p_{op} is operating pressure, R is the universal gas constant, M_w is the molecular weight of the gas, and T is temperature.

4.3.3.1 *Drag force formulations*
Generally, the drag force per unit volume for bubbles in a swarm is given by [84]:

$$\vec{F}_D = \frac{3\varepsilon_G \varepsilon_L}{4}\left(\frac{\rho_L}{d_B}\right) C_D |\overrightarrow{u_G} - \overrightarrow{u_L}|(\overrightarrow{u_G} - \overrightarrow{u_L}) \tag{4.4}$$

where C_D is the drag coefficient, d_B is the bubble diameter, and $\overrightarrow{u_G} - \overrightarrow{u_L}$ is the slip velocity. The drag force formulation includes the correction for bubble swarms and local volume fractions of the phases [91]. There are several empirical correlations for the drag coefficient, C_D, in the literature. The drag coefficient is normally presented in these correlations as a

function of the bubble Reynolds number (*Re*). A constant value of the drag coefficient may also be used [92, 93]. The bubble Reynolds number is defined as:

$$Re = \frac{\rho_L |\overrightarrow{\boldsymbol{u_G}} - \overrightarrow{\boldsymbol{u_L}}| d_B}{\mu_L} \qquad (4.5)$$

In the present research, simulations were carried out with three different drag coefficients. The first set of simulations was performed using the Universal drag coefficient [94]. Subsequent simulations were then conducted with the Schiller-Naumann [95] and Morsi-Alexander [96] drag coefficients in order to compare the suitability of the three drag models for the average and axial gas holdup computation in the flotation column. The equations describing the three drag coefficients are outlined in Table 4.2.

The drag coefficient values calculated from the equations presented in Table 4.2 are plotted in Figure 4.6 as a function of the bubble Reynolds number for $0 \leq Re < 1000$. Typical bubble sizes used in column flotation range from 0.5 – 2 mm corresponding to $1 << Re < 500$ [97]. For the 1 mm bubble size used in the simulations in this study, the *Re* value calculated using equation (4.5) was 115.5. Details of the drag coefficient calculations for the *Re* versus C_D graphs are provided in Appendix 4 (A – C). From Figure 4.6, it can be seen that increasing *Re* causes the drag coefficient to decrease exponentially towards a constant value. A constant C_D value of about 0.44 is therefore applicable for the Schiller-Naumann drag coefficient for $Re > 1000$.

On the other hand, the formulation for the Morsi-Alexander and Universal drag coefficients will change depending on the bubble Reynolds number. For the Morsi-Alexander drag model, the constants A, B, and C will be varying as *Re* changes from one range to another as outlined in Table 4.2. Likewise, the universal drag coefficient is defined differently for flows that are categorized to be either in the viscous regime, the distorted bubble regime, or the strongly deformed capped bubbles regime as determined by the Reynolds number.

At the moderate superficial gas velocities simulated in this study, the viscous regime ($0 \leq Re < 1000$) conditions apply. The equation presented in Table 4.2 is the one which is applicable when the prevailing flow is in the viscous regime. From Figure 4.6, it can also be observed that the Universal and the Schiller-Naumann drag models will give similar values of C_D in the viscous regime. Further details about the universal drag laws are available in a recent multiphase flow dynamics book [94].

Table 4.2: The drag coefficients that were used in the CFD simulations in the present study.

Schiller and Naumann[95]	$C_D = \begin{cases} \dfrac{24}{Re}[1 + 0.15Re^{0.687}] \; for \; Re < 1000 \\ 0.44 \; for \; Re > 1000 \end{cases}$	(4.6)
Morsi and Alexander[96]	$$C_D = \frac{A}{Re} + \frac{B}{Re^2} + C$$ $\begin{array}{llll} & A & B & C \\ Re < 0.1 & 24 & 0 & 0 \\ 0.1 \le Re < 1 & 22.73 & 0.0903 & 3.69 \\ 1 \le Re < 10 & 29.1667 & -3.8889 & 1.222 \\ 10 \le Re < 100 & 46.5 & -116.67 & 0.6167 \\ 100 \le Re < 1000 & 98.33 & -2778 & 0.3644 \\ 1000 \le Re < 5000 & 148.62 & -4.75 \times 10^4 & 0.357 \\ 5000 \le Re < 10000 & -490.546 & 5.787 \times 10^5 & 0.46 \\ 10000 \le Re < 50000 & -1662.5 & 5.4167 \times 10^6 & 0.5191 \\ Re \ge 50000 & 0 & 0 & 0.44 \end{array}$	(4.7)
Universal drag[94]	$$C_{D_{vis}} = \frac{24}{Re}(1 + 0.1Re^{0.75})$$ where Re is the relative Reynolds number for the primary phase L and the secondary phase G obtained on the basis of the relative velocity of the two phases as:- $$Re = \frac{\rho_L|\overrightarrow{\boldsymbol{u_L}} - \overrightarrow{\boldsymbol{u_G}}|d_B}{\mu_e}$$ where μ_e is the effective viscosity of the primary phase considering the effects of the secondary phase. $$\mu_e = \frac{\mu_L}{1 - \varepsilon_G}$$	(4.8)

C_D as a function of Re

Figure 4.6: Drag coefficient C_D as a function of bubble Reynolds number Re for $0 \leq Re < 1000$.

4.3.4 Turbulence model

Turbulence was modelled using the realizable k-ϵ turbulence model which is a RANS (Reynolds- Averaged Navier-Stokes) based model. In the RANS modelling approach, the instantaneous Navier-Stokes equations are replaced with the time averaged Navier-Stokes (RANS) equations which are solved to produce a time averaged flow field. The averaging procedure introduces additional unknowns, the Reynolds stresses. The Reynolds stresses are subsequently resolved by employing Boussinesq's eddy viscosity concept where the Reynolds stresses (or turbulent stresses) are related to the velocity gradients according equation (3.9). The eddy (turbulent) viscosity is then modelled as outlined in equation (3.13) and equation (3.14).

4.3.5 Numerical solution methods

Momentum and volume fraction equations were discretized using the QUICK scheme, while First Order Upwind was employed for turbulence kinetic energy and dissipation rate

discretization. The QUICK scheme provides up to third-order accuracy in the computations, while First Order Upwind is easier to converge. The time step size was 0.05s.

For simulations that were difficult to converge the First Order Upwind scheme was used in place of the QUICK scheme until convergence. In some of such cases the time step size was changed from 0.05s to 0.025s to enhance convergence. The simulations were run up to flow times of between 400s and 540s since the bubble residence time in a similar sized column was measured to be between 4-5 minutes [98].

4.4   Results and discussion

Two sets of CFD simulations were carried out in this study to predict the average gas holdup and the axial gas holdup variation in the flotation column. The first set of simulations was conducted using the Universal drag coefficient to calculate the drag force between the air bubbles and the liquid. Another set of simulations was then performed with the Schiller-Naumann and the Morsi-Alexander drag coefficients in order to compare the suitability of the different drag models for predicting gas holdup in the column. The physical parameters used in the simulations are defined in Table 4.3: Parameters used in the CFD simulations.. The simulation results obtained with the Universal drag are presented first followed by a comparison of the results obtained with the three different drag coefficients.

Table 4.3: Parameters used in the CFD simulations.

Liquid phase (water)	
Density	998.2 kg/m^3
Viscosity	0.001 kg/m-s
Gas phase (air bubbles)	
Density	1.225 kg/m^3; for compressible flow, density was calculated using the Ideal Gas law
Viscosity	1.789 x 10^{-5} kg/m-s
Bubble diameter	1 mm

4.4.1   Simulation results with Universal drag coefficient

4.4.1.1   *Liquid flow field*

The predicted velocity vectors of the liquid (water) in the column are shown in Figure 4.7. The liquid velocity field shows a typical circulating flow in the column in which the liquid is rising in the centre and descending near the walls of the column. This compares well with

55

earlier CFD predictions for flotation columns [11, 13] as well as experimental data on bubble columns [48, 50].

The type of liquid circulation where upward flow exists in the centre while downward flow prevails near the column walls is referred to as gulf-stream circulation [49]. This liquid circulation pattern has been attributed to density differences arising from non-uniform radial gas holdup profiles [48, 49].

The simulated axial velocity profile of water at the mid-height position in the column is presented in Figure 4.8. It can be seen in this Figure that the water velocity is positive (upward) in the centre of the column and negative (downward) near the wall hence confirming the gulf-stream circulation pattern in the column. The axial water velocity profile shown in Figure 4.8 is asymmetrical. Asymmetrical velocity profiles have also been reported by other researchers who conducted experimental studies on bubble columns [50].

| Bottom part | Middle part | Top part |
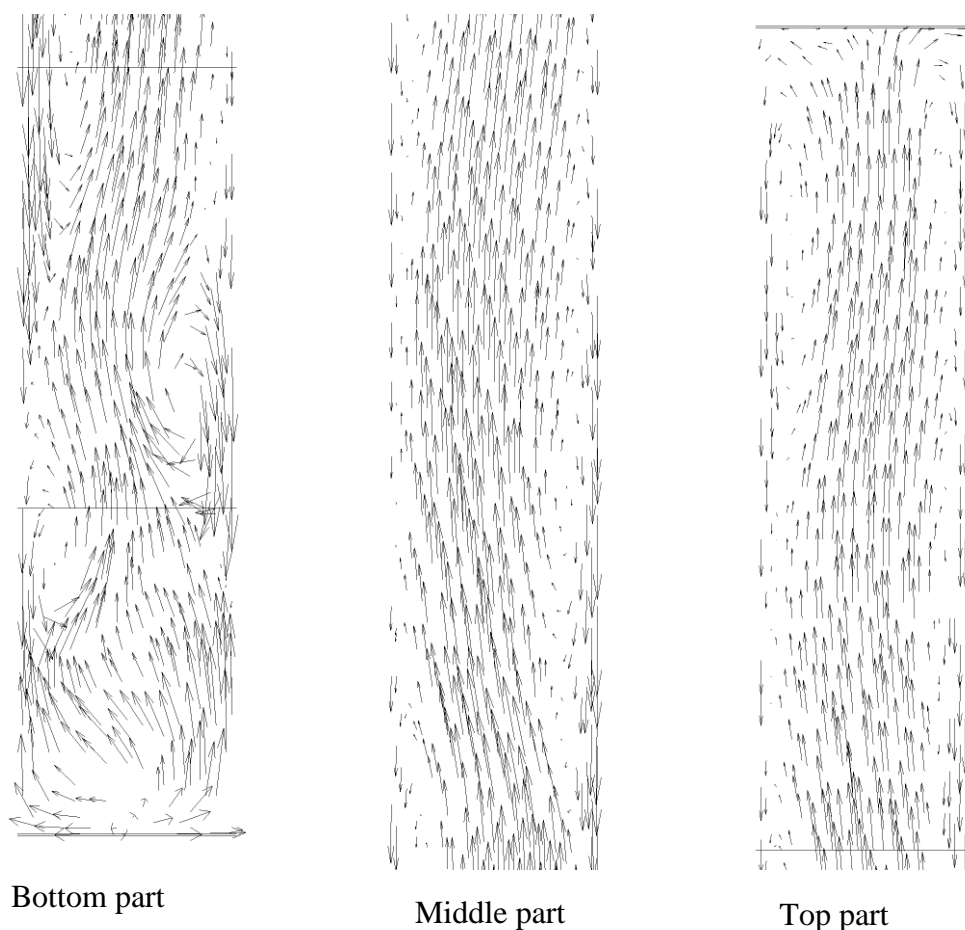
Figure 4.7: Vectors showing the predicted flow of water in the column (superficial gas velocity, J_g = 0.93 cm/s).

56
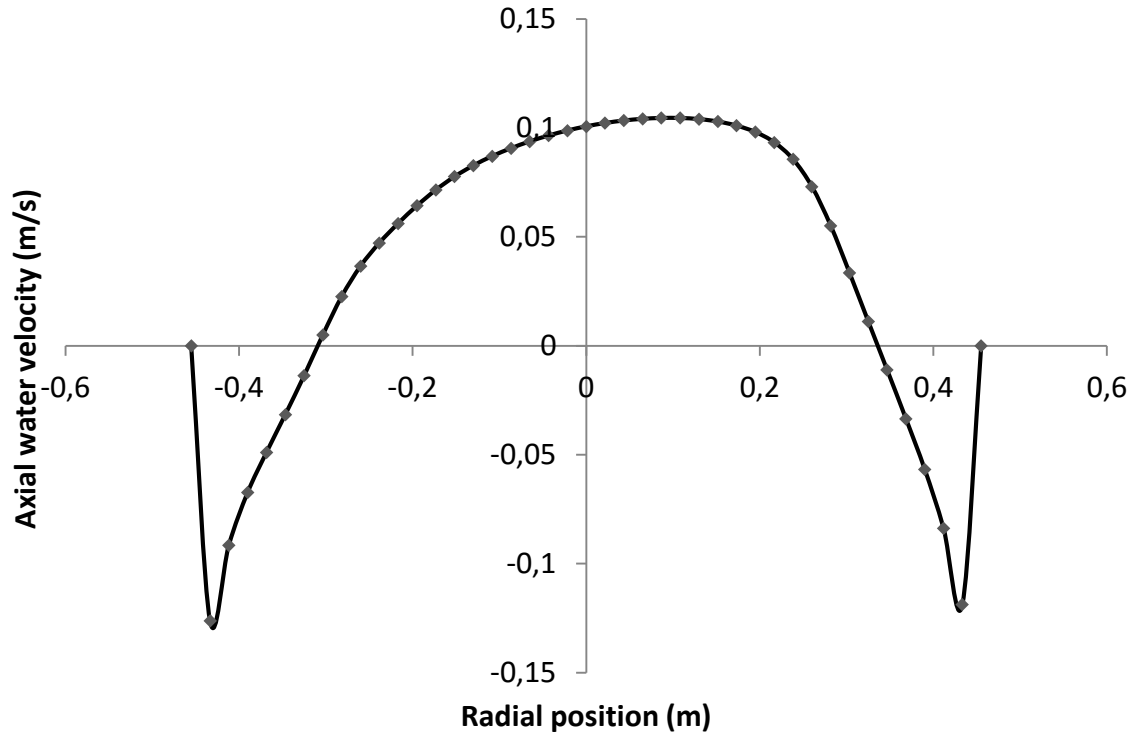
Figure 4.8: Axial water velocity profile at column mid-height position (Height = 6.75 m). Superficial gas velocity, J_g = 0.93 cm/s.

4.4.1.2   Gas holdup distribution in the column

Figure 4.9 shows the time averaged air volume fraction (gas holdup) contours in the column obtained from the CFD simulations. The gas holdup increases from the bottom to the top of the column as shown in the Figure. The gas holdup at the top is almost twice the gas holdup value at the bottom of the column. The increase in gas holdup with increasing height in the column is achieved in CFD simulations by applying the ideal gas model to compute the density of the air bubbles as a function of the predicted pressure field. The axial increase in gas holdup has been attributed to the hydrostatic expansion of bubbles due to the decrease in hydrostatic pressure [22, 73]. Figure 4.9 also shows a radial variation in gas holdup in which the highest gas holdup occurs at the centre of the column.

57
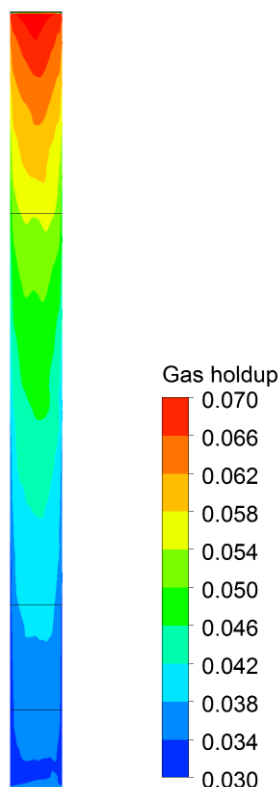
Figure 4.9: Gas holdup contours – time averaged air volume fraction (J_g = 0.93 cm/s).

The CFD model was further tested for the case in which the effect of the hydrostatic pressure is neglected. In this case, the air bubbles were assigned a constant density of 1.225 kg/m^3. In other words, simulation results in which the air bubbles were modelled as incompressible (without hydrostatic 'expansion') were compared with the results in which compressibility effects are accounted for using the ideal gas law. This was done in order to determine whether there was no other source of change in axial gas holdup. The axial gas holdup profiles of the two cases are compared in Figure 4.10. The case with compressibility effects shows an axial gas holdup profile in which the gas holdup increases by at least 100% from bottom to top along the height of the column. On the other hand, the incompressible case does not show significant increase in axial gas holdup. The decreasing hydrostatic pressure therefore plays the major role in creating an axial gas holdup profile in flotation columns.
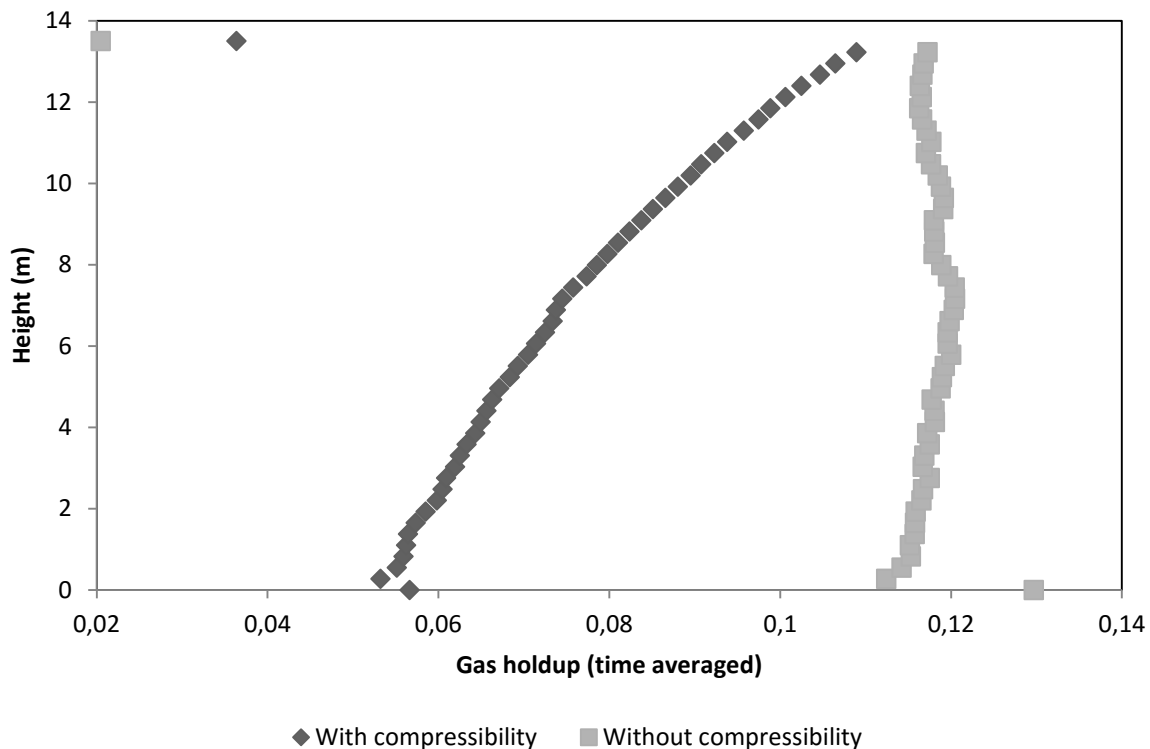
Figure 4.10: Comparison of CFD simulations with hydrostatic pressure effects (compressibility) and the case without hydrostatic bubble 'expansion' (incompressible); $J_g = 1.51$ cm/s.

4.4.1.3 *Comparison of predicted gas holdup with experimental data*

The gas holdup was obtained from CFD simulations as a volume-weighted average volume fraction of the air bubbles. The predicted average gas holdup is the net volume-weighted average volume fraction for the three sections (bottom, middle, and top) of the column while axial gas holdup was determined from the local value of air volume fraction in each of the three sections. Figure 4.11 is the parity plot comparing the simulated (predicted) average gas holdup against the experimental gas holdup measurements [18]. The CFD predictions seem to be in good agreement with the experimental data since all the points lie close to the line y = x as shown in the Figure.
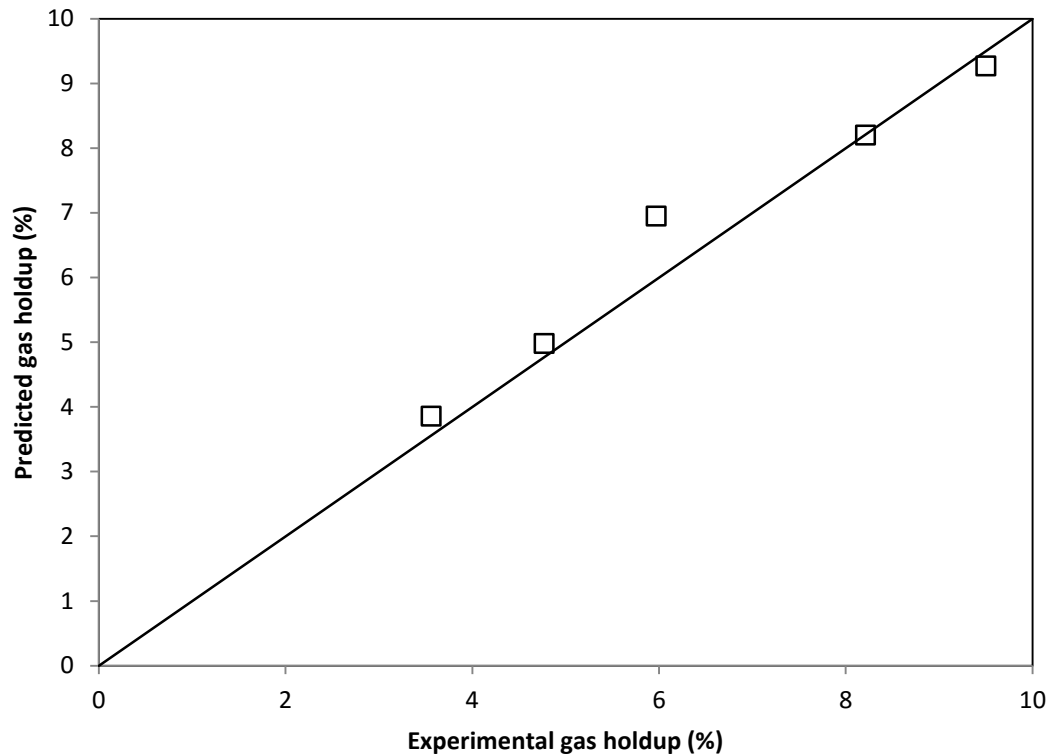
Figure 4.11: Parity plot comparing the predicted (CFD) average gas holdup and the experimental data [18].

The axial gas holdup predicted for each of the three sections (bottom, middle, and top) of the column is also compared against experimental data in Figure 4.12 – Figure 4.15. The increase of gas holdup along the column height can be observed both in the CFD predictions and experimental data as shown in these Figures.

The axial gas holdup prediction for the middle part of the column gave an excellent comparison with experimental data while the top part was slightly under-predicted for the higher superficial gas velocities (J_g = 1.51 cm/s and 1.67 cm/s). On the other hand, it can be observed from Figure 4.12 – Figure 4.15 that the axial gas holdup is over-predicted for the bottom part of the column especially at lower superficial gas velocities (J_g = 0.72 and 0.93 cm/s). This is because the CFD model applies a constant bubble size of 1 mm and does not account for bubble coalescence and break up in the column. At lower superficial gas velocities bubble coalescence will be the dominant process compared to bubble break up [99], hence the experimental gas holdup in the bottom part of the column will be lower than the predicted one. However, with increasing Superficial gas velocity bubble break up probably reduces the average bubble size to around the 1 mm value used in the simulations,

60

hence the observed improvement in axial gas holdup prediction for the bottom part of the column at higher superficial gas velocities (i.e., for J_g = 1.51 cm/s and 1.67 cm/s).

Axial gas holdup at J_g = 0.72 cm/s
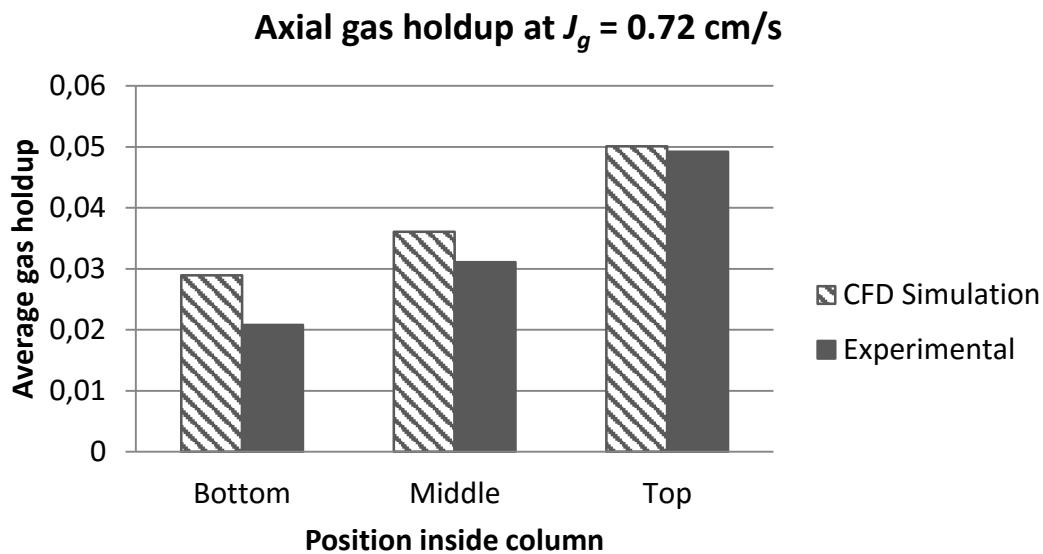
Figure 4.12: Comparison of the predicted axial gas holdup profile with experimental data [18]; J_g = 0.72 cm/s.

Axial gas holdup at J_g = 0.93 cm/s
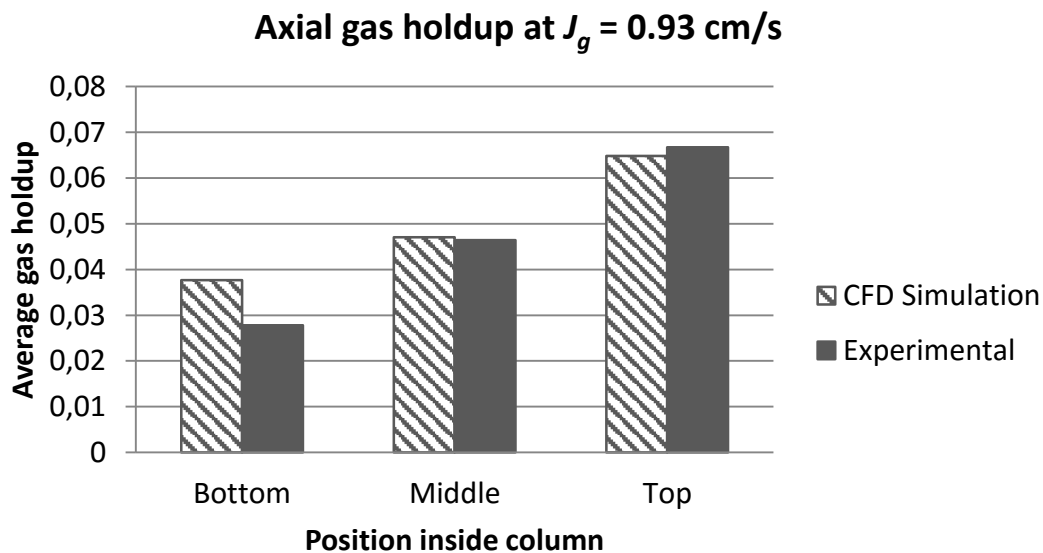
Figure 4.13: Comparison of the predicted axial gas holdup profile with experimental data [18]; J_g = 0.93 cm/s.

61

Axial gas holdup at J_g = 1.51 cm/s
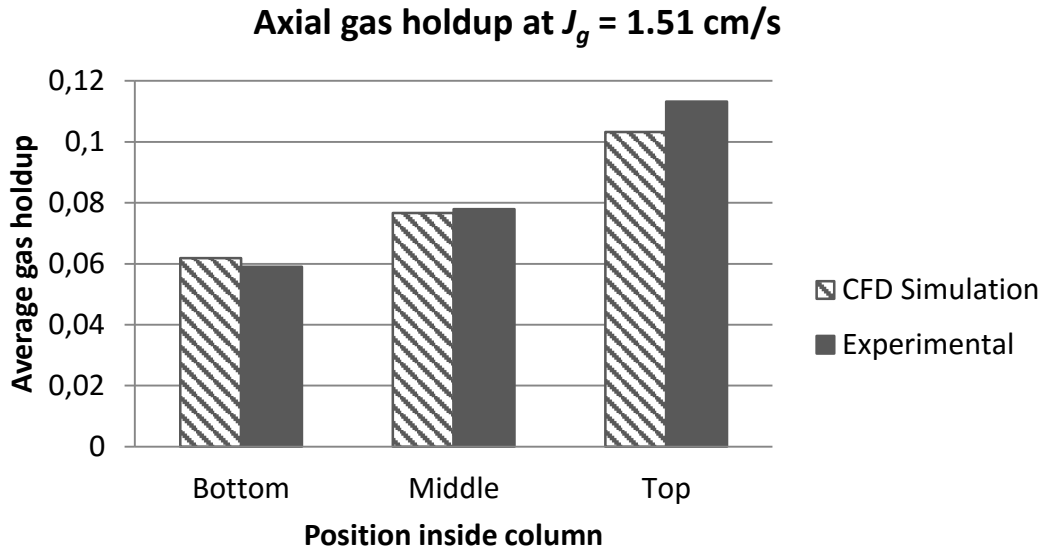
Figure 4.14: Comparison of the predicted axial gas holdup profile with experimental data [18]; J_g = 1.51 cm/s.

Axial gas holdup at J_g = 1.67 cm/s
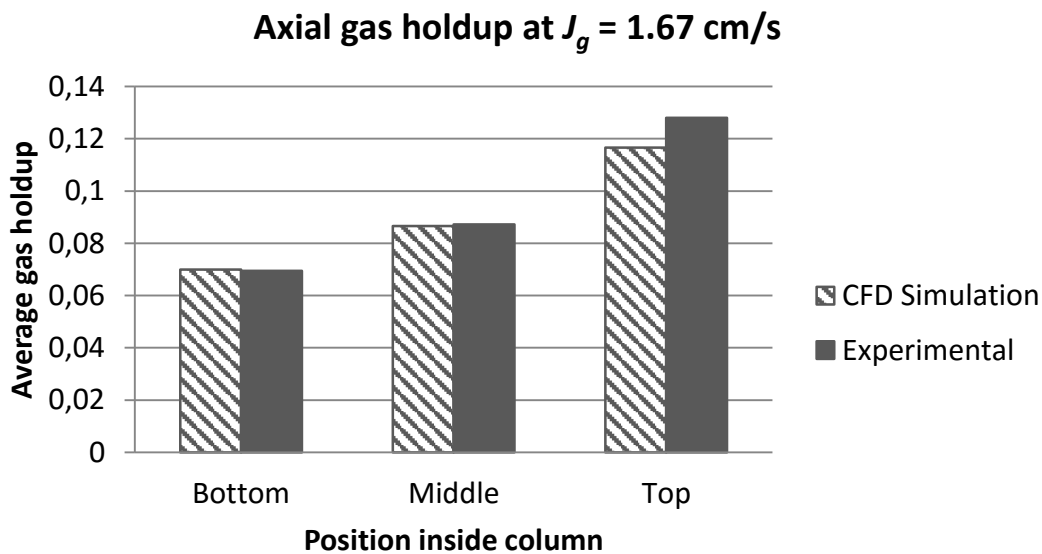
Figure 4.15: Comparison of the predicted axial gas holdup profile with experimental data [18]; J_g = 1.67 cm/s.

4.4.1.4   Bubble velocities

Table 4.4 shows the volume weighted average velocity magnitude of air bubbles obtained from the CFD simulations at different superficial gas velocities. For the constant bubble size of 1 mm used in the CFD simulations, the average velocity magnitude seems to decrease

slightly with increasing superficial gas velocity. This is perhaps due to the increase in average gas holdup resulting from increasing the superficial gas velocity [100-102].

Table 4.4: Predicted average velocities of air bubbles at different superficial gas velocities.

Superficial gas velocity (cm/s)	Average Velocity Magnitude of air bubbles (cm/s)
0.72	12.79
0.93	12.33
1.22	11.78
1.51	11.84
1.67	11.61

The simulated axial velocity profiles of air bubbles at different heights in the column are shown in Figure 4.16 for J_g = 1.51 cm/s. It can be seen that the axial bubble velocity decreases with height along the column. Previous research on axial velocity profiles of single bubbles also identified similar bubble behaviour along the column height due to the progressive increase in the drag coefficient resulting from surfactant-induced changes at the bubble surface [31]. However, since the effects of surfactants on bubble surfaces are not accounted for in the present CFD model, the observed axial variation in bubble velocity in this case must have its origins in some other mechanism, possibly the increase in the drag force resulting from the increase in gas holdup with height along the column. The observed decrease in bubble velocity with column height could result in a further increase in axial gas holdup variations. Figure 4.16 also also shows a change in the shape of the axial bubble velocity profile from a parabolic shape at the bottom and in the middle to a more uniform profile at the top of the column where the flow turbulence is fully developed.

In Figure 4.17, the axial velocity of bubbles is plotted against height along the column axis. The profile obtained shows three stages of the velocity profile similar to the three-stage profile described by Sam et al. [31] for single bubbles rising in a 4 m water column in the presence of frother. In the initial stage, the bubble velocity increases rapidly (acceleration stage) to reach a maximum velocity of 23.2 cm/s at height approximately 2.7 m in the column. This value compares favourably with the maximum velocity of 25.0 ± 0.4 cm/s reported by Sam et al. [31] for bubbles of 0.9 mm diameter. In the second stage (deceleration

stage), the bubble velocity is decreasing until at height approximately 8.5 m. After that the bubble velocity appears to fluctuate around an average velocity of about 11.5 cm/s (constant velocity or terminal velocity stage). This value can be compared to the terminal velocities of between 11.0 and 12.0 cm/s observed by Sam et al. [31] for similar bubble size (0.9 mm bubble diameter).

An interesting observation here is that in spite of the fact that our CFD model does not account for the effects of frother, the results in Figure 4.17 are quiet similar to the three-stage profile described by Sam et al. [31] for bubbles rising in water in the presence of frother where the decreasing velocity in stage 2 was attributed to progressive adsorption of surfactant molecules as the bubble rises. On the other hand, equation (4.4) indicates that the drag force on the air bubbles should increase with increasing volume fraction of the bubbles (or gas holdup). The deceleration of bubbles observed in the CFD results could therefore be related to the increase in gas holdup along the column axis due to subsequent increases in the drag force.
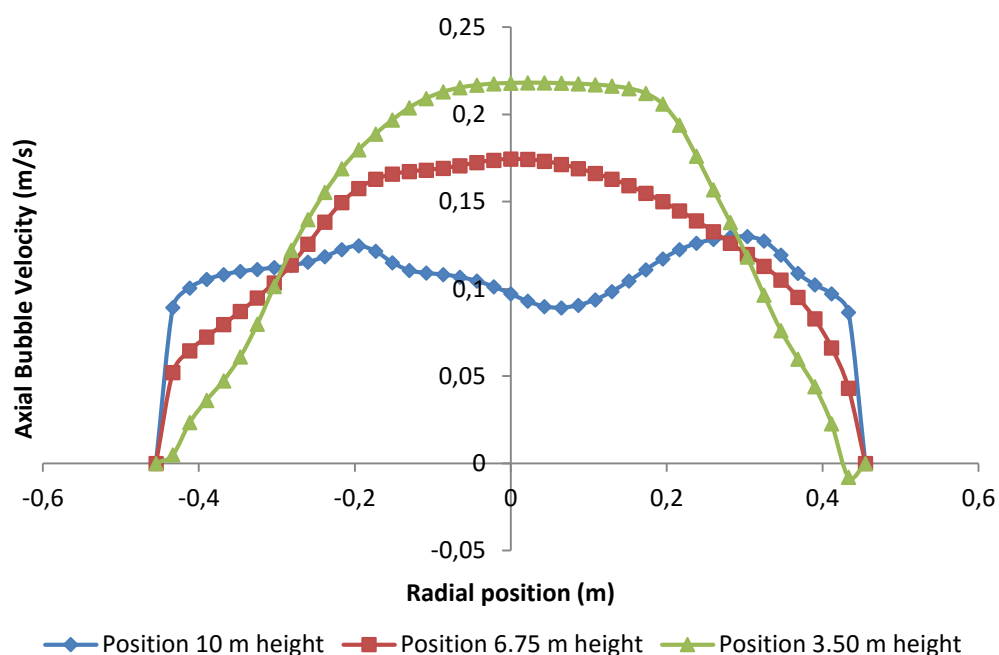
Figure 4.16: Axial velocity profiles of air bubbles at three different heights along the column; $J_g = 1.51$ cm/s.
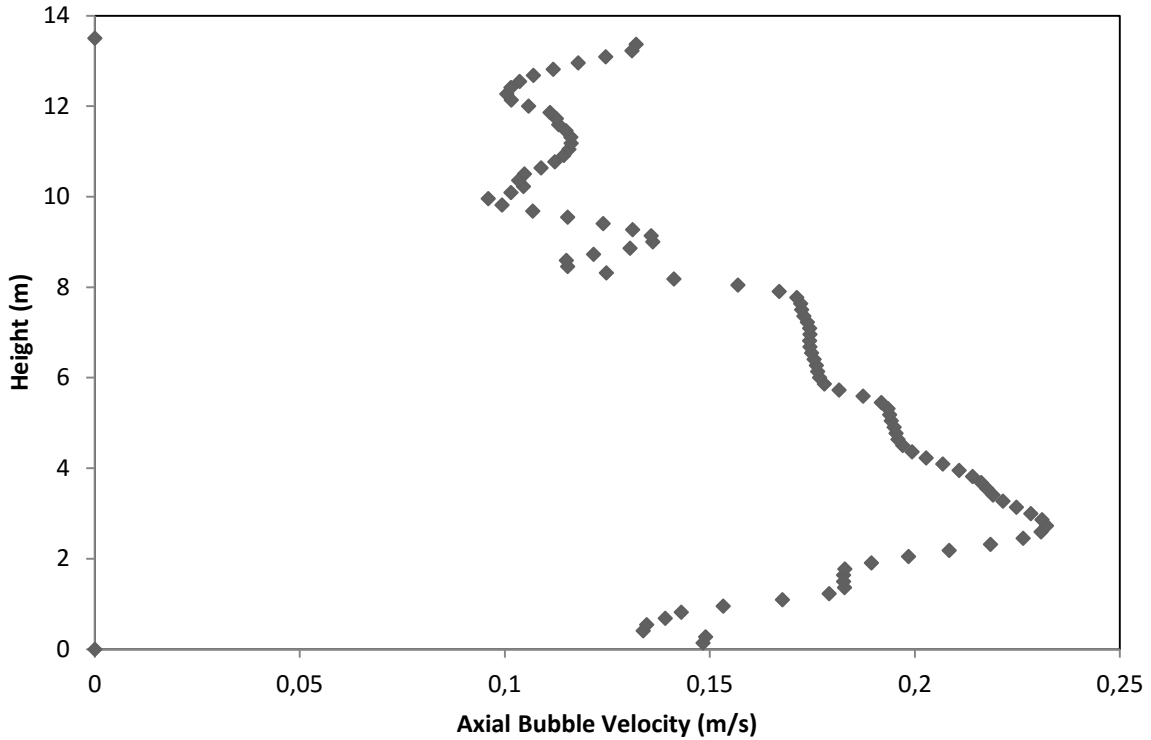
Figure 4.17: Axial bubble velocity versus height along the column axis; J_g = 1.51 cm/s.

4.4.2 Comparison of average and axial gas holdup predicted using different drag coefficients

In this research, simulations were also performed to compare the gas holdup prediction when different drag coefficient formulations were used. In this regard, CFD simulations were carried out with three drag models, the Universal drag, Schiller and Naumann, and the Morsi and Alexander models. The parity plot comparing the average gas holdup prediction for the different drag coefficients is shown in Figure 4.18. It can be seen that there is no significant difference between the results obtained with the three drag coefficients.
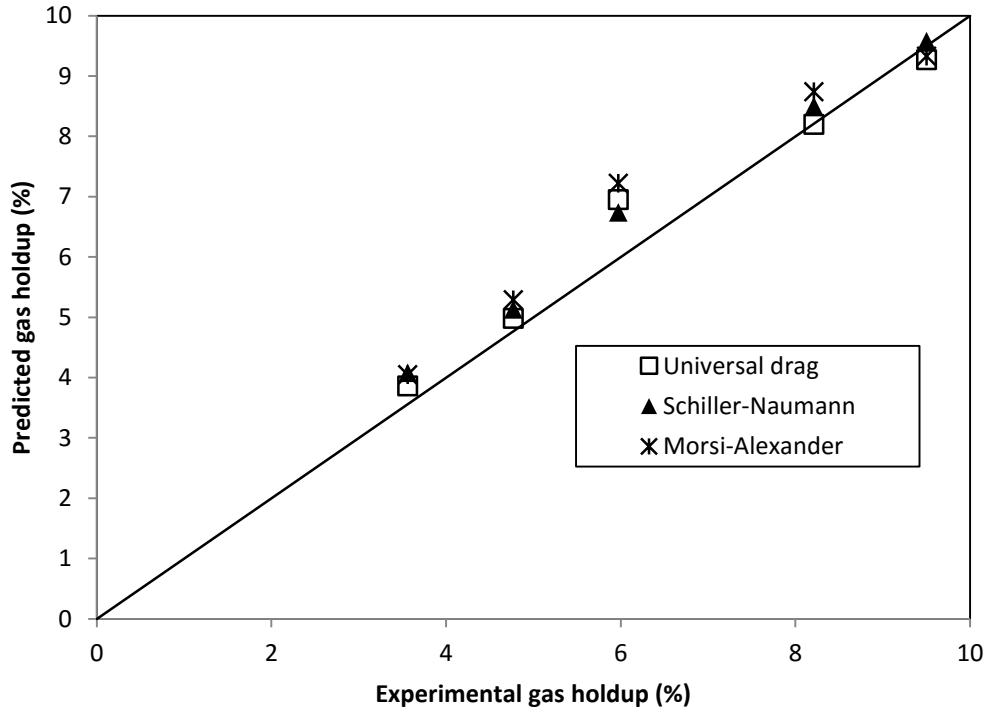
Figure 4.18: Parity plot comparing the average gas holdup prediction for different drag models. The different models are compared against the experimental data from Gomez et al.[18]

The average gas holdup results obtained with the three drag coefficients are further compared against experimental data in Table 4.5 in terms of the mean absolute relative error (MARE) between the CFD predictions and the corresponding experimental measurements calculated as follows:

$$MARE\ (\%) = 100\frac{1}{N}\sum\left|1 - \frac{\varepsilon_{G\,CFD}}{\varepsilon_{G\,Exp}}\right|$$

(4.9)

With mean absolute relative error (MARE) equal to 6.2%, the Universal drag coefficient performs better compared to the Schiller-Naumann (MARE = 7.9%) and Morsi-Alexander (MARE = 10.8%).

Table 4.5: Comparison of average gas holdup predicted using different drag coefficients.

UNIVERSAL DRAG			
Superficial gas velocity (cm/s)	Average gas holdup (%) - Experimental	Gas Holdup (%) - CFD	Relative Error
0.72	3.56	3.86	0.084
0.93	4.77	4.98	0.044
1.22	5.97	6.91	0.157
1.51	8.21	8.20	0.001
1.67	9.50	9.27	0.024
Mean absolute relative error (MARE) = 6.22%			
SCHILLER NAUMANN			
Superficial gas velocity (cm/s)	Average gas holdup (%) - Experimental	Gas Holdup (%) - CFD	Relative Error
0.72	3.56	4.08	0.146
0.93	4.77	5.13	0.075
1.22	5.97	6.74	0.129
1.51	8.21	8.50	0.035
1.67	9.50	9.58	0.008
Mean absolute relative error (MARE) = 7.89%			
MORSI ALEXANDER			
Superficial gas velocity (cm/s)	Average gas holdup (%) - Experimental	Gas Holdup (%) - CFD	Relative Error
0.72	3.56	4.05	0.138
0.93	4.77	5.29	0.109
1.22	5.97	7.22	0.209
1.51	8.21	8.74	0.065
1.67	9.50	9.33	0.018
Mean absolute relative error (MARE) = 10.77%			

The Axial gas holdup predictions using the different drag coefficients are compared with experimental data [18] in Figure 4.19– Figure 4.22. There is again no significant difference between the results obtained with the three drag coefficients. For all the three drag models, the gas hold up prediction was very good for the middle part of the column, good for the top part, and over predicted at low superficial gas velocity (Jg = 0.72 cm/s and 0.93 cm/s) for the bottom part of the column. The over-prediction of the local gas holdup at the bottom part of the column can be attributed to bubble coalescence as already explained above. The mean absolute relative error calculated for the different drag coefficients for the axial gas holdup prediction are presented in Table 4.6 – Table 4.8. Mean absolute relative error above 20% was obtained for the gas holdup prediction in the bottom part of the column with all three drag coefficients. On the other hand, the gas holdup in the middle and top parts of the column was predicted with less than 10% relative error.
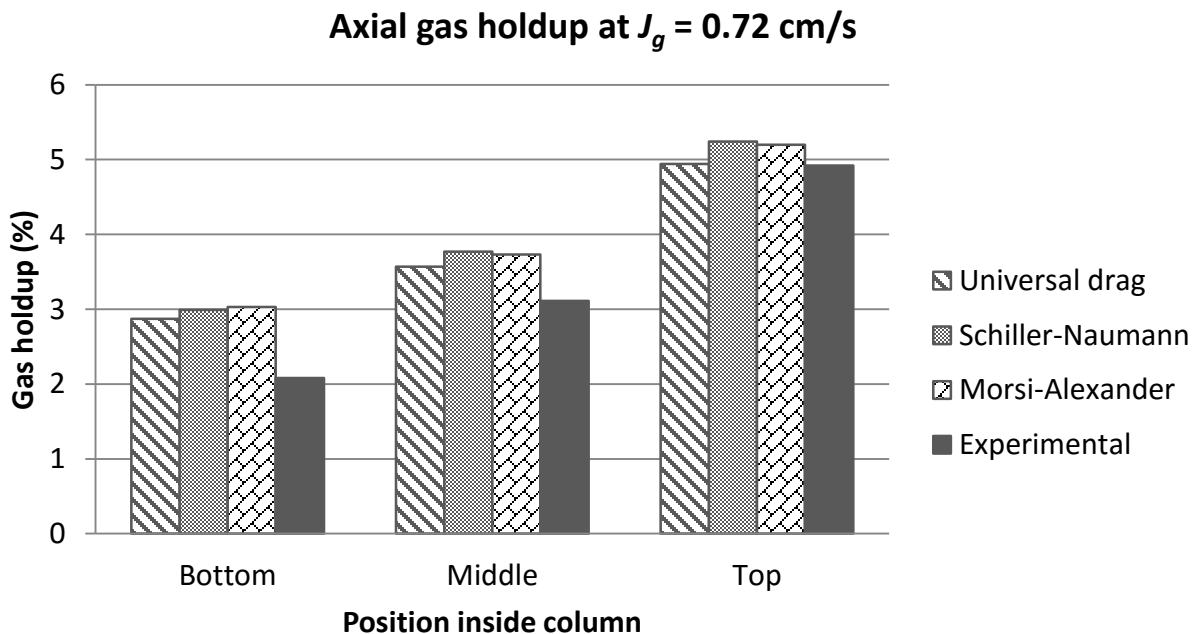
Figure 4.19: Comparison of axial gas holdup prediction for different drag coefficients; superficial gas velocity, J_g = 0.72 cm/s.

Axial gas holdup at J_g = 0.93 cm/s
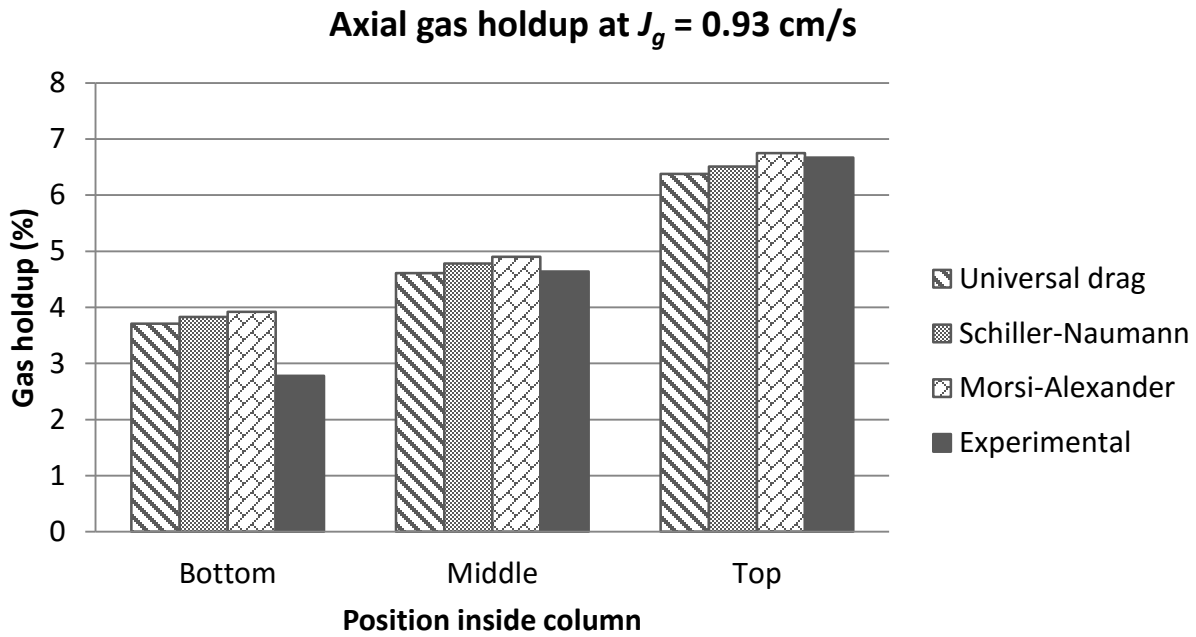
Figure 4.20: Comparison of axial gas holdup prediction for different drag coefficients; superficial gas velocity, J_g = 0.93 cm/s.

Axial gas holdup at J_g = 1.51 cm/s
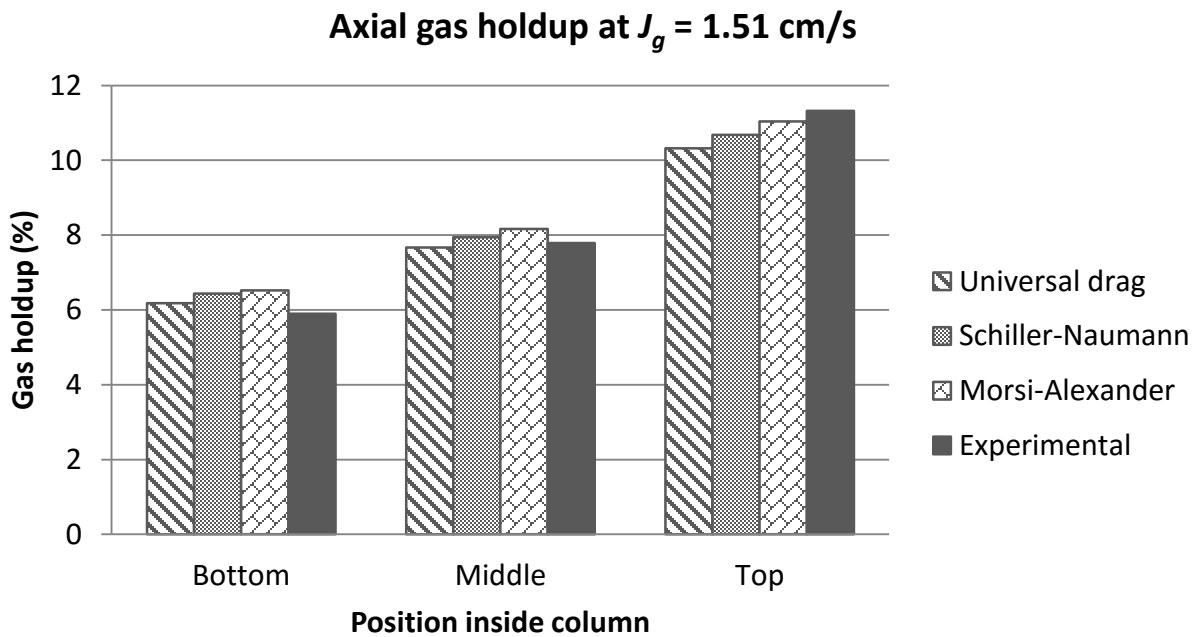
Figure 4.21: Comparison of gas holdup prediction for different drag coefficients; superficial gas velocity, J_g = 1.51 cm/s.

69

Axial gas holdup at J_g = 1.67 cm/s
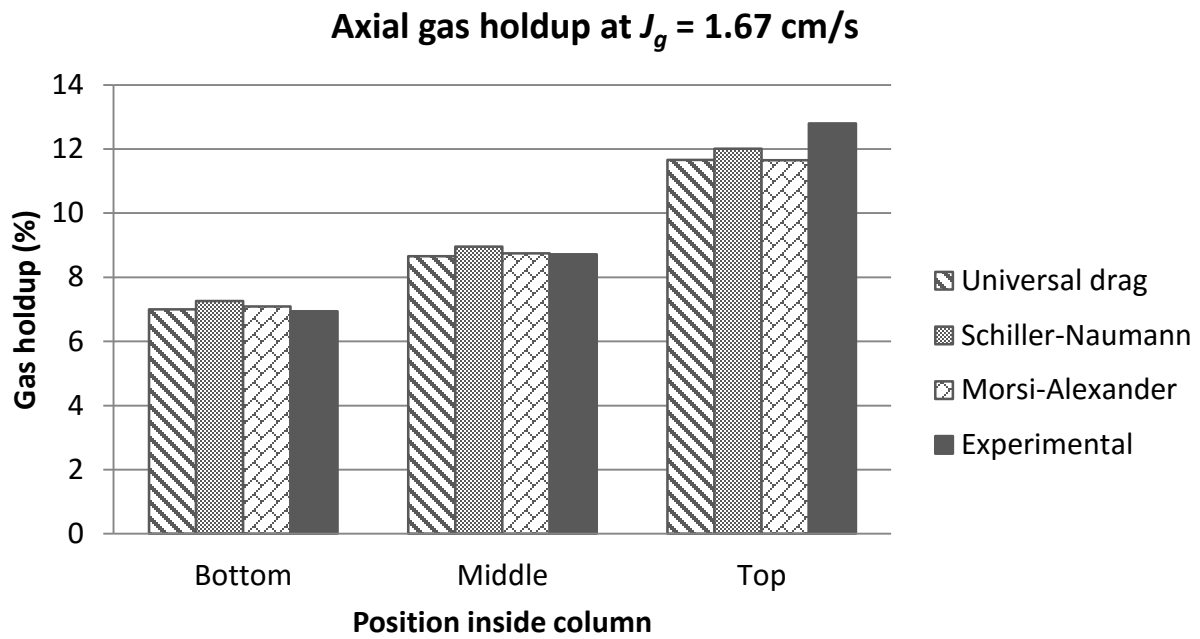
Figure 4.22: Comparison of gas holdup prediction for different drag coefficients; superficial gas velocity, J_g = 1.67 cm/s.

Table 4.6: Comparison of axial gas holdup predicted with different drag coefficients for the bottom section of the column. The drag coefficients are compared against the experimental data of Gomez et al.[18].

UNIVERSAL DRAG			
Superficial gas velocity (cm/s)	Gas holdup bottom section (%)		
	Experimental	CFD	Relative Error
0.72	2.08	2.87	0.380
0.93	2.78	3.71	0.335
1.22	4.17	5.15	0.235
1.51	5.90	6.18	0.047
1.67	6.94	7.00	0.009
Mean absolute relative error (MARE) = 20.11%			
SCHILLER-NAUMANN			
Superficial gas velocity (cm/s)	Gas holdup bottom section (%)		
	Experimental	CFD	Relative Error
0.72	2.08	2.99	0.438
0.93	2.78	3.83	0.378
1.22	4.17	5.08	0.218
1.51	5.90	6.44	0.092
1.67	6.94	7.26	0.046
Mean absolute relative error (MARE) = 23.42%			
MORSI-ALEXANDER			
Superficial gas velocity (cm/s)	Gas holdup bottom section (%)		
	Experimental	CFD	Relative Error
0.72	2.08	3.03	0.457
0.93	2.78	3.92	0.410
1.22	4.17	5.37	0.288
1.51	5.90	6.52	0.105
1.67	6.94	7.09	0.022
Mean absolute relative error (MARE) = 25.63%			

Table 4.7: Comparison of axial gas holdup predicted with different drag coefficients for the middle section of the column. The drag coefficients are compared against the experimental data of Gomez et al.[18].

UNIVERSAL DRAG			
Superficial gas velocity (cm/s)	Gas holdup middle section (%)		
	Experimental	CFD	Relative Error
0.72	3.11	3.57	0.148
0.93	4.64	4.61	0.006
1.22	5.84	6.44	0.103
1.51	7.79	7.67	0.015
1.67	8.72	8.66	0.007
Mean absolute relative error (MARE) = 5.59%			
SCHILLER-NAUMANN			
Superficial gas velocity (cm/s)	Gas holdup middle section (%)		
	Experimental	CFD	Relative Error
0.72	3.11	3.77	0.212
0.93	4.64	4.78	0.030
1.22	5.84	6.29	0.077
1.51	7.79	7.94	0.019
1.67	8.72	8.96	0.028
Mean absolute relative error (MARE) = 7.32%			
MORSI-ALEXANDER			
Superficial gas velocity (cm/s)	Gas holdup middle section (%)		
	Experimental	CFD	Relative Error
0.72	3.11	3.73	0.199
0.93	4.64	4.90	0.056
1.22	5.84	6.70	0.147
1.51	7.79	8.16	0.047
1.67	8.72	8.75	0.003
Mean absolute relative error (MARE) = 9.072%			

Table 4.8: Comparison of axial gas holdup predicted with different drag coefficients for the top section of the column. The drag coefficients are compared against the experimental data of Gomez et al.[18].

UNIVERSAL DRAG			
Superficial gas velocity (cm/s)	Gas holdup top section (%)		
	Experimental	CFD	Relative Error
0.72	4.92	4.94	0.004
0.93	6.67	6.38	0.043
1.22	8.22	8.87	0.079
1.51	11.32	10.32	0.088
1.67	12.8	11.66	0.089
Mean Absolute Relative Error (MARE) = 6.08%			
SCHILLER-NAUMANN			
Superficial gas velocity (cm/s)	Gas holdup top section (%)		
	Experimental	CFD	Relative Error
0.72	4.92	5.24	0.065
0.93	6.67	6.51	0.024
1.22	8.22	8.49	0.033
1.51	11.32	10.68	0.057
1.67	12.8	12.01	0.062
Mean Absolute Relative Error (MARE) = 4.80%			
MORSI-ALEXANDER			
Superficial gas velocity (cm/s)	Gas holdup top section (%)		
	Experimental	CFD	Relative Error
0.72	4.92	5.2	0.057
0.93	6.67	6.75	0.012
1.22	8.22	9.2	0.119
1.51	11.32	11.04	0.025
1.67	12.8	11.65	0.090
Mean Absolute Relative Error (MARE) = 6.05%			

4.5 Conclusions

CFD modelling was applied to study the gas holdup and its variation along the collection zone of a pilot flotation column. Both the predicted average gas holdup and the axial (local) gas holdup were in good agreement with the experimental data available in the literature. The generally known gas distribution profile, with the gas holdup increasing upward in the column and having maximum values in the column centre was also predicted by the CFD simulations.

Three drag models, the Universal drag, Schiller-Naumann, and Morsi-Alexander drag coefficients were compared in this study in order to determine the suitable drag model for average and axial gas holdup prediction in the column. The three drag coefficients all produced good prediction of both the average and local gas holdup. Therefore, any of these three drag coefficients can be used to model flotation column hydrodynamics.

An axial velocity profile was also observed in which the bubble velocity magnitude decreased with height along the column. The reason for this could be the increase in drag force resulting from the axial increase in gas holdup along the column height. However, the decrease in axial bubble velocity along the column height can result in a further increase in the axial gas holdup variations compared to the effect of the hydrostatic pressure only. The axial variation in gas holdup could therefore be explained as having its origins in two inter-related processes – the hydrostatic expansion of air bubbles and the development of a bubble velocity profile in which the axial velocity of bubbles decreases with height along the column.

Chapter 5   CFD Simulation of the mixing characteristics of industrial flotation columns

5.1   Introduction

In this chapter, the mixing characteristics of the collection zone of industrial flotation columns are investigated using Computational Fluid Dynamics (CFD). Flotation columns are known for their improved metallurgical performance compared to conventional flotation cells. However, increased mixing in the column can adversely affect its grade/recovery performance.

It has been observed that mineral recovery decreases as the mixing conditions increase from plug flow towards perfectly mixed flow in the column [2, 56]. A high degree of mixing will therefore have detrimental effects on the overall performance of a flotation column. As a result, the design and optimization of flotation columns require detailed knowledge of the effects of various geometrical and operational parameters on the mixing characteristics of the column.

The mixing characteristics of flotation columns have been studied by several researchers [58, 64, 65, 103, 104]. However, there are still uncertainties particularly with regard to solids mixing characteristics in the column. The earlier studies by Dobby and Finch [58] and Yianatos and Bergh [65] suggested that the solids and liquid axial dispersion coefficients were equal. On the other hand, several authors have questioned the equivalence of the solids and liquid dispersion citing various reasons [61, 105, 106]. Some researchers have also investigated the effect of solids on the liquid dispersion in the column [40, 59]. It has been reported that the liquid dispersion decreased as the percentage of solids in the feed increased, possibly due to viscous effects. However, the effect of particle size on the liquid dispersion has not yet been studied.

The studies described above were entirely based on experimental methods which did not provide detailed information of the solids and liquid flow patterns inside the flotation column. On the other hand, Computational Fluid Dynamics (CFD) is an alternative modelling tool which is based on the flow physics of the process. CFD methodology can therefore be used in the study of the mixing characteristics of flotation columns, with the additional advantage of basing the interpretation of the results on the flow patterns derived from numerical simulations. Despite the fact that CFD can potentially be useful in the design and

75

optimization of column flotation, there seems to be a limited amount of literature on the subject. In addition, the few column flotation CFD models in the literature in which mixing is investigated have simulated two phase (gas-liquid) flows only while solids have not been included in the column [11, 15].

Deng et al. [11] applied numerical simulations to study the flows in flotation columns. They predicted a liquid circulation pattern in which the axial liquid velocity was upward in the centre and downward near the walls of the column. The mixing in the flotation column was further attributed to the liquid circulation pattern established in the column. However, the actual mixing was not simulated in terms of residence time distributions (RTDs).

Subsequent studies were conducted by Xia et al. [15] who used a two-dimensional CFD model to simulate the alleviation of liquid back-mixing by baffles and packings in a flotation column. Their study revealed that the liquid back-mixing in an open bubble/flotation column could be alleviated using baffles and packings. However, the liquid RTD simulations were not conducted in order to quantify the actual mixing parameters in the open column compared to the baffled column and the column with packings.

The aim of the study presented in this chapter was, therefore, to investigate the mixing characteristics of industrial flotation columns using Computational Fluid Dynamics (CFD). In this regard, CFD models were developed for the 0.45 m square column and the 0.91 m diameter cylindrical column from the work of Dobby and Finch [58] and Yianatos and Bergh [65], respectively. These authors' data was therefore used to validate the present modelling approach. Specifically, the work presented in this chapter involves numerical simulations of residence time distributions (RTDs) of both the liquid and solid phases in industrial columns. The simulated RTDs are then used to determine the mixing parameters, i.e., the mean residence time and the vessel dispersion number. Both the mean residence time and the vessel dispersion number are useful parameters in the design and scale-up equations for column flotation.

In addition, the simulated flow patterns of the solid and liquid phases are compared in order to understand the relationship between the solid and liquid dispersion characteristics. The effects of particle size and bubble size on liquid back-mixing in the column are also investigated.

5.2 Theory

The one-dimensional (axial) plug flow dispersion model is applicable to describe the axial mixing process in the collection zone of the flotation column [2]. In this case, the degree of mixing is quantified by the axial dispersion coefficient D (units of length^2/time) or the dimensionless vessel dispersion (N_d).

Two extreme cases of mixing exist, namely:

- Plug flow (negligible dispersion), $N_d \rightarrow 0$
- Perfectly mixed reactor (large dispersion), $N_d \rightarrow \infty$

The vessel dispersion number is given by:

$$N_d = \frac{D}{uH} \tag{5.1}$$

where u is either the liquid interstitial velocity or the particle velocity and H is the height of the collection zone.

The axial dispersion coefficient (D) or the vessel dispersion number (N_d) can be calculated from Residence Time Distribution (RTD) data using two parameters: the mean residence time (τ) and the variance or measure of the spread of the RTD curve (σ^2). These measures are directly related by theory to D and/or N_d. In this study, the mean residence time was calculated from the first moment about the origin according to the following equation [107]:

$$\tau = \frac{\int_0^\infty t\,C\,dt}{\int_0^\infty C\,dt} = \frac{\sum t C \Delta t}{\sum C \Delta t} \tag{5.2}$$

On the other hand, the variance is given by the second moment about the mean as follows:

$$\sigma^2 = \frac{\int_0^\infty (t-\tau)^2\,C\,dt}{\int_0^\infty C\,dt} = \frac{\int_0^\infty t^2\,C\,dt}{\int_0^\infty C\,dt} - \tau^2 \tag{5.3}$$

For a set of discrete data points, the variance is expressed as:

$$\sigma^2 \cong \frac{\sum (t-\tau)^2 C \Delta t}{\sum C \Delta t} = \frac{\sum t^2 C \Delta t}{\sum C \Delta t} - \tau^2 \tag{5.4}$$

77

The variance measures the spread of the distribution about the mean and has units of (time)^2. It is mainly useful for matching experimental RTD curves to one of a family of theoretical curves. Once the mean residence time and the variance have been determined, the vessel dispersion number (*D/uH*) can be calculated from the following equation for closed vessel boundary conditions [107]:

$$\sigma_\theta{}^2 = \frac{\sigma^2}{\tau^2} = 2\frac{D}{uH} - 2(\frac{D}{uH})^2(1 - e^{-uH/D}) \qquad (5.5)$$

5.3 CFD Methodology

5.3.1 Model geometry, mesh, and boundary conditions

Air bubbles were introduced into the column by means of mass and momentum source terms at the bottom of the column. Since the sparging systems that are used in industrial flotation columns are designed to ensure uniform distribution of air bubbles over the entire column cross section [26], the air bubbles were introduced over the entire column cross section in this study without including the physical spargers in the model geometry. Uniform air distribution has also been verified in pilot scale flotation columns by means of radial gas holdup measurements [27, 28].The use of the entire column cross section for bubble introduction into the column is therefore a legitimate albeit simplified representation of the sparging system in the simulated industrial columns. Correspondingly, the information available in the literature for the flotation columns being simulated in the present study was mostly given in terms of superficial velocities calculated over the entire column cross-section. The mass and momentum source terms were calculated from the respective superficial gas velocities as described in Chapter 3. Corresponding sink terms were applied at the top of the column to simulate the exit of the air bubbles from the collection zone.

Since only the collection zone is modelled in this work, the resulting model geometry is simply a vessel of height equal to the collection zone height and radial dimensions similar to the respective flotation column. For the liquid phase the top of the column was modelled using velocity inlet boundary conditions where inlet velocity was set equal to the superficial liquid velocity. Since the computational domain being considered is the collection zone of the column, the superficial liquid velocity must include the feed rate plus the bias water resulting from wash water addition. The superficial liquid velocity is therefore equal to the superficial tailing rate. The bottom part of the column was also modelled as a velocity inlet boundary where exit velocity was set equal to the liquid superficial velocity but with a negative sign.

For the column wall, no slip boundary conditions were applied for both the liquid (primary phase) and the air bubbles as well as solids (secondary phases).

The mesh used in the present study was generated over the model geometry using the meshing application of ANSYS Workbench. The mesh was in each case generated using the Sweep method which creates a mesh comprising mainly hexahedral elements. The computational mesh for the square and the cylindrical columns are shown in Figure 5.1 and Figure 5.2, respectively. Grid independency studies were conducted in which the numerical solution was tested at several different mesh sizes until changes in applicable flow regimes became insignificant.
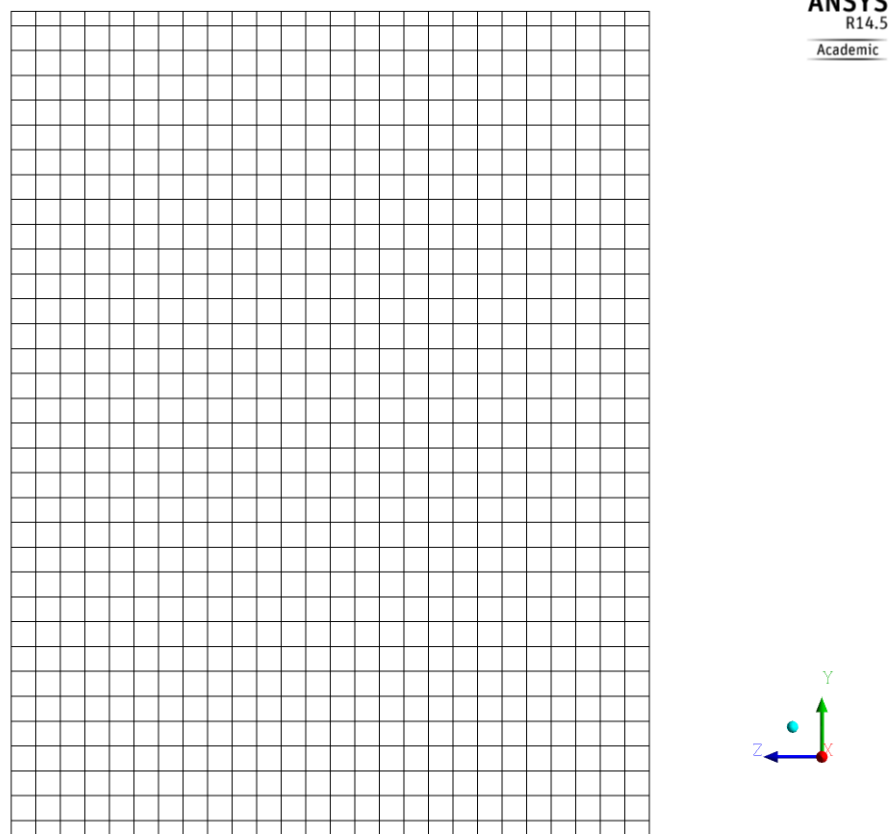
Figure 5.1: Computational mesh for the 0.45 m square column (side view).

Top view   Side view
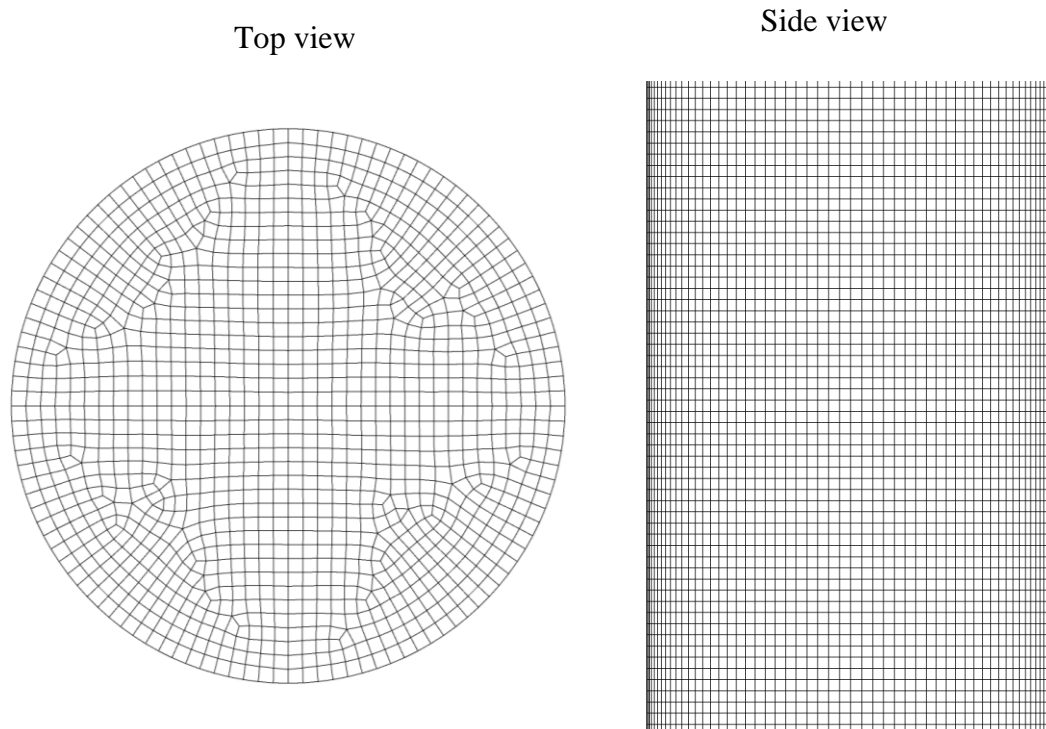
Figure 5.2: Computational mesh for the 0.91 m diameter cylindrical column.

5.3.1.1   Grid independence study (0.45 m square column)

Five mesh sizes with attributes outlined in Table 5.1 were considered for the grid independency study. The simulated mean axial bubble and water velocity profiles for these mesh sizes are given in Figure 5.3 and Figure 5.4. It can be seen that mesh 1, mesh 2, and mesh 3 all gave unrealistic velocity profiles. On the other hand, mesh 4 and mesh 5 gave axial liquid velocity profiles similar to those reported in the literature for bubble columns [48, 50, 108]. However, grid independent solutions were not obtained due to increasingly unrealistic computational time of the simulations for mesh sizes smaller than mesh 5. Mesh 4 was therefore used in all the subsequent simulations as a reasonable trade-off between the desired accuracy and the computational time of the simulations.

Table 5.1: Mesh sizes considered for the grid independency study (0.45 m square column).

Identification	Element size (cm)	Number of cells	Number of nodes	Minimum orthogonal quality	Gas holdup (%)
Mesh 1	5	19, 200	23, 353	1	13.07
Mesh 2	3.5	53, 508	61, 650	1	13.01
Mesh 3	2.5	123, 768	138, 263	1	12.56
Mesh 4	1.75	367, 744	397, 305	1	13.43
Mesh 5	1.25	986, 256	1, 043, 178	1	13.24
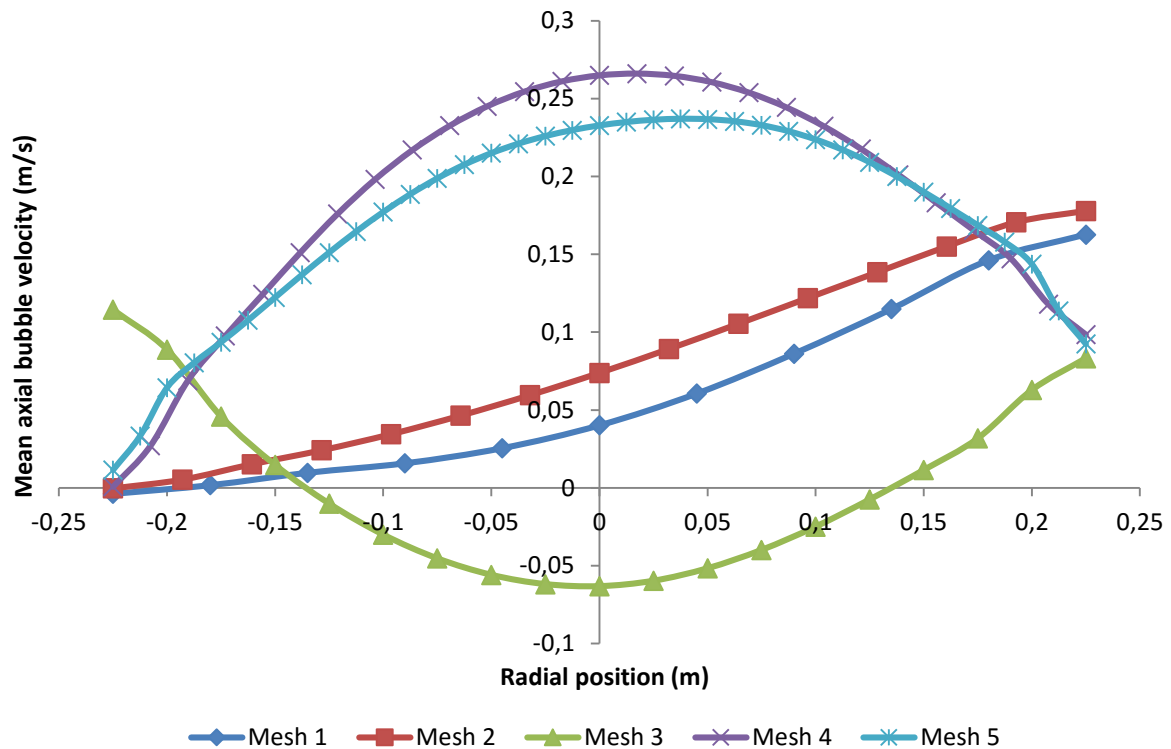
Figure 5.3: Simulated mean axial bubble velocities for different mesh sizes (0.45 m square column).

81
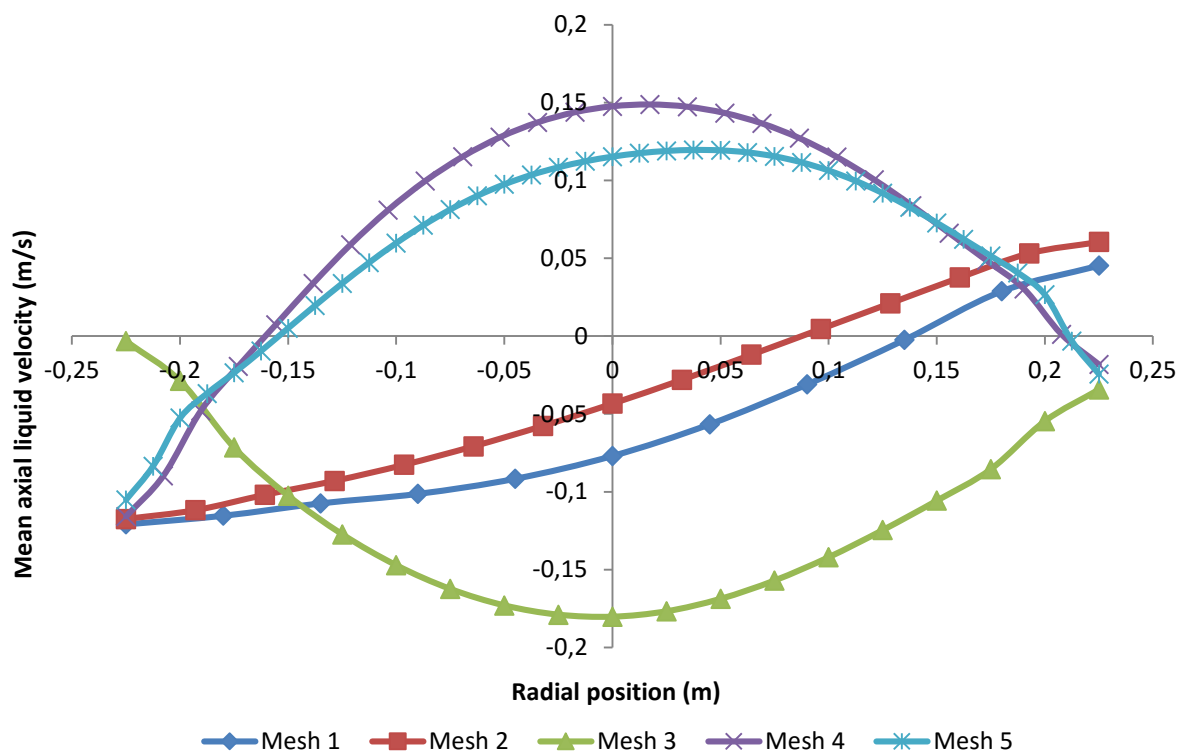
Figure 5.4: Simulated mean axial liquid (water) velocities for different mesh sizes (0.45 m square column).

5.3.1.2 Grid independency study (0.91 m diameter cylindrical column)

For the cylindrical column, four mesh sizes were examined for grid independency. The mesh sizes are outlined in Table 5.2. The predicted mean axial bubble and liquid velocity profiles for the different mesh sizes are shown in Figure 5.5 and Figure 5.6, respectively. Comparing the results of mesh 3 and 4, mesh 3 with 502,098 grid cells was selected as a good compromise with respect to computational time.

Table 5.2: Mesh sizes considred for the grid independency study (0.91 m diameter column).

Identification	Element size (cm)	Number of cells	Number of nodes	Minimum orthogonal quality	Gas holdup (%)
Mesh 1	5	70, 902	77, 140	0.850	14.63
Mesh 2	3.75	151, 985	163, 620	0.838	14.87
Mesh 3	2.5	502, 098	525, 512	0.829	14.83
Mesh 4	1.875	1, 152, 925	1, 195, 816	0.794	14.80

82
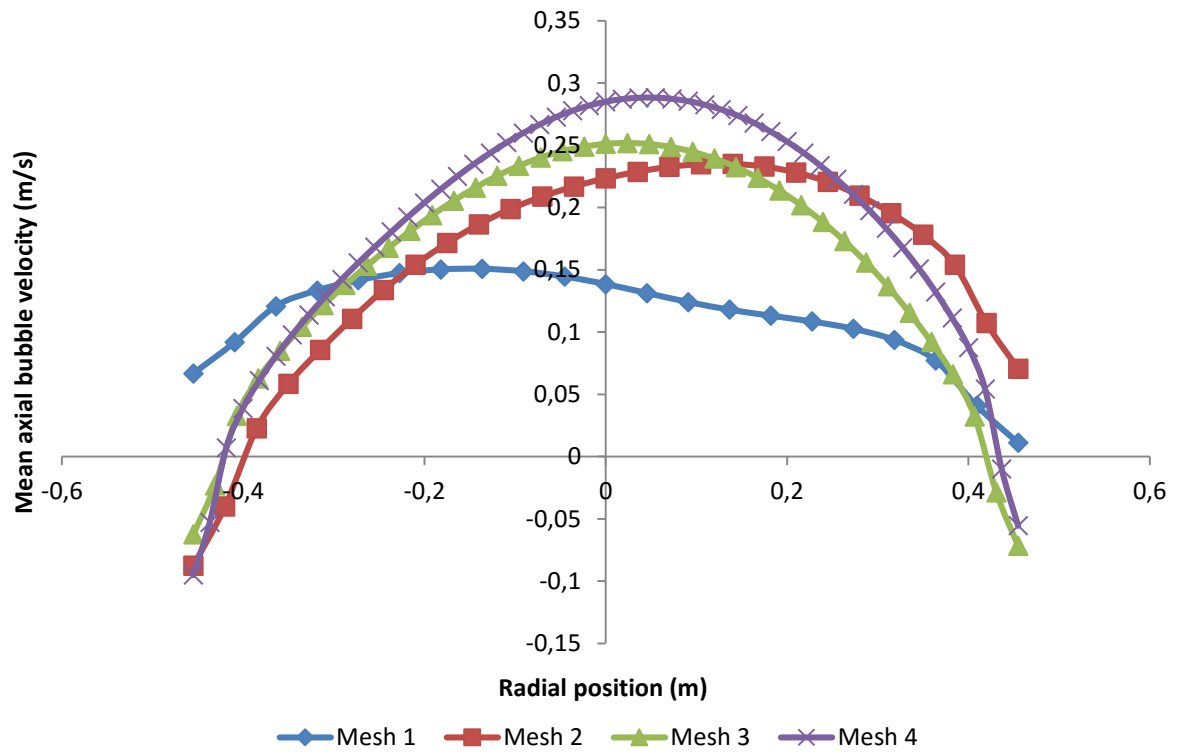
Figure 5.5: Simulated mean axial bubble velocity profiles for the different mesh sizes (0.91 m diameter column).
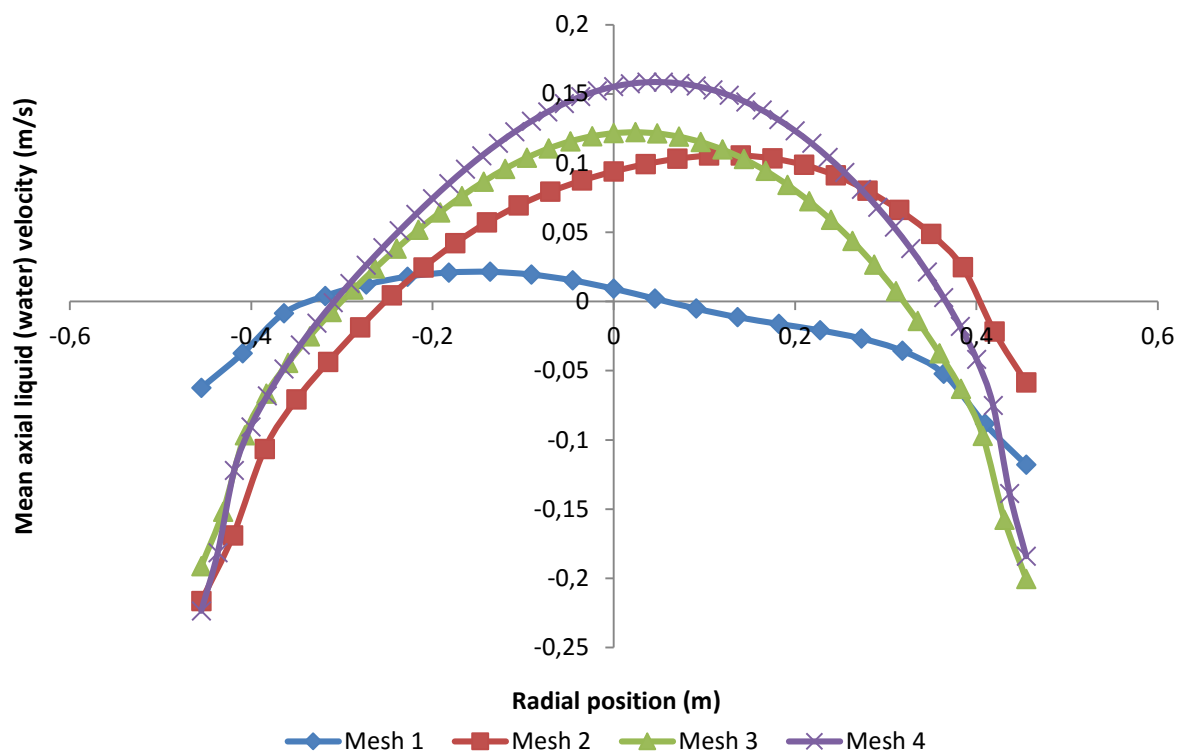
Figure 5.6: Simulated mean axial liquid velocity profiles for the different mesh sizes (0.91 m diameter column).

5.3.2   Multiphase model

In this research, the multiphase flow in the flotation columns was modeled using the Eulerian-Eulerian (E-E) approach which has been recommended for industrial scale bubble columns due to its computational efficiency [80, 109]. In the Eulerian-Eulerian approach, both the continuous (primary) phase and the dispersed (secondary) phase are modelled in an Eulerian frame of reference as interpenetrating continua. Conservation equations for mass and momentum are therefore solved for each phase separately. Interaction between the phases is then accounted for by means of momentum exchange terms incorporated in their respective momentum equations.

In the present study, the three-phase flow in the industrial flotation columns was modelled considering water as the continuous phase (or primary phase) while air bubbles and solid particles were treated as dispersed phases (or secondary phases). The volume averaged mass and momentum conservation equations for the gas and liquid phase have been given in Chapter 3, equations (3.3) and (3.4). The continuity and momentum equations for the solids (particles) are presented respectively as follows:

$$\frac{\partial}{\partial t}(\varepsilon_s \rho_s) + \nabla.(\varepsilon_s \rho_s \overrightarrow{u_s}) = 0 \tag{5.6}$$

$$\frac{\partial}{\partial t}(\varepsilon_s \rho_s \overrightarrow{u_s}) + \nabla.(\varepsilon_s \rho_s \overrightarrow{u_s} \otimes \overrightarrow{u_s}) = -\varepsilon_s \nabla p - \nabla P_s + \nabla.\varepsilon_s \overline{\overline{\tau_s}} + \varepsilon_s \rho_s \overrightarrow{g} + M_{s,l} \tag{5.7}$$

where s is the index for solid phase and P_s is the solids pressure, ε_s is the volume fraction, ρ_s is the phase density, and $\overrightarrow{u_s}$ is the velocity of the solid phase. $M_{s,l}$ is the momentum exchange between the solids and liquid phases and $\varepsilon \rho g$ is the gravity force, while $\overline{\overline{\tau_s}}$ is the solids phase stress tensor given by:

$$\overline{\overline{\tau_s}} = \varepsilon_s \mu_s \left(\nabla \overrightarrow{u_s} + \nabla \overrightarrow{u_s}^T \right) + \varepsilon_s \left(\lambda_s - \frac{2}{3}\mu_s \right) \nabla.\overrightarrow{u_s} \overline{\overline{I}} \tag{5.8}$$

In terms of the momentum exchange forces between the phases, only the drag force between the continuous phase and the dispersed phases was considered in this study. The momentum exchange between the two dispersed phases was not included in the model.

5.3.2.1 Gas-liquid drag force

The drag force per unit volume for bubbles in a swarm is generally obtained from the following equation:

$$\overrightarrow{F_D}(g,l) = \frac{3\varepsilon_g \varepsilon_l}{4}\left(\frac{\rho_l}{d_B} \right) C_D(g,l)\left| \overrightarrow{u_g} - \overrightarrow{u_l} \right|\left(\overrightarrow{u_g} - \overrightarrow{u_l} \right) \tag{5.9}$$

where C_D (g, l) is the drag coefficient between the liquid phase and the air bubbles, d_B is the bubble diameter, and $\overrightarrow{u_g} - \overrightarrow{u_l}$ is the slip velocity. There are a number of empirical correlations that can be used to calculate the drag coefficient, C_D (g, l). The drag coefficient is normally presented in these correlations as a function of the bubble Reynolds number (Re) defined as:

$$Re = \frac{\rho_l \left| \overrightarrow{u_g} - \overrightarrow{u_l} \right| d_B}{\mu_l} \tag{5.10}$$

In this study, the drag coefficient was calculated using the Universal Drag Laws [94]. In this case, the universal drag coefficient is defined in different ways depending on whether the prevailing regime is in the viscous regime category, the distorted bubble regime, or the strongly deformed caped bubbles regime. At the moderate superficial gas velocities simulated

in the present study, the viscous regime conditions apply and the drag coefficient is calculated from the following equation:

$$C_D(g,l)_{vis} = \frac{24}{Re}(1 + 0.1Re^{0.75}) \tag{5.11}$$

5.3.2.2 *Liquid-solid drag force*

The drag force between the liquid and the solid particles was calculated using the Wen and Yu model [110]. The drag force per unit volume is given by:

$$\overrightarrow{F_D}(s,l) = \frac{3}{4}C_D(s,l)\frac{\varepsilon_s\varepsilon_l\rho_l|\overrightarrow{\boldsymbol{u}_s} - \overrightarrow{\boldsymbol{u}_l}|}{d_s}\varepsilon_l^{-2.65}(\overrightarrow{\boldsymbol{u}_l} - \overrightarrow{\boldsymbol{u}_s}) \tag{5.12}$$

The drag coefficient is calculated as:

$$C_D(s,l) = \frac{24}{\varepsilon_l Re_s}[1 + 0.15(\varepsilon_l Re_s)^{0.687}] \tag{5.13}$$

The Wen and Yu model is suitable for dilute systems similar to the conditions simulated in the present study.

5.3.3 Turbulence model

Turbulence in the continuous phase (water) was modelled using the realizable k-ϵ turbulence model which is a RANS (Reynolds-Averaged Navier-Stokes) based model. In the RANS turbulence modelling, the instantaneous Navier-Stokes equations are time averaged to produce the Reynolds-Averaged Navier-Stokes (RANS) equations which are solved to obtain a time averaged flow field. The averaging procedure introduces additional unknowns; the Reynolds stresses which represent the effects of turbulent fluctuations on the mean flow. RANS models therefore calculate the mean flow while modelling the effect of turbulent fluctuations on the mean flow.

The k-ϵ model is an Eddy Viscosity turbulence model. The Reynolds stresses are therefore related to the velocity gradients through the turbulent viscosity as presented in the following equation:

$$-\rho\overline{u_i'u_j'} = \mu_t\left(\frac{\partial\boldsymbol{u}_i}{\partial x_j} + \frac{\partial\boldsymbol{u}_j}{\partial x_i}\right) - \frac{2}{3}\left(\rho k + \mu_t\frac{\partial\boldsymbol{u}_k}{\partial x_i}\right)\delta_{ij} \tag{5.14}$$

where μ_t is the turbulent or eddy viscosity, k is the turbulent kinetic energy and δ_{ij} is the Kronecker delta. The Kronecker delta is important in order to make the eddy viscosity

concept applicable to normal stresses where i = j. On the other hand, the turbulent viscosity is calculated from the turbulent kinetic energy (k) and the turbulent dissipation rate according to the following equation:

$$\mu_t = \rho C_\mu \frac{k^2}{\epsilon} \tag{5.15}$$

The k-ϵ model is therefore a two equation turbulence model since two additional transport equations must be solved for the turbulent kinetic energy (k) and dissipation rates (ϵ).

5.3.4 Residence Time Distribution (RTD) Simulation

There are several methods for predicting residence time distribution using CFD. One way is to represent the tracer fluid by a large number of discrete particles and then applying Lagrangian particle tracking analysis with the Discrete Phase Model (DPM) available in ANYSIS FLUENT [111, 112]. The particle residence time is monitored at the outlet and plotted in a histogram which represents the residence time distribution. This method was not used in the present study because it requires a larger number of particles with subsequent increase in the computational cost of the simulations.

In the second method, the tracer fluid is considered as a continuum by solving an additional transport equation for the tracer species. The concentration of the tracer is then monitored at the outlet to give the RTD. The method applied to simulate the liquid RTD in the present study is similar to this one.

5.3.4.1 *Liquid RTD*

Liquid RTD was modelled by solving conservation equations for chemical tracer species using the Species Model in ANSYS FLUENT. In multiphase flows, the species conservation equation is solved for each phase q to predict the local mass fraction of each species Y_i^q by means of a convection-diffusion equation for the ith species. For an inert tracer species, the species conservation equation for a multiphase mixture can be represented as follows:

$$\frac{\partial}{\partial t}(\rho^q \varepsilon^q Y_i^q) + \nabla.(\rho^q \varepsilon^q \overrightarrow{\boldsymbol{u}}^q Y_i^q) = -\nabla.\varepsilon^q \overrightarrow{J_i}^q \tag{5.16}$$

where $\overrightarrow{J_i}$ is the diffusion flux of species i which is obtained from the following equation:

$$\overrightarrow{J_i} = -\left(\rho D_{i,m} + \frac{\mu_t}{Sc_t}\right)\nabla Y_i \tag{5.17}$$

87

where $D_{i,m}$ is the mass diffusion coefficient for species i, Sc_t is the turbulent Schmidt number ($\frac{\mu_t}{\rho D_t}$ where μ_t is the turbulent viscosity) and D_t is the turbulent diffusivity. The flux $\vec{J_i}$ therefore consists of two parts, the molecular diffusion and the turbulent diffusion.

In the present study, the simulations were conducted in two stages. First, the velocity flow field was calculated using the First Order Upwind scheme for momentum, volume fraction, and turbulence kinetic energy and dissipation rate discretization. The First Order Upwind scheme was preferred in order to avoid divergence during the computations.

In the second stage, tracer simulations were performed on the 'frozen' velocity field obtained in the first step. In other words, once the converged solution of the flow equations was obtained, the flow field was 'frozen' by disabling the flow equations and the turbulence and volume fraction equations in the solver. A tracer species was then defined with properties similar to those of the carrier fluid, in this case water. Next, unsteady tracer simulations were carried out solving only the species conservation equation using the Second Order Implicit formulation for time discretization.

5.3.4.1.1 Tracer injection and monitoring

The tracer mass fraction at the column inlet was set to 1 for time durations similar to the tracer injection time in the respective experimental columns. In this case, the total injection time was about 30 seconds for the square column [58] and 1 second for the cylindrical column [65]. After that, the mass fraction of the tracer was again set to 0 and the simulation continued. The mass fraction of the tracer was subsequently recorded at the outlet every 10s and used to obtain the Residence Time Distribution (RTD) curves from which the mean residence time (τ) and the vessel dispersion number (N_d) were calculated.

The method used for liquid RTD simulation is summarized as follows:

- Calculate velocity field – Calculated using the First Order Upwind momentum discretization scheme
- Introduce Tracer Species – A tracer species is introduced having properties of water, the carrier fluid
- Perform unsteady tracer simulation – Species conservation equation is solved on frozen flow field while monitoring exit mass fraction

5.3.4.2   *Particle (Solids) RTD*

Particle RTD was modelled using a transport equation that computes the age of particles in the column. This method is based on the transport equation for the local residence time of a fluid as derived by Ghirelli and Leckner [35]. The equation was introduced into the CFD model of the flotation column as a User Defined Scalar (UDS) equation. In this case, particle age (or residence time) is considered as a scalar property that is being transported by the particles. The resulting spatial distribution of particle age in the column can be used to describe the mixing characteristics of the solid phase. The transport equation for the age of particles is presented as follows:

$$\frac{\partial}{\partial t}(\rho_s \varepsilon_s a_s) + \frac{\partial}{\partial x_i}(\rho_s \boldsymbol{u}_i \varepsilon_s a_s) = \rho_s \varepsilon_s \qquad (5.18)$$

The product on the right hand side of equation (5.18) was included as a source term introduced by means of a User Defined Function (UDF). The UDF is outlined in Appendix 2. The boundary conditions for the particle age were set up as follows:

- At the inlet the particle age (or residence time) is set to zero
- At the walls, a zero flux condition was specified for the particle age
- At the outlet, the particle age was extrapolated from the last domain cell

The mean residence time of the particles was obtained as the mass weighted or area weighted average age of the particles at the outlet. An overview of the method is presented in the following outline:

- Calculate velocity field – First Order Upwind scheme is used for momentum discretization
- Introduce UDS for particle age – Particle age is considered as a scalar property transported by the particles
- Solve UDS equation – Scalar conservation equation for spatial age distribution is solved on 'frozen' flow field
- Determine Residence time – Mass Weighted Average age at outlet is the mean residence time

5.4   Results and discussion

Three phase CFD simulations were conducted to model the 0.45 m square column and the 0.91 m diameter cylindrical column that were used in the work of Dobby and Finch [58] and Yianatos and Bergh [65], respectively. The operating conditions of the two columns are presented in theTable 5.3.

A bubble size of 1 mm was used in the simulations for the 0.45 m column since this is the typical bubble size reported for this column in literature [1]. On the other hand, the 0.91 m diameter column was simulated with different average bubble sizes including 0.8, 1, 1.5 and 2 mm in order to determine the bubble size that would give the correct gas holdup (18%) for the column (refer to Table 5.3). The correct gas holdup was subsequently obtained with a bubble size of 0.8 mm. The simulated RTDs obtained using the different bubble sizes were also compared in order to investigate the effect of bubble size on axial mixing in the column.

The CFD simulations in this study were conducted using average particle sizes comparable with the range of particle sizes studied in the corresponding experimental work. Separate simulations were performed for each particle size in order to minimize the computational cost of the simulations. The results obtained from the CFD simulations are presented separately for the two columns.

Table 5.3: Operating conditions of the industrial columns being simulated in the present study [58, 65].

	Square column (Dobby and Finch)	Cylindrical column (Yianatos and Bergh)
Superficial gas velocity (cm/s)	1.4	1.8
Superficial liquid velocity (cm/s)	1.2	0.92
Gas holdup (%)	5.5	18
Feed wt% solids	3	16.2
Solids volume fraction	0.006	0.0604
Solids density (g/cm^3)	5.19	3
Collection zone height (m)	9.5	10

5.4.1   Square column

In their experimental work, Dobby and Finch [58] measured the liquid (water) RTD together with the solids RTD for a range of solid particle sizes averaging 44, 63, 88, and 125 µm. In the present research, CFD modelling was applied to simulate the operating conditions prevailing in the experimental column. Separate simulations were carried out for each of the particle sizes, i.e., using one size of particles at a time.

5.4.1.1   *Liquid residence time distribution (RTD)*

The Residence Time Distribution (RTD) obtained from CFD simulation is compared with the experimental RTD in Figure 5.7. Since the dominant particle size (d_{80}) for the modelled column was mostly particles of about 45 µm size [2], the CFD results that were compared with the experimental liquid RTD are those that were run with the 44 µm average particle size. The CFD results compare favourably with the experimental data as shown in Figure 5.7.

The mixing parameters calculated from the CFD simulated liquid RTD, together with the predicted air holdup are compared with the literature experimental data inTable 5.4. Both the liquid mean residence time and the vessel dispersion number are reasonably well predicted by the CFD simulations. However, the predicted air holdup is larger than the measured one. Dobby and Finch [58] also noted that the measured air holdup was smaller than would be expected for bubbles of approximately 1 mm size. However, the reason for the small air holdup value is not clear from their experimental data. One of the possible reasons could be that the experimental air holdup was probably measured near the bottom of the column in which case the air holdup would be smaller than the average holdup in the entire column considering the axial gas holdup variation.
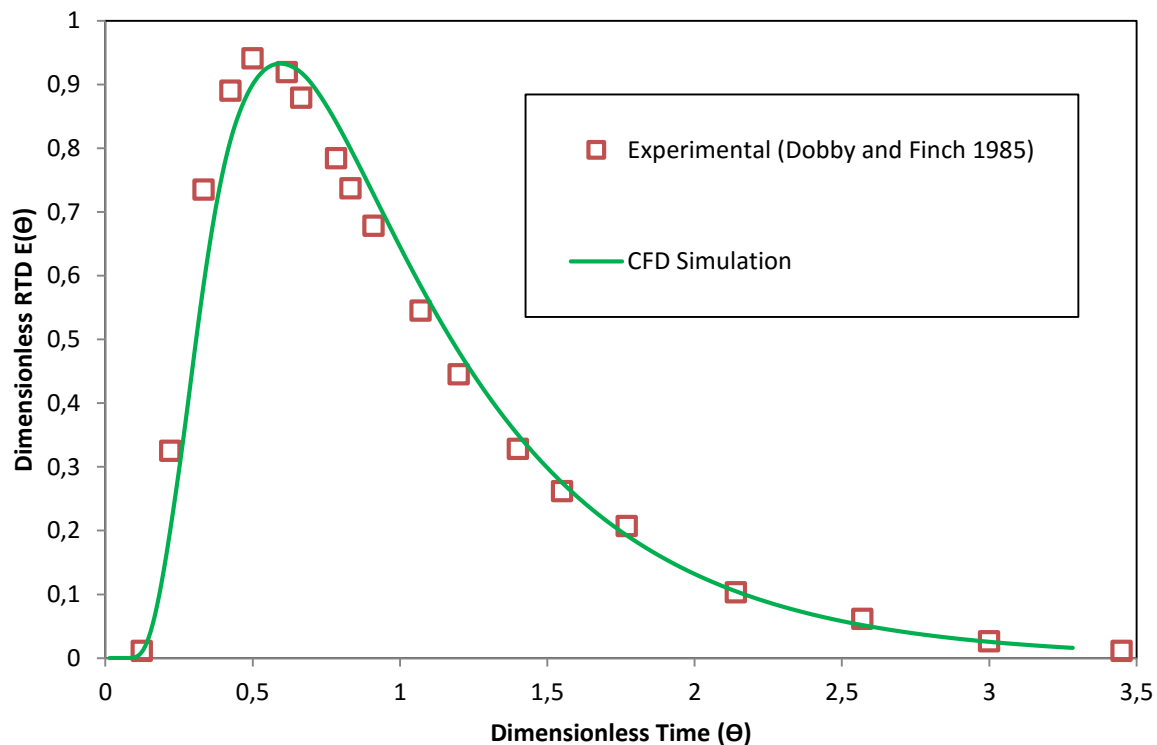
Figure 5.7: Simulated liquid (water) RTD for the square column compared with the experimental data of Dobby and Finch [58].

Table 5.4: Comparison of CFD predicted mixing parameters with experimental data.

Parameter	CFD Prediction	Experimental data[58]
Liquid mean residence time (τ_l) in minutes	11.4	12.6
Vessel dispersion number (N_d)	0.209	0.278
Estimated air holdup, ε_g	0.130	0.055

5.4.1.2 Particle (solids) RTD

Solving the transport equation of the particle age in the column gives the spatial distribution of the age of the particles in the collection zone of the column. The spatial age distribution of 44 µm solids is presented in Figure 5.8 for illustration. The simulated particle age seems to increase from the walls towards the centre of the column. This is as a result of the liquid circulation pattern in which the liquid (water) rises in the centre of the column and descends near the walls. The axial velocity profile of water at the mid-height position in the column is presented in Figure 5.9. It can be seen that the velocity is positive in the centre and negative

92

near the walls of the column. The water is therefore rising in the centre and descending at the walls. The rising water carries with it 'older' particles that had reached the bottom part of the column while the descending water carries with it the 'younger' particles entering the column at the top. The particle age distribution in the column is therefore governed by the established liquid circulation prevailing in the column. The implication of these observations is that the back-mixing effect resulting from liquid circulation in flotation columns might cause short-circuiting of feed to gangue flow as earlier suggested by Xia et al. [15]. Gangue might also flow back to feed or concentrate flow and thus make separation less selective.
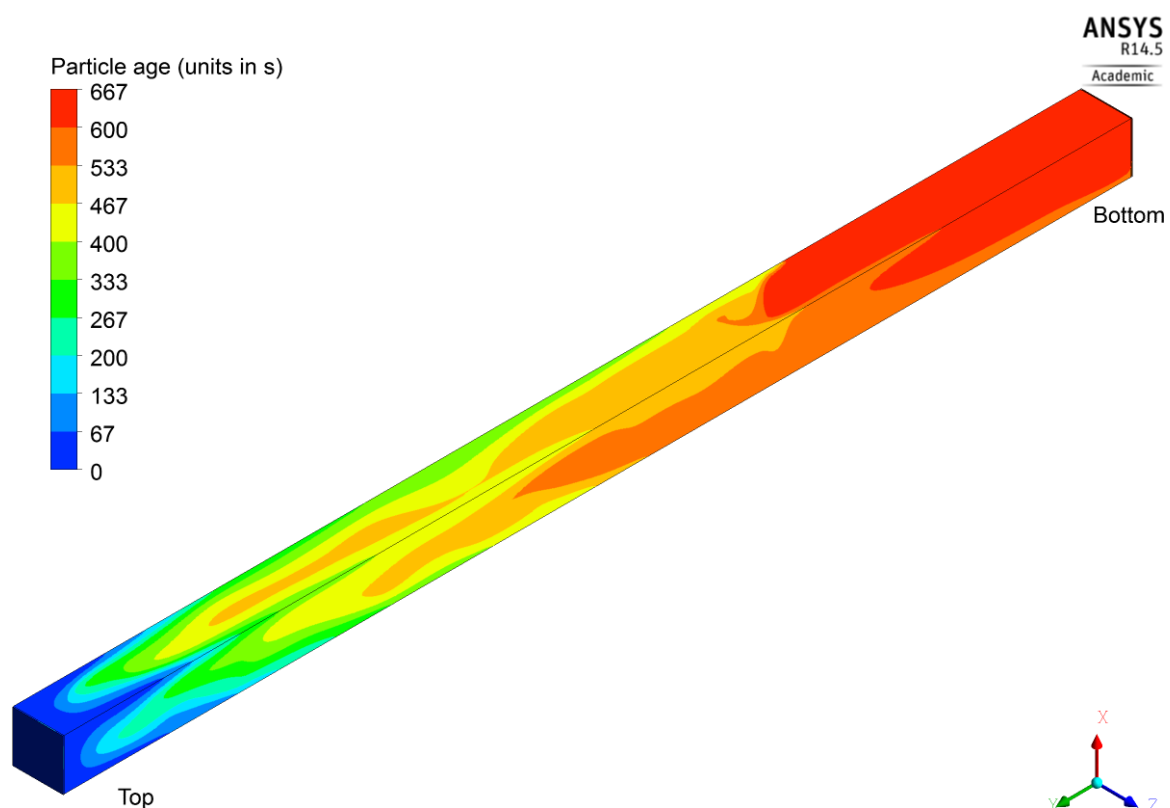
Figure 5.8: Contours of simulated particle age distribution in the square column; particle size = 44 μm.
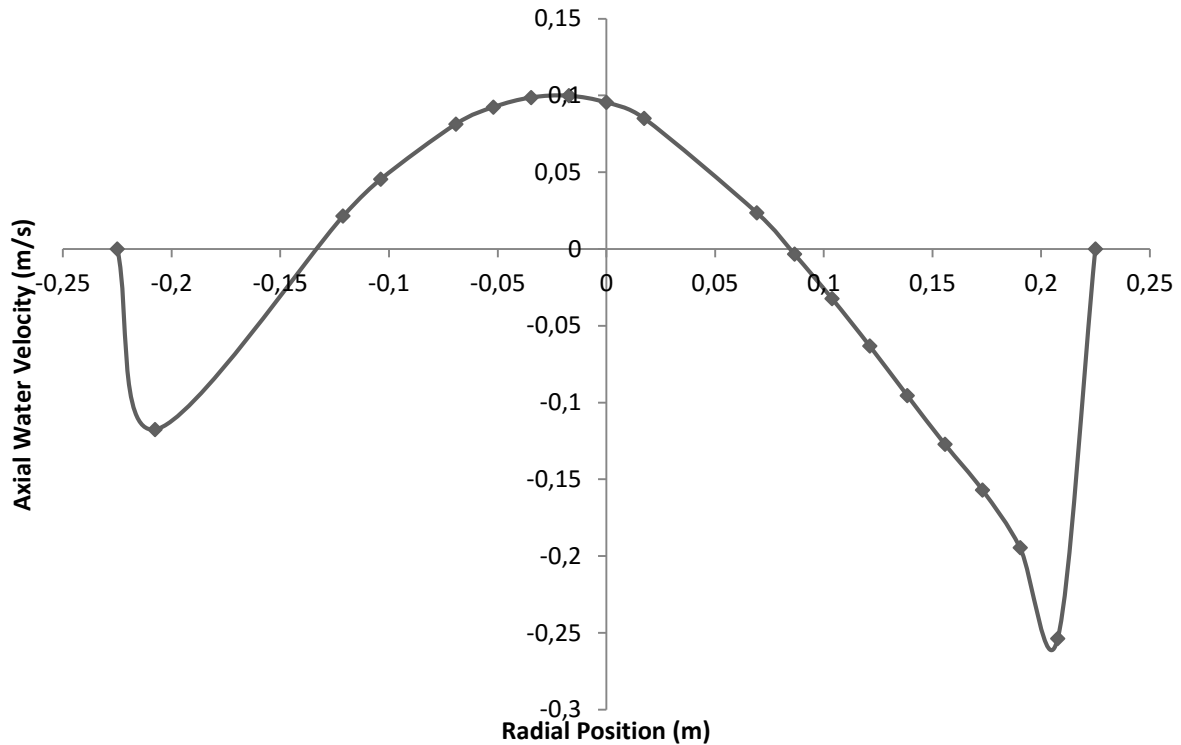
Figure 5.9: Axial velocity profile of water showing the circulation pattern with upward flow at the centre and downward flow near the column walls (square column).

The area weighted average or mass weighted average age of the particles at the outlet of the column gives the particle mean residence time. In Figure 5.10, the particle mean residence times obtained from the CFD simulations using the particle age scalar equation are compared with the experimental values reported by Dobby and Finch [58]. The Mean Absolute Relative Error (MARE) between the CFD predictions and the experimental data was calculated from the following equation:

$$MARE(\%) = 100 \frac{1}{N} \Sigma \left| 1 - \frac{\tau_{CFD}}{\tau_{Exp.}} \right| \tag{5.19}$$

With Mean Absolute Relative Error (MARE) equal to 7.8% the CFD results compared well with the experimental data. The simulation results in Figure 5.10 also show that the solids (particle) mean residence time decreases with increasing particle size. This is also evident in the corresponding experimental data. In comparison with the simulated liquid mean residence time of 11.4 minutes (refer to Table 5.4), the predicted mean residence time of 5 minutes for the largest particle size (125 μm) was about 50% of the liquid residence time. On the other

94

hand, the smallest particle size (44 µm) had mean residence time (10.3 minutes) similar to the liquid one.
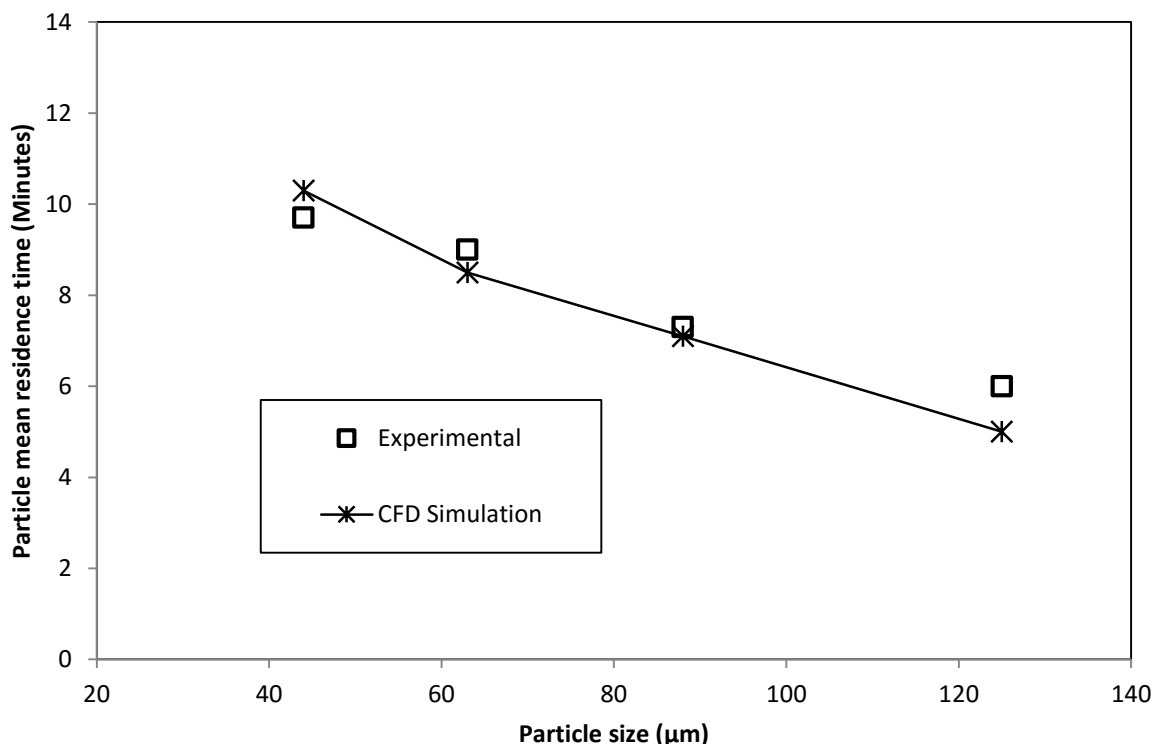
Figure 5.10: Comparison of CFD predicted (simulation) and experimental measurements [58] of particle mean residence time vs particle size.

5.4.1.3 *Comparison of liquid (water) and solids flow patterns*

A comparison of the liquid and solids axial velocity profiles was undertaken as illustrated in Figure 5.11 and Figure 5.12 in order to determine whether the solids dispersion number and the liquid one were equivalent as suggested by previous researchers [58, 65, 104]. The axial velocity profiles were taken at the mid-height position in the column. In Figure 5.11, the axial velocity profile of 88 µm solids is compared with the liquid one. It can be observed that the negative part (downward part) of the solids axial velocity is slightly larger than the liquid one while the positive solids velocity (upward part) is less than the liquid one. This is due to the gravitational settling imposed on the solid particles. However, the differences in the velocities of the phases are not large enough to suggest significant differences in their axial mixing. It is therefore reasonable for column flotation design and scale up purposes to assume the equality of the liquid and solids vessel dispersion numbers for this particular particle size.

The axial velocity profile of 125 μm solids is compared with the liquid one in Figure 5.12. It is clearly shown that the axial velocities of the 125 μm solids are now significantly different from the liquid velocities due to the effects of gravity on the particles. Their dispersion coefficients are therefore likely to be different also. The assumption of equal dispersion for solids and liquid phases should not be applicable in this case.
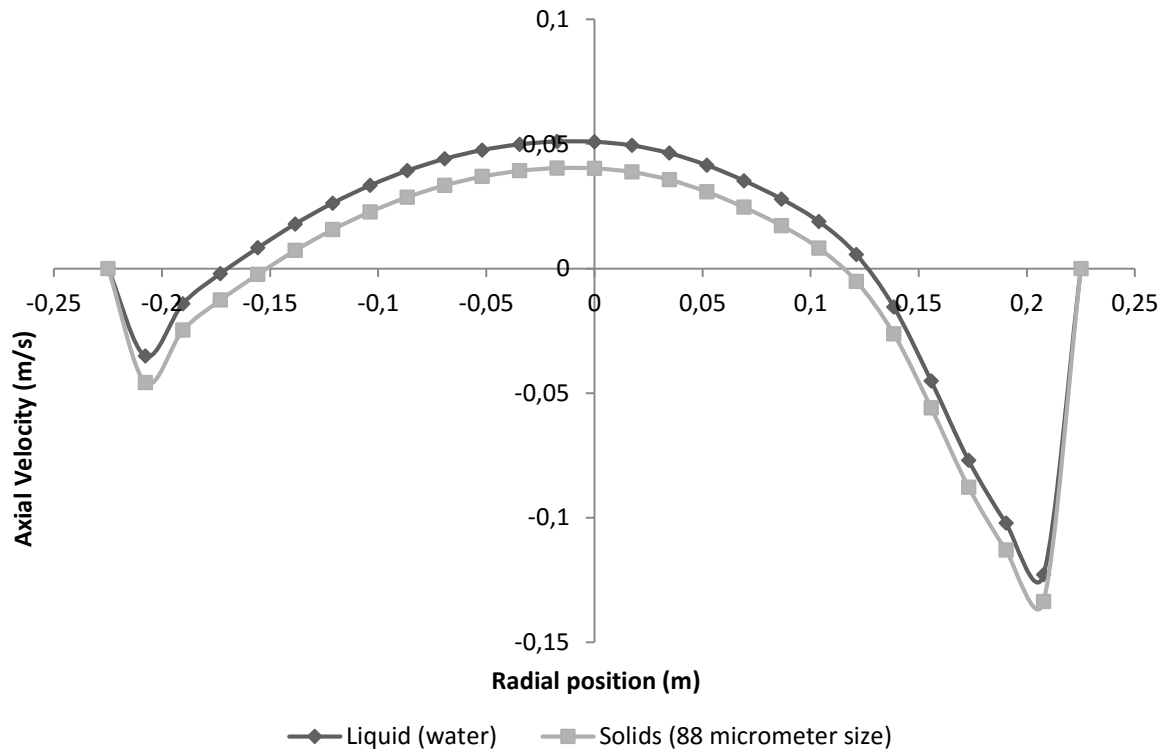
Figure 5.11: Comparison of liquid (water) and solids (88 μm) axial velocity profiles.
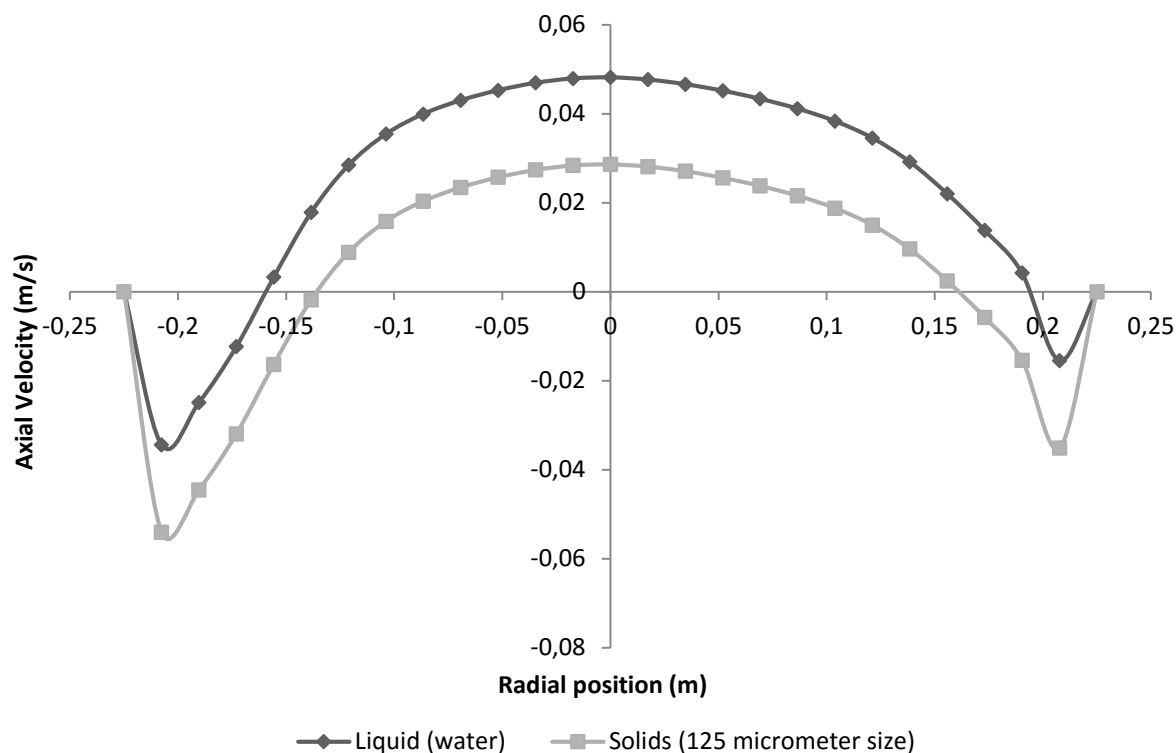
Figure 5.12: Comparison of liquid (water) and solids (125 µm) axial velocity profiles.

5.4.2   Cylindrical column

Another set of CFD simulations were conducted to model the cylindrical column that was used in the work of Yianatos and Bergh [65]. Their work involved both solids and liquid RTD measurements performed using radioactive tracer techniques in a 0.91 m diameter industrial flotation column. For the solids, residence time distributions were measured for three size classes; fine (-39 µm), medium (-75+38 µm), and coarse (-150+75 µm).

In the present study, three average particle sizes representing each of the three size classes were used in the CFD simulations, namely; 19, 56.5, and 112.5 µm. The CFD simulations were performed with one particle size at a time in order to reduce the computational effort required for the simulations. The CFD results for this column are presented as follows.

5.4.2.1   *Liquid residence time distribution (RTD)*

The simulated liquid residence time distribution (RTD) is compared with the experimental RTD in Figure 5.13. Since the particle size in the industrial column was predominantly less than 24 µm [113], the CFD simulation performed with 19 µm particle size is the one that is compared with the experimental liquid RTD data. The CFD simulation is in good agreement with the experimental liquid RTD.

97

The mixing parameters (liquid mean residence time and vessel dispersion number) calculated from the CFD simulated liquid RTD, together with the predicted air holdup are compared with the experimental data of Yianatos and Bergh [65] in Table 5.5. It can be seen that the simulated mixing parameters are in reasonable agreement with the experimental data.
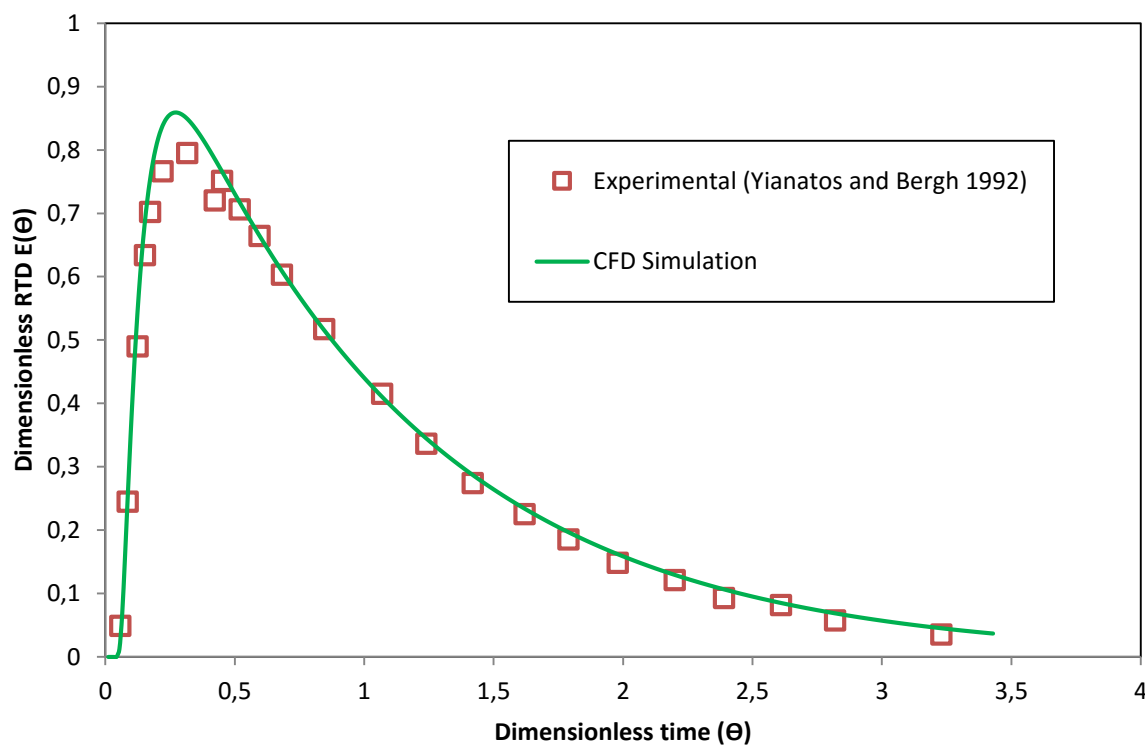
Figure 5.13: Simulated liquid (water) RTD for the cylindrical column compared with the experimental data of Yianatos and Bergh [65].

Table 5.5: Comparison of CFD predicted (simulated) mixing parameters with experimental data.

Parameter	CFD prediction	Experimental data [65]
Liquid mean residence time in minutes (τ_l)	15.5	14.3
Relative variance ($\sigma_\theta{}^2$)	0.561	0.515
Vessel dispersion number (N_d)	0.488	0.41
Gas holdup, ε_g (%)	17.6	18

5.4.2.1.1 Effect of particle size and bubble size on liquid axial mixing

The effect of particle size on the liquid vessel dispersion number was investigated using liquid RTDs obtained from CFD simulations performed with different particle sizes. The results are shown in Figure 5.14 for simulations conducted with two different bubble sizes; 0.8 and 1 mm. It can be seen that increasing the particle size results in a decrease in the liquid vessel dispersion number. On the other hand, previous studies had found that increasing the percentage of solids (wt %) in the feed caused a slight decrease in the liquid mixing intensity inside the column [59, 114, 115]. In other words the liquid vessel dispersion number decreased with increasing solids percentage in the feed (or increasing pulp density).

Subsequently, the feed solids percentage has been included in the empirical correlations that are used for estimating the vessel dispersion number for predicting the recovery in column scale up procedures. However, the decrease in liquid dispersion number observed in the present research as particle size increases suggests that particle size should also be considered in the correlations for estimating the vessel dispersion number. This way the effect of particle size on mineral recovery will also be accounted for in the scale up procedure.

Figure 5.14 also shows that increasing bubble size caused reduction in the liquid dispersion. A similar observation was reported by Xia et al. [15] who observed that a reduction in bubble size resulted in a rise in the axial liquid velocity. The increase in liquid back-mixing can be attributed to the increase in gas holdup resulting from the reduction in bubble size. As the bubble size is reduced, the number of bubbles increases while the bubble rise velocity reduces causing an increase in bubble residence time. The subsequent increase in gas holdup results in higher axial liquid velocity which will cause a stronger back-mixing effect [15, 59].

The effect of bubble size on liquid dispersion is further illustrated in Figure 5.15. The liquid vessel dispersion number decreased from 0.488 to 0.281 when the bubble size was increased from 0.8 mm to 1mm, which is almost a 50% decrease. This is an important finding especially with regard to fine particles flotation where micro bubbles have been suggested to improve the collection efficiency of the fine particles. Using micro bubbles may therefore not necessarily result in improved fine particles recovery because of the increase in liquid back-mixing.
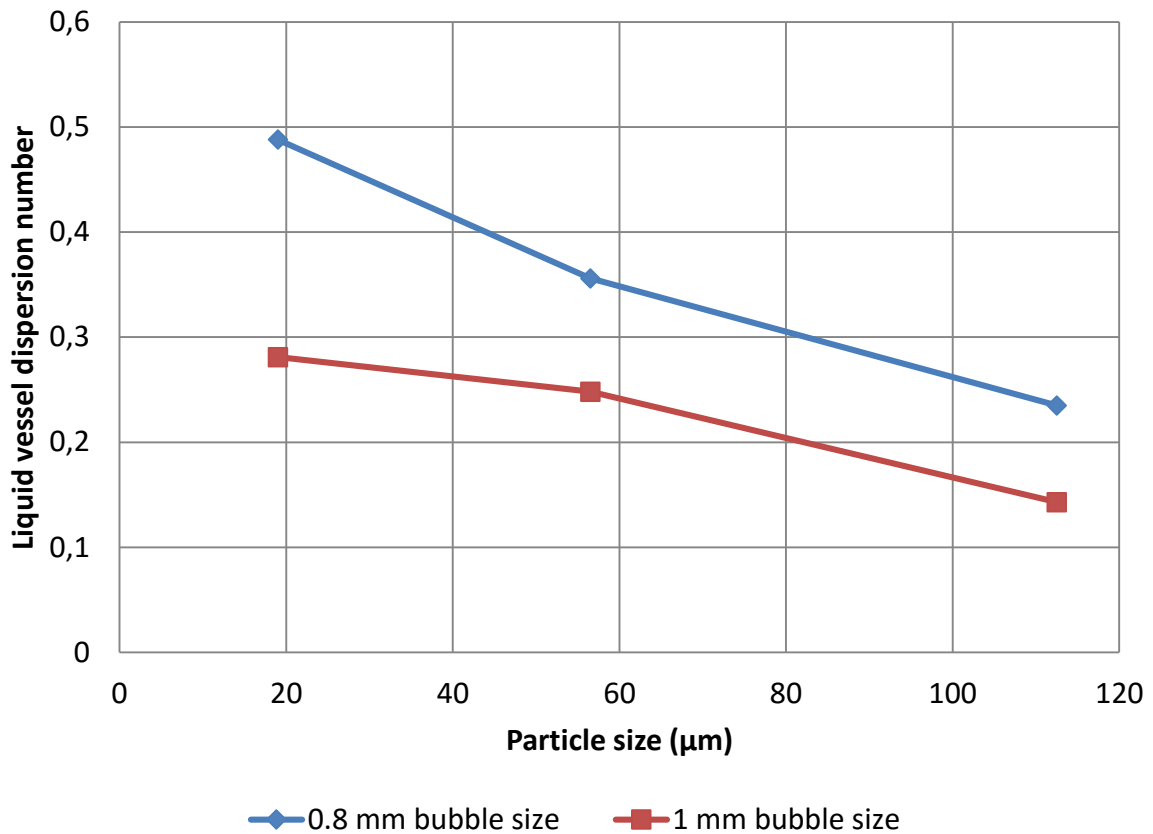
Figure 5.14: Effect of particle size on the liquid vessel dispersion number. The results are from CFD simulations performed with two different bubble sizes, namely 0.8 and 1 mm (cylindrical column).
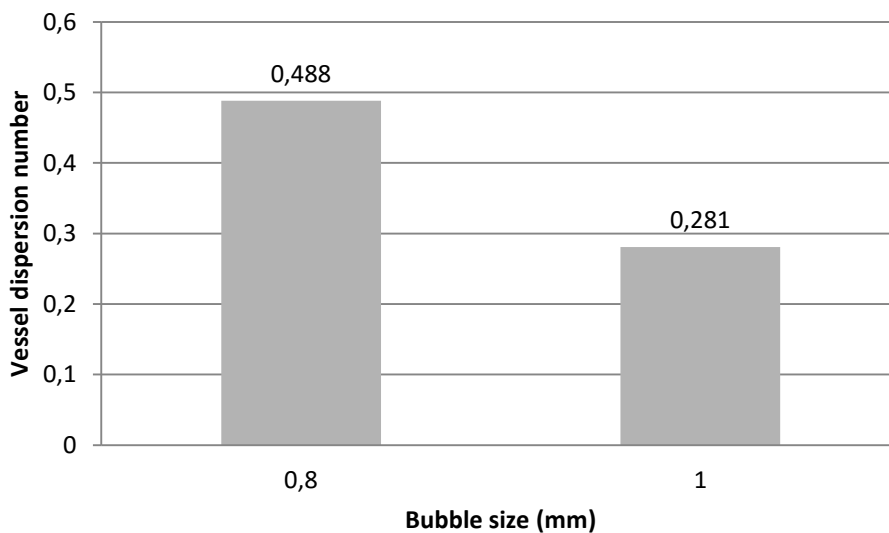
Figure 5.15: Effect of bubble size on the liquid vessel dispersion number (cylindrical column).

5.4.2.2   *Particle (solids) RTD*

5.4.2.2.1 Particle age distribution in the column

The contour plot of the spatial age distribution of 112.5 µm particles at vertical mid-plane position in the column is presented in Figure 5.16. The maximum particle age (red color) is 637 seconds, i.e., about 10.6 minutes. However, the 'oldest' particles in the column are not only found at the outlet but up to the middle height along the column. This is because of the liquid circulation pattern established in the column in which the water rises in the centre of the column and descends near the column walls. The 'older' particles that reach the bottom are therefore lifted with the rising flow up to the middle part of the column. To verify this, the water velocity vectors were compared with the particle age contours in the column as shown in Figure 5.17. This Figure demonstrates that the highest particle ages (red contours) indeed coincide with two large liquid circulation cells occupying the bottom half of the column. Particle age distribution inside the column is therefore affected by the liquid recirculation in the column.
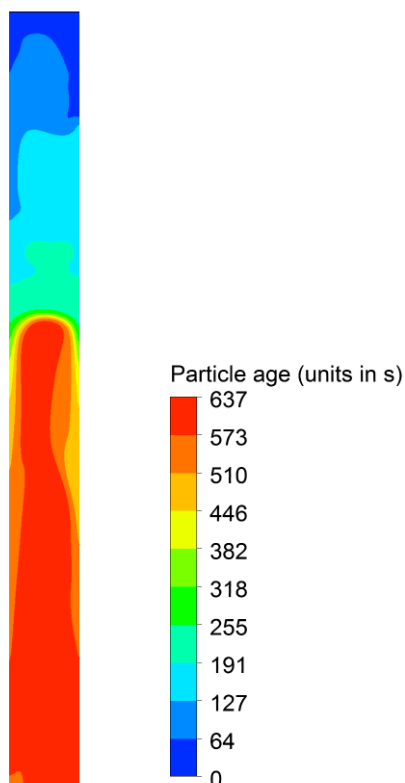
Figure 5.16: Spatial distribution of particle age for 112.5 µm particles; bubble size = 1 mm.
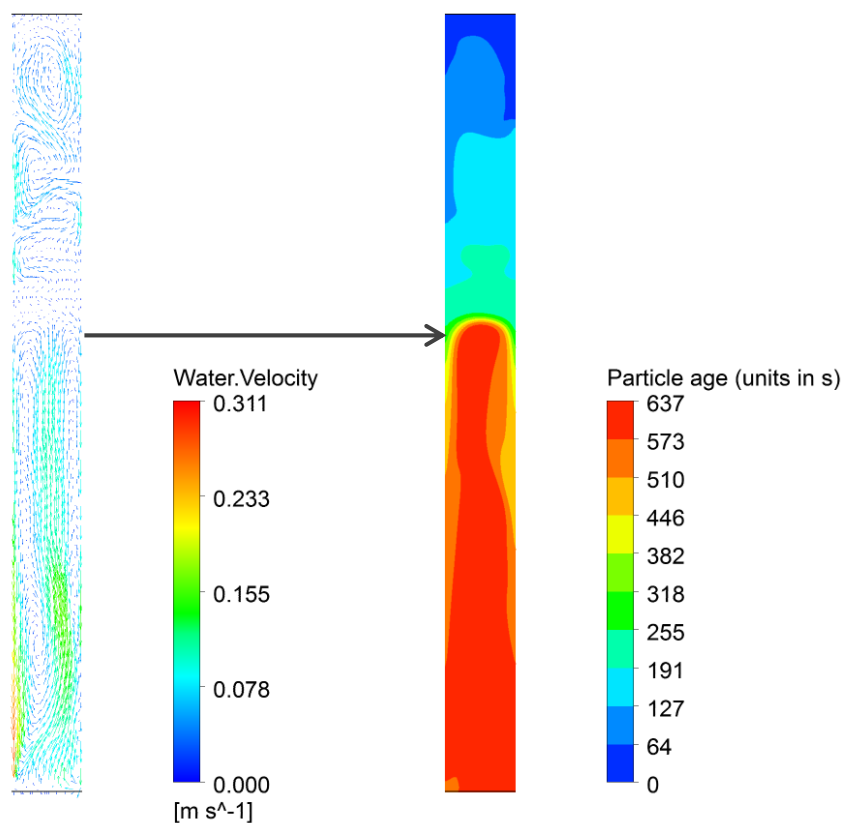
Figure 5.17: Comparison of water velocity vectors with particle age contours in the column.

5.4.2.3 *Comparison of liquid and solids flow patterns at higher solids content (16.2 wt% solids)*

One of the arguments against the assumption of equal liquid and solids dispersion coefficients is that the solids content (3 wt %) that was used in the research that led to that conclusion [58] was too small to highlight any differences between the two phases [61]. Liquid (water) and solids axial velocity profiles obtained from CFD simulations for the 0.91 m diameter column operating with higher solids content (16.2 wt % solids) [65] were therefore compared in order to determine whether their axial dispersion coefficients would still be equal. The liquid and solids (56.5 and 112.5 µm) axial velocity profiles at mid-height location are presented in Figure 5.18 and Figure 5.19. It can be seen that the solids axial velocities are similar to the liquid ones even for the 112.5 µm particle size. The assumption of equal solids and liquid dispersion would therefore be applicable for the operating conditions in this column. Yianatos and Bergh [65] also reported similar conclusions from their experimental RTD measurements.

This result is clearly different from the results observed for 125 μm particle size (Figure 5.12) in the square column. However, it should not be a surprising result considering that the cylindrical column was operating with a higher superficial gas velocity (J_g = 1.8 cm/s) compared to the square column (J_g = 1.4 cm/s). The effect of the superficial gas velocity should therefore be taken into consideration when deciding whether to estimate the solids dispersion from the liquid one. The results here seem to suggest that the liquid and solids mixing characteristics are equivalent for $J_g \geq 1.8$ cm/s.
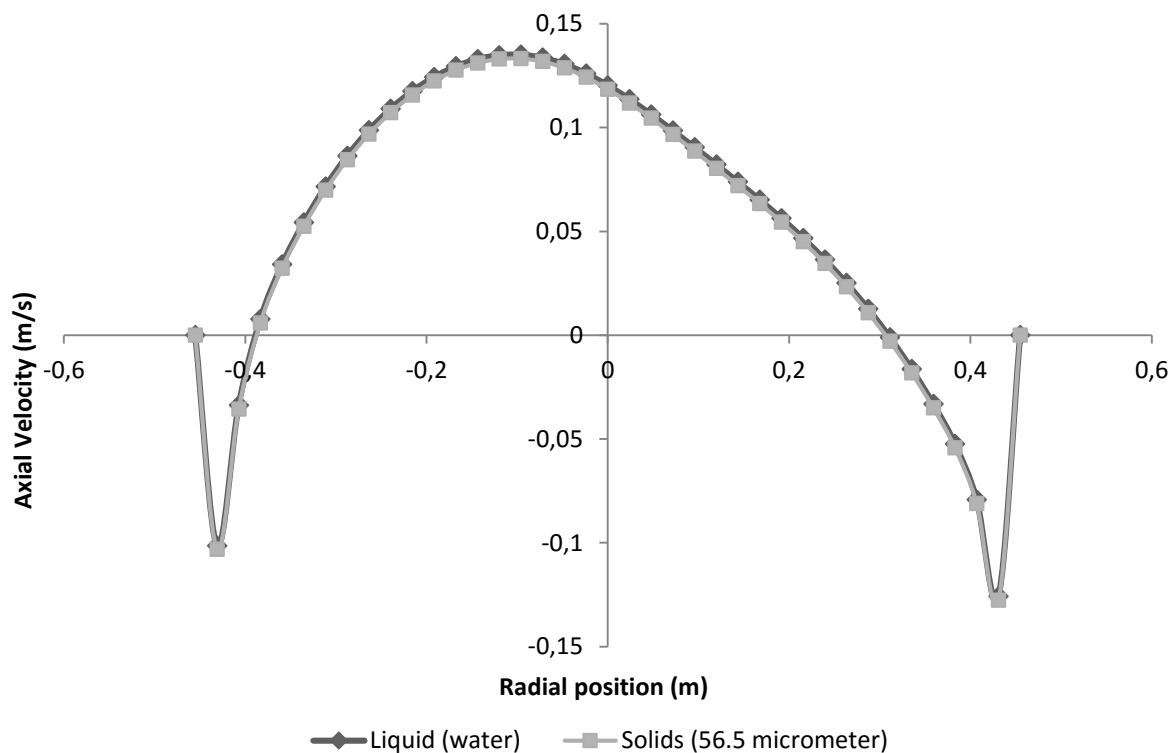
Figure 5.18: Comparison of liquid (water) and solids (56.5 μm) axial velocity profiles.
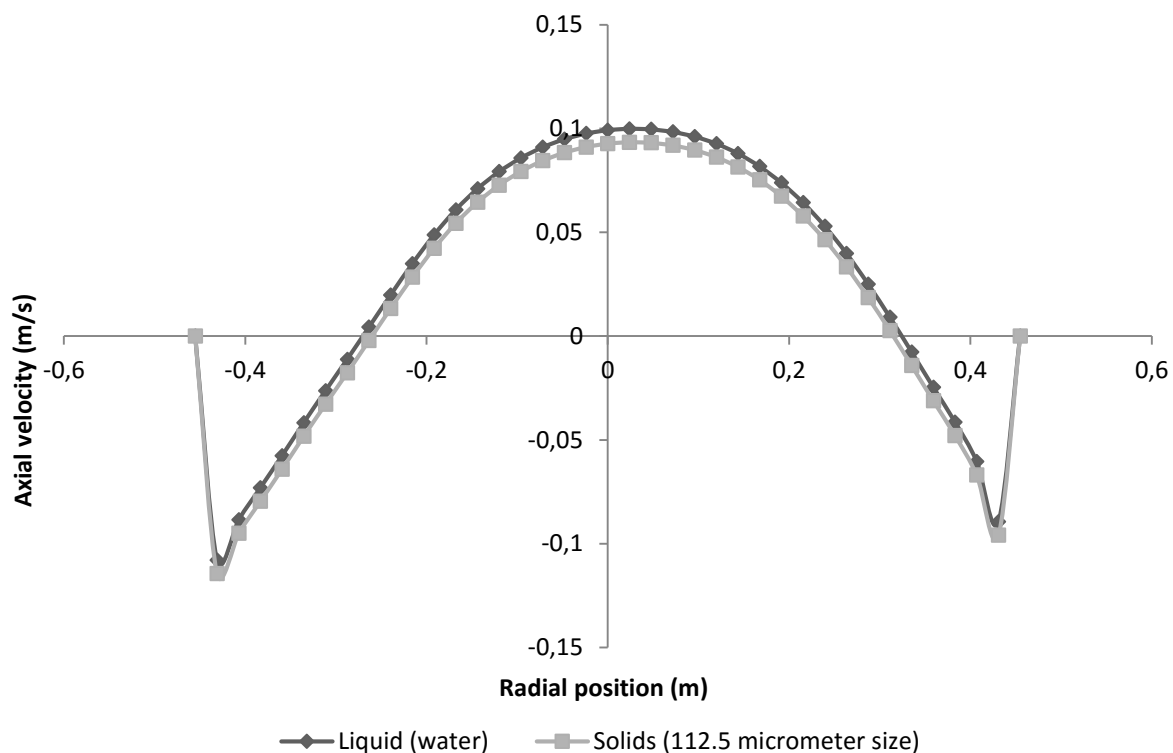
Figure 5.19: Comparison of liquid (water) and solids (112.5 μm) axial velocity profiles.

5.5 Conclusion

In this chapter, liquid RTD and solids RTD have been simulated using the Species transport model and a user defined scalar (UDS) equation that gives the particle age distribution in the column. The CFD simulation results agreed favourably with the experimental data. The results obtained showed that particle residence time decreases with increasing particle size. The residence time of the coarser particles (125 μm) was found to be about 50% of the liquid one while the finer particles (44 μm) had residence time similar to the liquid one.

It was also found that the liquid flow pattern determines particle age distribution inside the column. Particle residence time distribution is therefore affected by liquid recirculation in the column. The equivalence of the liquid and solids axial dispersion coefficients (or vessel dispersion numbers) was investigated by comparing the water and the solids axial velocity profiles. The axial velocities of the two phases were found to be similar, especially for the cylindrical column where the superficial gas velocity was higher (J_g = 1.8 cm/s). The assumption of an equal solids and liquid axial dispersion coefficient was therefore found to be valid for flotation columns operating with Jg ≥ 1.8 cm/s.

In addition, the effects of the bubble size and particle size of the solids on the liquid dispersion were investigated. It was found that increasing particle size of the solids resulted in a decrease in the liquid vessel dispersion number. On the other hand, a decrease in the bubble size caused a significant increase in the liquid vessel dispersion number.

Chapter 6   Investigation of flow regime transition in a column flotation cell using CFD

6.1   Introduction

The focus of this chapter is to apply CFD to investigate flow regime transition in a column flotation cell. Two types of flow characteristics can be distinguished in gas-liquid flows in bubble columns, bubbly flow and churn-turbulent flow. The bubbly flow regime is characterized by uniform flow of bubbles of uniform size. On the other hand, churn-turbulent flow is characterized by a wide variation in bubble sizes with large bubbles rising rapidly and causing liquid circulation.

Flotation columns are normally operated in the bubbly flow regime which is the optimal condition for column flotation [2, 7, 8]. However, it has been generally observed that flotation column performance deteriorates when the superficial gas velocity is increased beyond a certain limit [20]. The identification of this critical or maximum superficial gas velocity is therefore important for optimal operation of flotation columns.

Xu et al. [19, 20] investigated three phenomena that can be used to identify the maximum superficial gas velocity in column flotation: loss of interface, loss of positive bias flow, and loss of bubbly flow. The loss of interface occurs when the hydrodynamic conditions in the froth zone of the column become identical to the conditions prevailing in the collection zone. This will result in the loss of the cleaning action associated with the froth zone.

In column flotation, wash water which is continuously added at the top of the column maintains a net downward flow of water that prevents entrained particles from reaching the concentrate. This net downward flow of water is referred to as positive bias flow. By minimizing entrainment of unwanted particles, a positive bias maximizes concentrate grade. Loss of positive bias occurs when the superficial gas velocity is high enough to cause the reversal of the net flow of water at the froth/collection zone interface.

On the other hand, the loss of bubbly flow occurs when the superficial gas velocity is sufficiently high to bring a transition from bubbly flow conditions into churn-turbulent flow. The increased mixing associated with churn-turbulent flow is unfavorable to the mineral recovery in the column.

Considering the froth and liquid (pulp) phases as distinct flow regimes with different liquid holdups, Langberg and Jameson [21] investigated the hydrodynamic conditions under which the froth and pulp phases can coexist in a flotation cell. The effects of superficial gas velocity and bubble size on the limiting conditions for flow regime coexistence and for countercurrent flow across the froth-liquid interface were studied using a one dimensional two-phase flow model. Their study identified two hydrodynamic limiting conditions relevant to the operation of flotation cells and columns, the limiting condition for the coexistence of the froth and liquid (pulp) phases, and the limiting condition for countercurrent flow.

Of the three phenomena used to identify the maximum superficial gas velocity in column flotation, the loss of bubbly flow is the most difficult to determine [19, 20]. The relationship between gas holdup and superficial gas velocity is used to determine the loss of bubbly flow in the column. In this method, a linear gas holdup versus superficial gas velocity relationship represents bubbly flow while deviation from linearity defines loss of bubbly flow. However, the loss of bubbly flow is difficult to identify with this method because of the gradual nature of the transition from bubbly flow to churn-turbulent conditions in the presence of frother [19].

In this research, the maximum superficial gas velocity for transition from bubbly flow to churn-turbulent flow was studied using Computational Fluid Dynamics (CFD). Besides the gas holdup versus superficial gas velocity relationship, two alternative methods of flow regime characterization are employed to identify the loss of bubbly flow in a pilot scale column flotation cell. The first method involves examining the evolution of radial gas holdup profiles as a function of superficial gas velocity. The shape of the radial gas holdup profile has been recognized as a function of the flow pattern in two phase flows [46, 116]. On the other hand, a graph of gas holdup versus time can also be used to identify the prevailing flow regime in the flotation column [117]. Wide variations in the gas holdup versus time graph characterize churn-turbulent flow conditions while gas holdup is almost constant under bubbly flow conditions.

6.2   Methods for flow regime identification

The relationship between gas holdup and superficial gas velocity can be used to define the prevailing flow regime in the flotation column [118]. In the bubbly flow regime, the gas holdup increases linearly with increasing superficial gas velocity. However, the gas holdup deviates from this linear relationship when the superficial gas velocity is increased above a

certain value as shown in Figure 6.1. The superficial gas velocity at which deviation from the linear relationship occurs is thus the maximum or critical velocity above which the flow regime changes from bubbly flow to churn-turbulent flow. In other words, it is the maximum superficial gas velocity for loss of bubbly flow.
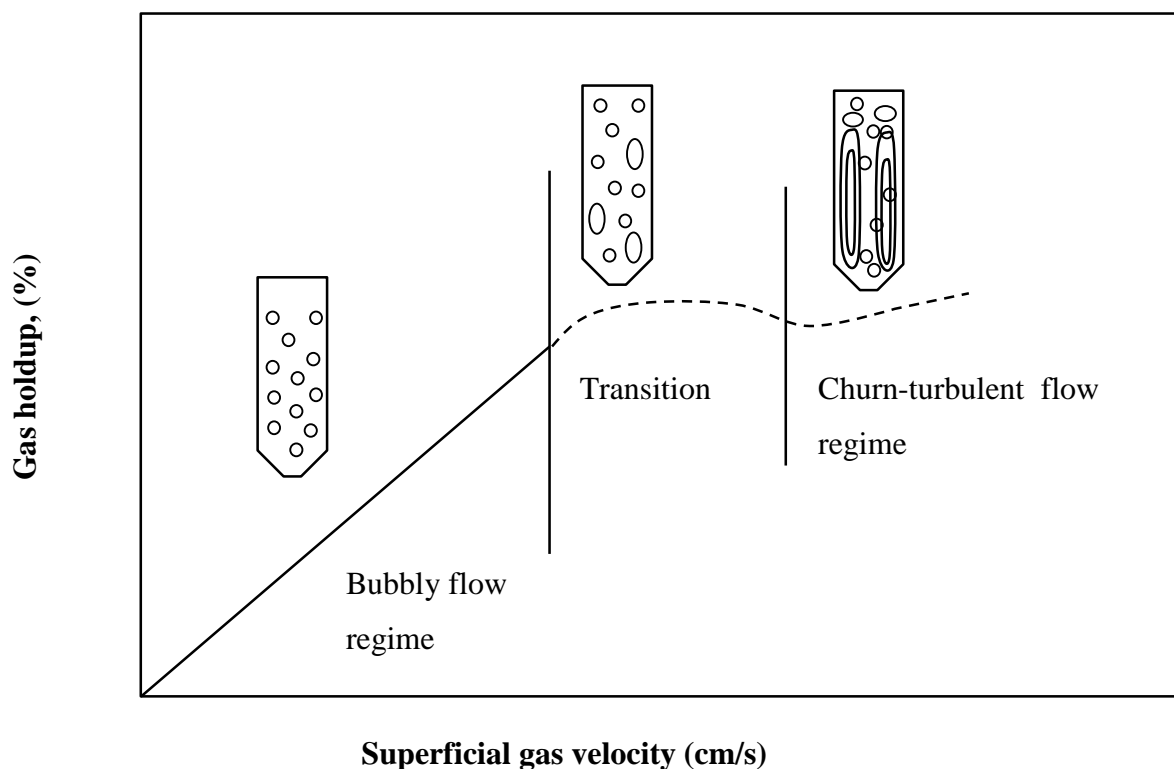
Figure 6.1: Gas holdup as a function of superficial gas velocity (adapted from Finch and Dobby[2]).

Xu et al. [19] applied the gas holdup versus superficial gas velocity relationship to determine the maximum superficial gas velocity for loss of bubbly flow in a pilot scale flotation column. However, these authors reported difficulties in the identification of the regime transition point as a result of the gradual nature of this transition particularly in the presence of frother. The present study therefore applies the following alternative methods to distinguish the different flow regimes and thus identify the maximum velocity above which the transition from bubbly flow to churn-turbulent flow will occur.

6.2.1   Radial Gas Holdup profiles

Two general gas holdup profiles are known to exist, the parabolic profile and the saddle-shaped profile. Kobayasi et al. [116] studied the characteristics of the local void fraction (gas holdup) distribution in air-water two phase flow. They reported a 'peculiar' distribution,

different from the previously accepted power law distribution in bubbly flow conditions. The distribution associated with bubbly flow has its peaks near the pipe wall. On the other hand, the distribution in slug flow had its maximum at the centre of the pipe.

Serizawa et al. [46] also studied various local parameters and turbulence characteristics of concurrent air-water two phase bubbly flow. They found that the distribution of void fraction (radial gas holdup) was a strong function of the flow pattern. The void fraction distribution changed from saddle shaped to parabolic as gas velocity increased. A saddle shaped distribution is therefore associated with bubbly flow conditions, while a parabolic one represents slug flow.

6.2.2   Gas holdup versus Time graph

A plot of gas holdup versus time can also be used to identify the existing flow regime in a column The gas holdup versus time will be relatively constant when the column is in the bubbly flow regime. On the other hand, the gas holdup will show wide variations when the column is operating in the churn-turbulent regime.[117]. A similar method has been used by previous researchers in which variations in conductivity signals were used to characterize the flow regime in the downcomer of a Jameson flotation cell [119, 120].

6.3   Description of the modeled column

The CFD model developed in the present research was used to simulate the flotation column that was used in the experimental work of Xu et al. [19, 20]. The column was made of Plexiglas and was 400 cm in height and 10.16 cm in diameter. The column was operated continuously and air was introduced into the bottom of the column through a cylindrical stainless steel sparger, 3.8 cm in diameter and 7 cm in length. This sparger geometry gives a ratio of column cross-section to sparger surface area of about 1:1. A schematic diagram of the column is presented in Figure 6.2. A detailed description of the experimental set up is presented elsewhere [20].
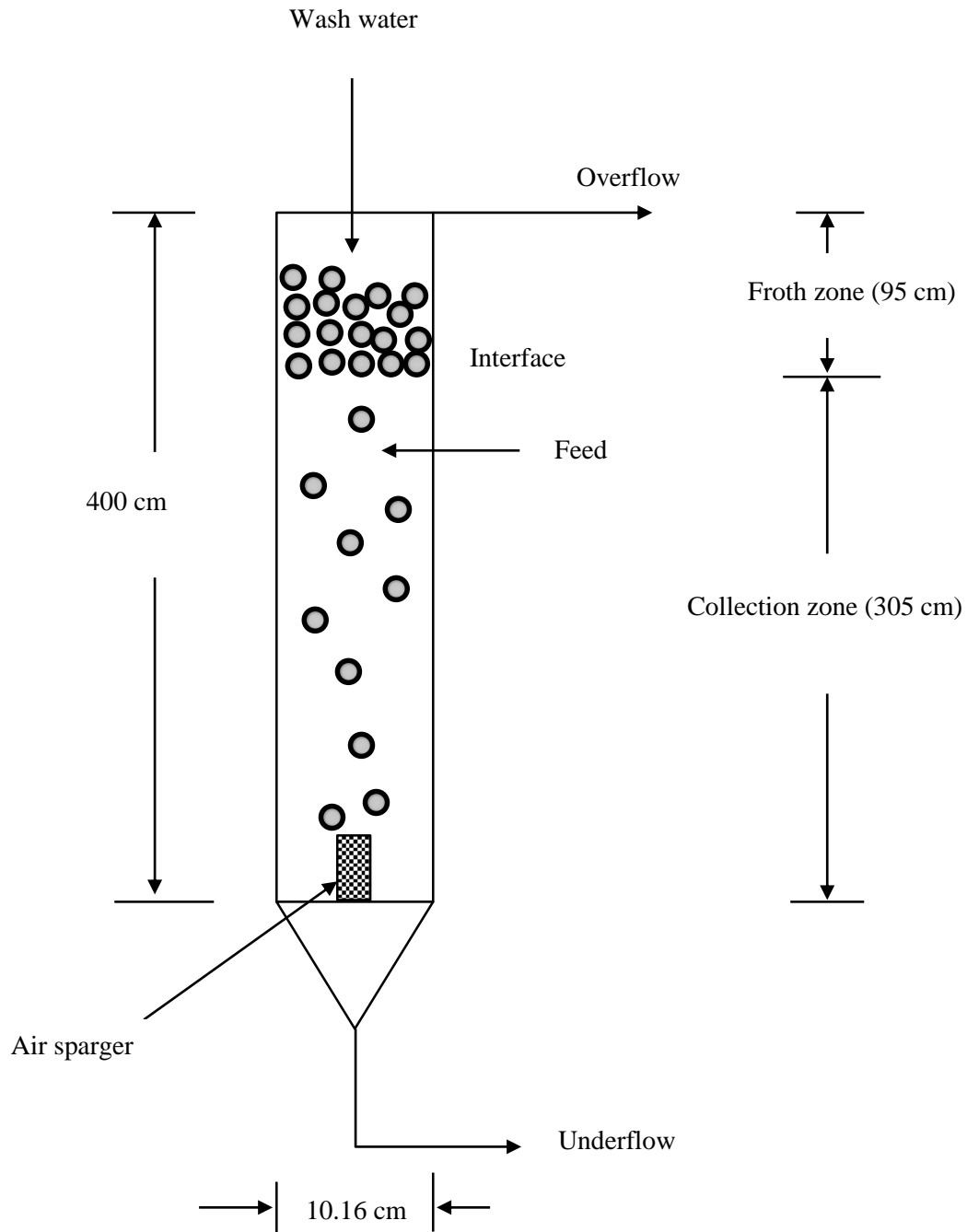
Figure 6.2: Schematic diagram of the modelled experimental column (after Xu et al. [20].).

6.4   CFD Methodology

6.4.1   Geometry and mesh

For the purposes of the present research, the model considers only the collection zone of the flotation column. Therefore the froth zone was not included in the model. A further simplification was achieved by leaving the sparger out in the model geometry. Instead, the air

was introduced from the bottom part of the column over the entire column cross section. This will not affect the required gas holdup prediction since the ratio of column cross-section to sparger surface area was about 1:1 in the experimental flotation column. The result of these simplifications is that the model geometry is reduced to a cylindrical vessel of height equal to the collection zone height (305 cm in this case) and diameter equal to the diameter of the experimental flotation column.

A mesh comprising mainly hexahedral elements was generated over the model geometry using the sweep method in ANSYS Meshing. Five mesh sizes were investigated in order to achieve grid independent numerical results. The mesh sizes are summarized in Table 6.1 together with their respective attributes.

Table 6.1: The five mesh sizes and their respective characteristics.

Mesh	Number of cells	Number of nodes	Minimum Orthogonal Quality	CPU time (Hrs)
Mesh 1	13,940	17,510	0.9318	2.5
Mesh 2	34,160	39,474	0.939	4.5
Mesh 3	79,755	88,560	0.773	14
Mesh 4	98,112	108,433	0.831	16
Mesh 5	114,696	126,764	0.878	17

The axial water and bubble velocity profiles obtained for the different mesh sizes are shown in Figure 6.3 and Figure 6.4, respectively. Grid independence was achieved with mesh 3 to mesh 4 and 5. Mesh 3 (79,755 elements) was therefore selected for all subsequent simulations in this study.

Figure 6.3: Water velocity profiles at mid-height in the collection zone (Height = 152.5 cm).

Figure 6.4: Bubble velocity profiles at mid-height in the collection zone (Height = 152.5 cm).

112

6.4.2   Boundary conditions

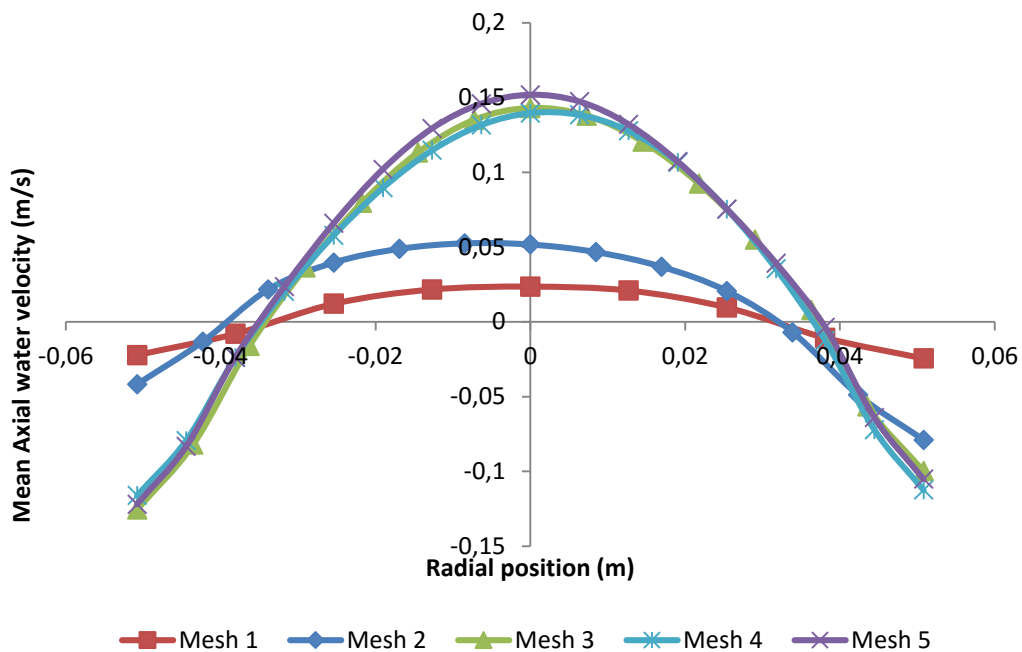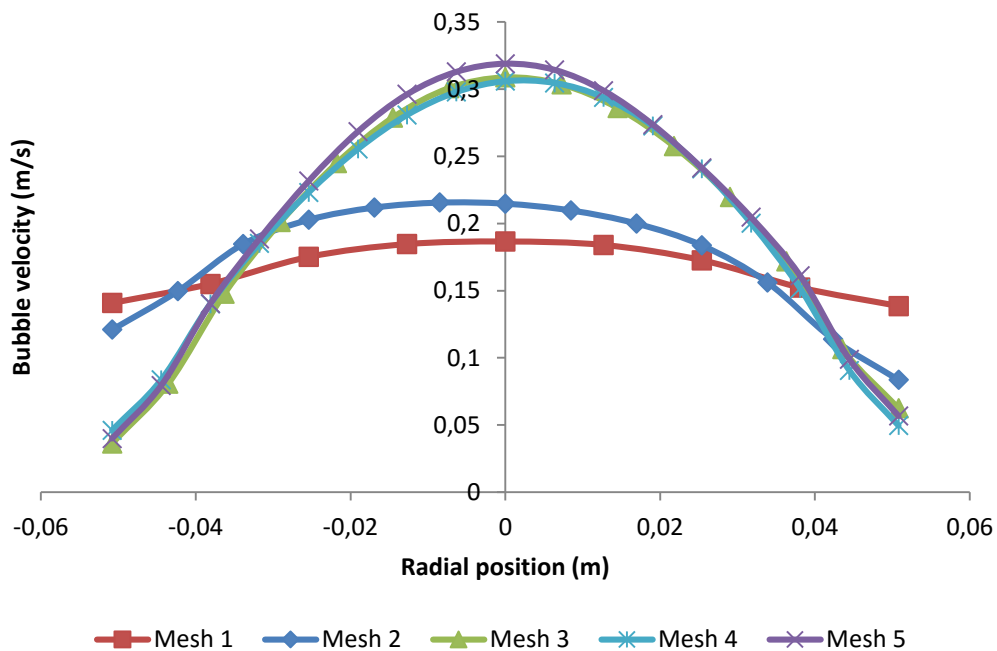Air bubbles were introduced into the column through mass and momentum source terms at the column bottom. The source terms were calculated from the respective superficial gas velocities and were applied over the entire column cross section at the bottom (source) and at the top (sink) of the collection zone.

For the liquid phase, the top of the collection zone was modelled as a velocity inlet boundary where inlet velocity was specified as equal to superficial liquid velocity J_l. Since the computational domain being considered is the collection zone of the column, the superficial liquid velocity must include the feed rate plus the bias water resulting from wash water addition. The superficial liquid velocity is therefore equal to the superficial tailing rate, J_t.

The bottom part was also modelled as velocity inlet where exit velocity was set equal to minus superficial liquid velocity. At the column wall, no slip boundary conditions were applied for both the air bubbles and the liquid phase.

6.4.3   Multiphase Model

The Eulerian-Eulerian (E-E) multiphase modelling approach used in this study has already been described in Chapter 3. Interaction between the phases in the model was accounted for through inclusion of the drag force between phases. The drag force is included in the respective momentum conservation equations as a source term. The continuity and momentum equations for the Eulerian-Eulerian model have been presented in Chapter 3 in equations (3.3) and (3.4) and will not be repeated here for brevity. The volume fraction (or gas holdup) of the secondary phase was calculated from the mass conservation equations as described in section 4.3.3 using equation (4.2).

In the present study, the drag coefficient was calculated using the universal drag laws [94]. In this case, the drag coefficient is defined in different ways depending on whether the prevailing regime is in the viscous regime category, the distorted bubble regime, or the strongly deformed capped bubbles regime. The different regimes are defined on the basis of the Reynolds number. In the viscous regime the drag coefficient is presented as:

$$C_{D_{vis}} = \frac{24}{Re}(1 + 0.1Re^{0.75}) \qquad (6.1)$$

where *Re* is the relative Reynolds number for the primary phase L and the secondary phase G defined as:

$$Re = \frac{\rho_L |\overrightarrow{u_L} - \overrightarrow{u_G}| d_B}{\mu_e} \tag{6.2}$$

and μ_e is the effective viscosity for the bubble-liquid mixture given by:

$$\mu_e = \frac{\mu_L}{1 - \varepsilon_G} \tag{6.3}$$

In the distorted bubble regime the drag coefficient is given as follows:

$$C_{D_{dis}} = \frac{2}{3} \left(\frac{d_B}{\lambda_{RT}} \right) \left\{ \frac{1 + 17.67 f^{6/7}}{18.67 f} \right\}^2 \ ; f = (1 - \varepsilon_G)^{1.5} \tag{6.4}$$

where λ_{RT} is the Rayleigh-Taylor instability wavelength defined as follows:

$$\lambda_{RT} = \left(\frac{\sigma}{g \Delta \rho_{GL}} \right)^{0.5} \tag{6.5}$$

and σ is the surface tension, g the gravitational acceleration, and $\Delta\rho_{GL}$ is the absolute value of the density difference between the phases *G* and *L*.

For the strongly deformed, capped bubbles regime, the following drag coefficient is used:

$$C_{D_{cap}} = \frac{8}{3} (1 - \varepsilon_G)^2 \tag{6.6}$$

Under churn-turbulent flow conditions, the drag coefficient is calculated using equation(6.6). Further details about the universal drag laws are available in a recent multiphase flow dynamics book [94].

6.4.4   Turbulence Modeling

Turbulence in the continuous phase was modelled using the k-ϵ realizable turbulence model, a RANS (Reynolds- Averaged Navier- Stokes) based model in which the time averaged Navier-Stokes (RANS) equations are solved in place of the instantaneous Navier-Stokes equations to produce a time averaged flow field. The averaging procedure introduces additional unknown terms; the Reynolds stresses which are subsequently resolved by employing Boussinesq's eddy viscosity concept where the Reynolds stresses (or turbulent stresses) are related to the velocity gradients according to equation (3.9) as described in section 3.4.3 where the realizaable k-e model is explained.

6.4.5   Numerical solution methods

The momentum and volume fraction equations were discretized using the first order upwind scheme. The first order upwind scheme was also employed for turbulence kinetic energy and dissipation rate discretization. A time step size of 0.05s was used in all the simulations. The simulations were run up to a flow time of at least 240s. Time averaging was carried out over the last 120s.

6.5   Results and discussion

If the entire range of bubble sizes encompassing the different flow regimes is known, CFD simulations can be conducted for a range of superficial gas velocities covering the different flow regimes. A plot of gas holdup versus superficial gas velocity can then be used to determine the point of departure from bubbly flow conditions as described earlier. For a system comprising of water and air without frother, an empirical formula derived by Shen [117] can be used to calculate the Sauter mean bubble size as a function of the superficial gas velocity. However, a similar empirical equation derived for column flotation conditions where frother plays an important role in determining the bubble size is only limited to superficial gas velocities ranging from 1 to 3 cm/s. The first set of CFD results presented in this study is therefore obtained using bubble sizes calculated for a system without frother. The gas holdup versus superficial gas velocity relationship obtained is then used to delineate the different flow regimes prevailing in the column.

Once the flow regimes are identified, the evolution of radial gas holdup profiles and gas holdup versus time graphs can be examined for the flow regimes determined from the gas holdup versus superficial gas velocity graph. Radial gas holdup profiles and gas holdup versus. time graphs are then used to determine the maximum superficial gas velocity for a column operating with an average bubble size of 1.5 mm which is comparable with typical bubble sizes being used in industrial flotation columns. The radial gas holdup profiles were obtained at the mid-height position (152.5 cm height) in the column. On the other hand, the gas holdup versus time graphs were obtained from a surface monitor located at column mid-height position from which area weighted average gas holdup measurements were recorded at 5 second intervals.

It is important at this stage, to clarify the definition of regime transition and churn-turbulent flow regime as used in the present study. Churn-turbulent flow is normally associated with a wide bubble size distribution including large bubbles. However, the CFD simulations in the

present research were conducted with a single mean bubble size assigned for each superficial gas velocity. Furthermore, in order to investigate the flow regime transition for conditions relevant to column flotation, the other set of CFD simulations was performed with the bubble size held at a constant value of 1.5 mm while increasing the superficial gas velocity to determine the maximum superficial gas velocity for that particular bubble size. The reference to churn-turbulent flow in the present study is therefore not based on a wide bubble size distribution of large bubbles in the presence of smaller ones. On the other hand, a CFD model coupled with a bubble population balance model can be used to predict bubble size distributions in the column. However, the present research did not incorporate bubble population balance modelling.

According to Lockett and Kirkpatrick [121] there are three main reasons for breakaway from ideal bubbly flow; flooding, liquid circulation, and the presence of large bubbles. It should therefore be possible to identify regime transition from changes in the pattern and intensity of the liquid circulation in the column even if changes in bubble size are negligible or absent. On the other hand, the liquid circulation pattern and its intensity depend on the prevailing radial gas holdup profile in the column [48].

Saddle shaped gas holdup profiles have already been related to bubbly flow conditions in two-phase flows [46, 116]. However, the bubbly flow regime is generally characterized by a radially uniform gas holdup distribution [122-124]. Both saddle and flat gas holdup profiles can therefore be considered to indicate the existence of the bubbly flow regime in the column. On the other hand, the churn-turbulent flow regime is generally distinguished by a non-uniform radial gas holdup distribution causing bulk liquid circulation. Parabolic gas holdup profiles are therefore interpreted to signify churn-turbulent flow conditions in the column.

6.5.1   Water and air only (without frother)

For the water and air only (no frother) system, CFD simulations were carried out for superficial gas velocities ranging from 1.01 to 14 cm/s to encompass both the bubbly flow and churn-turbulent flow regimes. The Sauter mean bubble size for a multi-bubble system without frother (i.e., water and air only) can be calculated as a function of the superficial gas velocities from the following empirical formula [117]:

$$d_{BS} = 0.33(J_g)^{0.24} \tag{6.7}$$

This empirical formula was derived for a laboratory flotation column with a porous stainless steel sparger similar to the one that was used in the column being modelled in the present work. The equation was therefore used in the present work to calculate the average bubble sizes that were subsequently used in the CFD simulations.

6.5.1.1   *Gas holdup versus superficial gas velocity (gas rate) graph*

The graph of gas holdup versus superficial gas velocity obtained from CFD simulations is presented in Figure 6.5. The different flow regimes can be cleared delineated as follows:

- Bubbly flow regime; J_g 1.01 – 6.12 cm/s (linear portion of the graph)
- Transition; $6.12 < J_g \leq 11.71$ cm/s (deviation from linear relationship between gas holdup and superficial gas velocity)
- Churn-turbulent flow; $J_g > 11.71$ cm/s (third portion of the gas holdup versus superficial gas velocity graph)

The maximum superficial gas velocity (J_gmax) before loss of bubbly flow is therefore equal to 6.12 cm/s for the water and air only system (without frother). This value compares well with the maximum superficial gas velocity of 5.25 cm/s for loss of bubbly flow predicted from drift flux theory by Xu et al. [20].

Having delineated the different flow regimes using the gas holdup versus superficial gas velocity relationship, the evolution of the radial gas holdup profiles was examined as the superficial gas velocity increased from 1.01 cm/s to 14 cm/s.
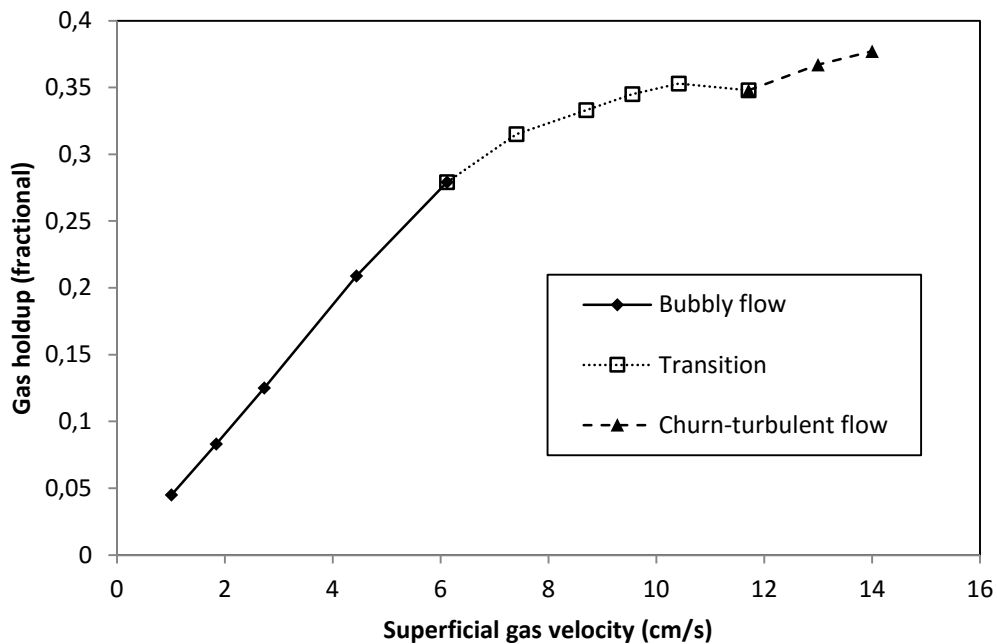
Figure 6.5: CFD predicted gas holdup as a function of superficial gas velocity.

6.5.1.2 *Radial gas holdup profiles*

A number of different types of radial gas holdup profiles were obtained from the CFD simulations including saddle-shaped profiles, flat profiles, and parabolic profiles. These profiles were then related to the flow regimes defined from the gas holdup/superficial gas velocity relationship (Figure 6.5) .

Three types of radial gas holdup profiles were observed in the bubbly flow regime. At the lower superficial gas velocities (J_g 1.01 – 2.73 cm/s) saddle shaped profiles with three distinct peaks were observed with one peak at the centre and two other peaks located near the walls of the column as shown in Figure 6.6 for $J_g = 1.84$ cm/s. The profiles then changed to ones with two near wall peaks and a central minimum point as the superficial gas velocity increased to $J_g = 4.44$ cm/s as illustrated in Figure 6.7. With further increase in the superficial gas velocity the central minimum point disappeared and the radial gas holdup profile became flat. The maximum superficial gas velocity ($J_g max = 6.12$ cm/s) before loss of bubbly flow is therefore characterized by a flat radial gas holdup profile with intermediate features between saddle and parabolic profiles as shown in Figure 6.8.

Figure 6.6: Radial gas holdup profile at J_g = 1.84 cm/s in the bubbly flow regime. The profile is saddle shaped with three distinct peaks.

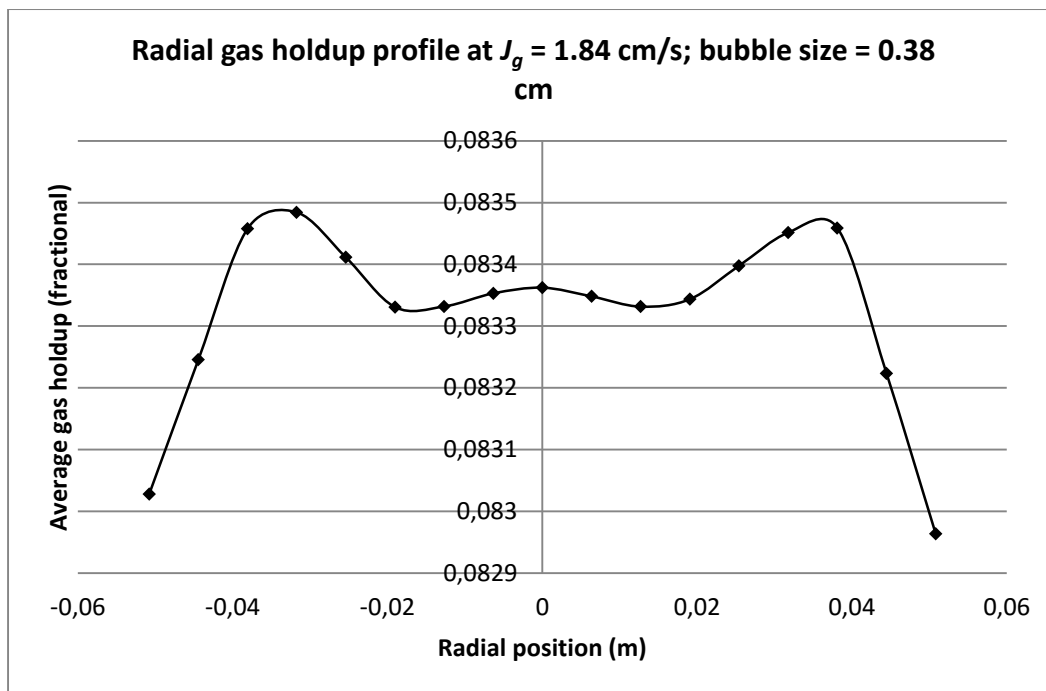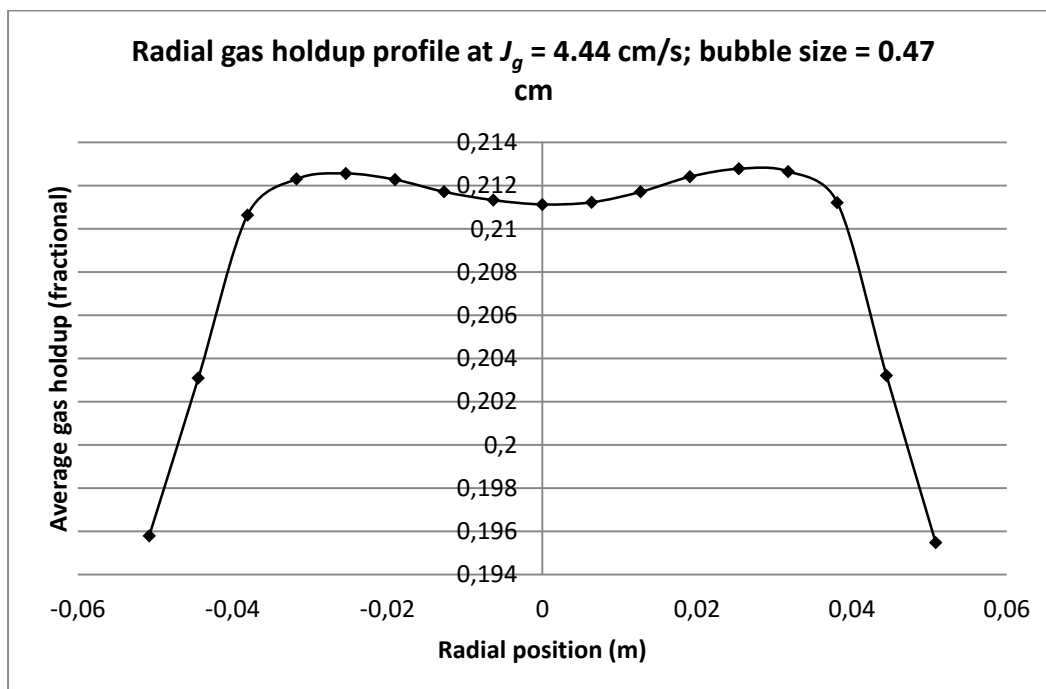**Figure 6.7: Radial gas holdup profiles at J_g = 4.44 cm/s in the bubbly flow regime. The saddle shaped profile is characterised by two near wall peaks and a central minimum value.**

119
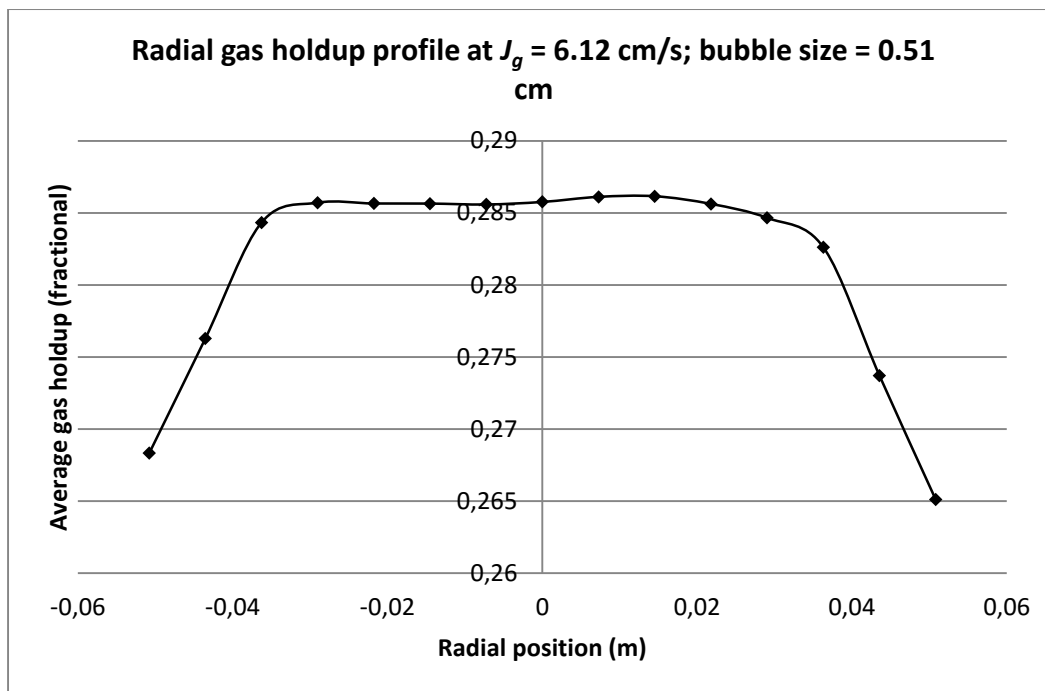
Figure 6.8: Radial gas holdup profile at J_g = 6.12 cm/s ($J_g max$) showing a flat profile with features intermediate between saddle and parabolic profiles.

The transition from bubbly flow to churn-turbulent flow was gradual and characterized by flat (J_g = 7.41 cm/s) to parabolic (J_g 8.70 – 11.71 cm/s) radial gas holdup profiles. The parabolic profiles became progressively steep as the superficial gas velocity increased. Eventually the flow regime changes into churn-turbulent flow (J_g > 11.71 cm/s) which is characterized by steep parabolic gas holdup profiles as shown in Figure 6.9.

6.5.1.3 Gas holdup versus time graphs

Another method that was used to distinguish flow regimes in the water–air system using CFD simulations was by means of gas holdup versus time graphs. Comparing the two extreme cases, the gas holdup versus time was mostly constant in the bubbly flow regime as shown in Figure 6.10 for J_g = 1.84 cm/s, except for moderate variations at the maximum superficial gas velocity. On the hand hand, very wide variations in gas holdup were observed in the churn-turbulent flow regime (i.e., J_g > 11.71 cm/s), as illustrated in Figure 6.11 for J_g = 14 cm/s. The transition from bubbly flow to churn-turbulent flow pattern was gradual and characterized by moderate to large fluctuations in gas holdup in which the gas holdup variations became increasingly intense as the superficial gas velocity increased.
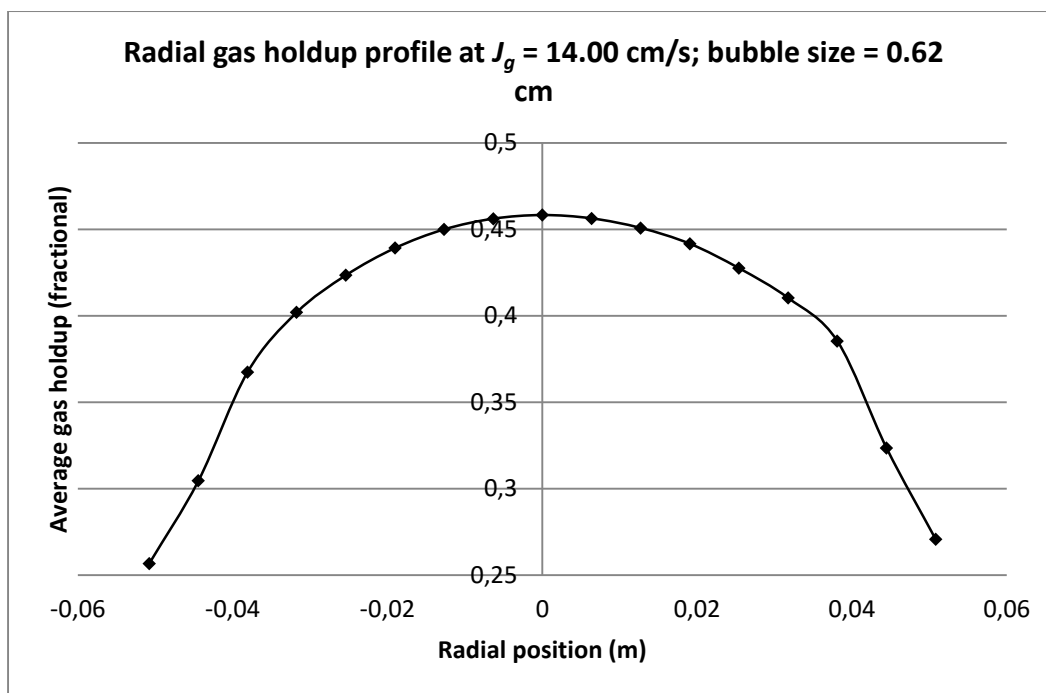
Figure 6.9: Radial gas holdup profile at J_g = 14 cm/s in the churn-turbulent flow regime. The typical profile is a steep parabolic profile.
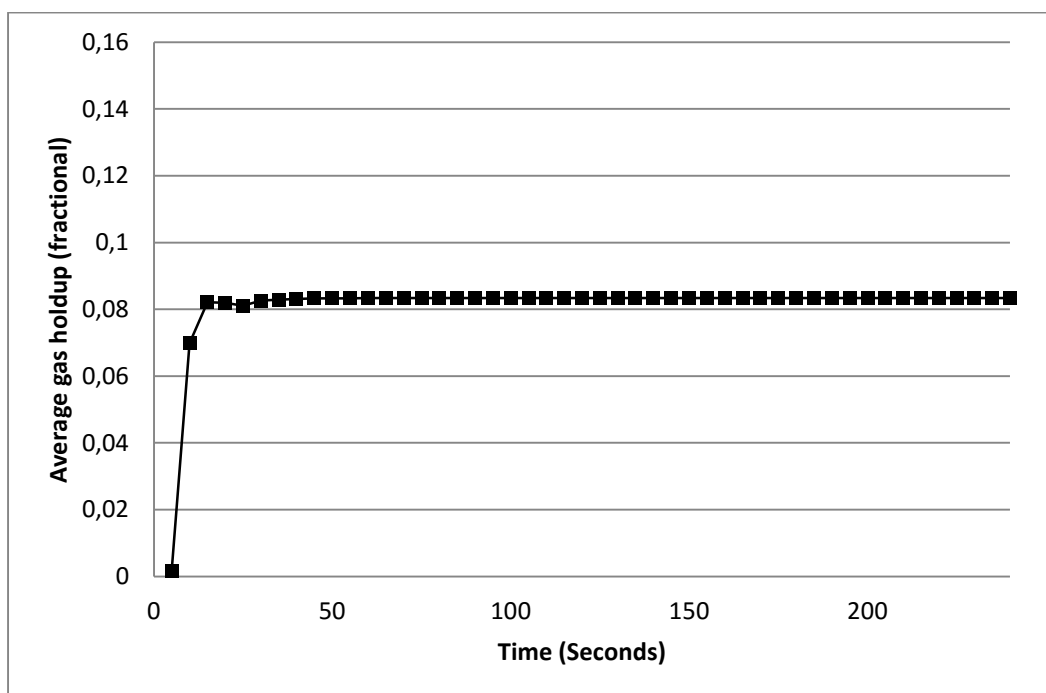
Figure 6.10: Gas holdup versus time graph for J_g = 1.84 cm/s. The constant gas holdup indicates bubbly flow conditions in the column.

121
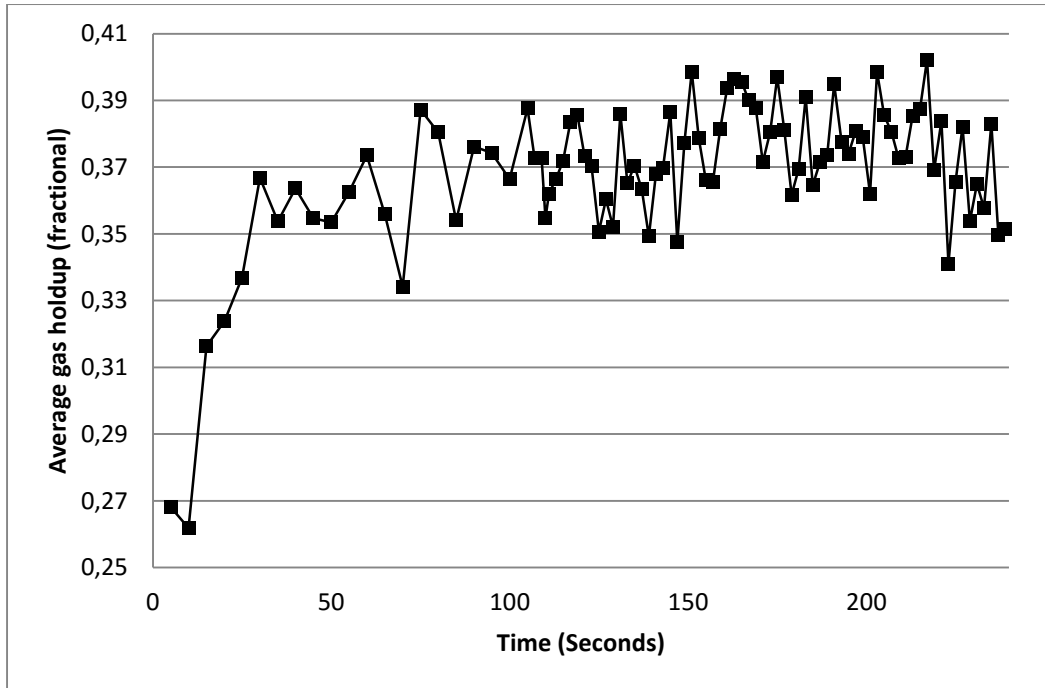
Figure 6.11: Gas holdup versus time graph for J_g = 14 cm/s. The wide variations in gas holdup are a characteristic feature of the churn-turbulent flow regime.

The results from the CFD simulations of the water and air only (no frother) system where bubble sizes are calculated from the superficial gas velocity according to equation (6.7) are summarized in Table 6.2. The progression from bubbly flow conditions to churn-turbulent flow can also be clearly appreciated from this Table. The distinguishing characteristics of the flow regimes are summarised in Table 6.3.

Table 6.2: Summary of CFD simulation of the water and air system (without frother); $J_{g,max}$ **= 6.12 cm/s.**

J_g (cm/s)	Sauter mean bubble size, d_{BS} (cm)	Gas holdup (fractional)	Gas holdup profile	Gas holdup versus Time	Comments
1.01	0.33	0.045	Saddle with three peaks	Constant	Bubbly flow
1.84	0.38	0.083	Saddle with three peaks	Constant	Bubbly flow
2.73	0.42	0.125	Saddle with three peaks	Almost constant	Bubbly flow
4.44	0.47	0.209	Saddle profile with two near wall peaks	Almost constant	Bubbly flow
6.12	0.51	0.279	Flat profile with intermediate features between parabolic and saddle profiles	Small to moderate variations	Bubbly flow (maximum superficial gas velocity)
7.41	0.53	0.315	Flat	Moderate variations	Transition
8.70	0.55	0.333	Flat-like parabolic	Moderate variations	Transition
9.56	0.57	0.345	Parabolic	Significant variations	Transition
10.42	0.58	0.353	Parabolic	Significant variations	Transition
11.71	0.60	0.348	Steep	Large	Transition

J_g (cm/s)	Sauter mean bubble size, d_{BS} (cm)	Gas holdup (fractional)	Gas holdup profile	Gas holdup versus Time	Comments
			parabolic	variations	(last point)
13.00	0.61	0.367	Steep parabolic	Wide variations (large variations)	Churn-turbulent flow
14.00	0.62	0.377	Steep parabolic	Wide variations (large variations)	Churn-turbulent flow

Table 6.3: Summary of the characteristics of the different flow regimes.

Flow regime	Description/characteristics
Bubbly flow	• Characterised by saddle-shaped radial gas holdup profiles accompanied by a constant Gas holdup versus Time graph • The profiles at lower J_g have three peaks that give way to profiles with two near-wall peaks and a central minimum and eventually flat profiles as J_g increases
Transition	• Characterised by flat to parabolic gas holdup profiles • The profiles become increasingly steep with increasing J_g while Gas holdup versus Time varies from moderate to large fluctuations
Churn-turbulent flow	• Characterised by steep parabolic profiles with very wide variations in Gas holdup versus Time

6.5.2   Water with frother (as in column flotation)

In flotation columns, the bubble size depends not only on the superficial gas velocity but also on other physical chemical characteristics of the gas-liquid system. In this case, the bubble size can be calculated as a function of the superficial gas velocity according to the following relationship [2, 8].

$$d_B = C\left(J_g\right)^n \tag{6.8}$$

where C and n are constants. The constant C is a fitting parameter which depends mainly on frother concentration, the sparger size and column size. Simulations were carried out for the experimental conditions used by Xu et al. [19, 20] particularly the case in which the frother concentration was 10 ppm. The value of C was therefore equal to 1 while n was 0.25.

The gas holdup obtained from the CFD simulations is plotted as a function of superficial gas velocity in Figure 6.12. The experimental data from Xu et al. [19] are included in the Figure for comparison. It can be seen that the predicted gas holdup is in good agreement with the experimental data up to superficial gas velocity J_g = 3.60 cm/s. Above J_g = 3.60 cm/s, the relationship in equation (6.8) is not applicable because the value of the exponent n (0.25) is valid for J_g 1 – 3 cm/s [8]. Unfortunately there is no equation relating bubble size and superficial gas velocity for flow conditions above J_g = 3 cm/s. Therefore, the gas holdup versus superficial gas velocity graph obtained from CFD simulations cannot be used to determine the maximum superficial gas velocity since the range of bubble sizes for the different flow regimes cannot be completely determined.

On the other hand, Xu et al. [19] used the gas holdup versus superficial gas velocity relationship to identify the maximum gas velocity for loss of bubbly flow. However, they reported a gradual and unclear transition from bubbly flow to churn-turbulent flow conditions. The maximum superficial gas velocity for conditions applicable in flotation columns can be obtained using radial gas holdup profiles and the gas holdup versus time graphs as already described. In this regard, CFD simulations were performed for a stipulated bubble size of 1.5 mm which is similar to common bubble sizes used in column flotation. The bubble size was held constant during the simulations while increasing the superficial gas velocity to encompass both bubbly flow and churn-turbulent flow conditions.
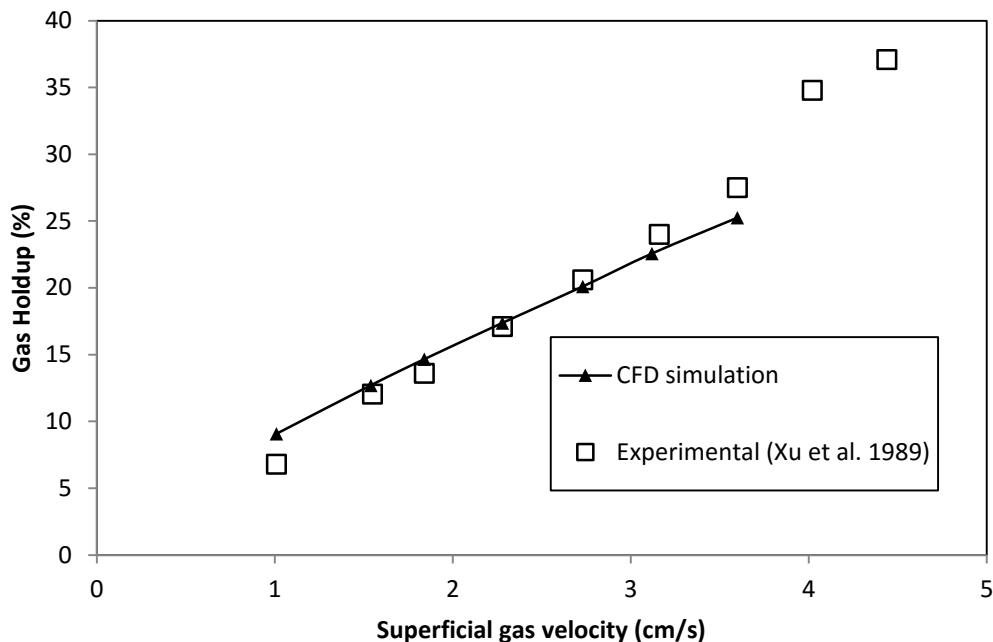
Figure 6.12: Comparison of CFD predicted gas holdup with experimental data [19].

6.5.3   Maximum superficial gas velocity for a column operating with 1.5 mm average bubble size

CFD Simulations were performed with a constant bubble size of 1.5 mm for superficial gas velocities   ranging   from J_g = 1.01   to   6.12   cm/s.   The   liquid   superficial   velocity   was maintained at J_l = 0.38 cm/s. Radial gas holdup profiles were examined for all the superficial gas velocities together with their corresponding gas holdup versus time plots. The following results were obtained.

Saddle shaped radial gas holdup profiles with three peaks were observed for J_g = 1.01 to 1.54 cm/s. The radial gas holdup profile for J_g 1.01 cm/s is presented in Figure 6.13 for elaboration. The profiles then changed to ones with two distinct peaks near to the column wall as Jg increased (J_g 1.84 to 2.73 cm/s). On the other hand, a flat profile with intermediate features between saddle-shaped and parabolic profiles was observed for J_g = 3.12 cm/s. The column was therefore operating under bubbly flow conditions from J_g = 1.01 to 3.12 cm/s.

Gas holdup versus time graphs were used to confirm the existing flow regime in the column. A relatively constant gas holdup versus time was observed for J_g = 1.01 – 1.84 cm/s while moderate fluctuations in gas holdup were observed from J_g = 2.28 – 3.12 cm/s, confirming that the column was indeed in the bubbly flow regime in this range of superficial gas

velocities. The Gas holdup versus Time graph for J_g = 1.01 cm/s is given in Figure 6.14 for illustration.

Figure 6.13: Radial gas holdup profile at J_g = 1.01 cm/s (Bubble size = 1.5 mm).
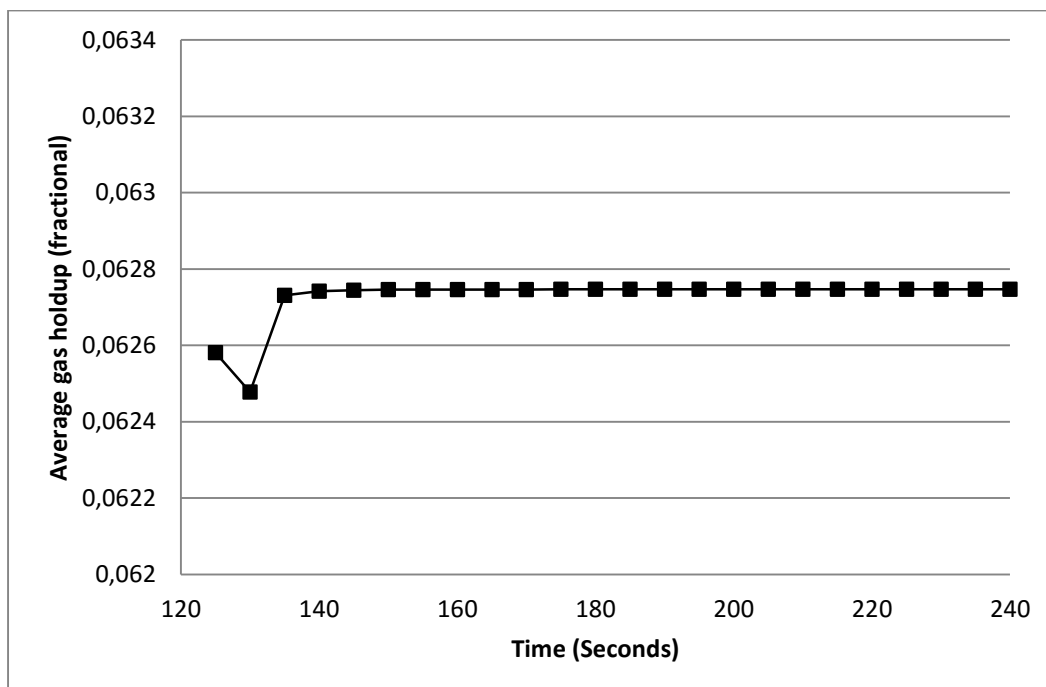
Figure 6.14: Gas holdup versus Time for J_g = 1.01 cm/s (Bubble size = 1.5 mm).

The maximum (critical) superficial gas velocity for transition into churn-turbulent flow was identified by the first appearance of flat radial gas holdup profiles with intermediate features

127

between parabolic and saddle shaped profiles at J_g = 3.12 cm/s. Thus, for a constant bubble size of 1.5 mm the transition to churn-turbulent flow begins at J_g = 3.6 cm/s. The maximum superficial gas velocity ($J_{g,max}$) before loss of bubbly flow is therefore 3.12 cm/s for a flotation column operating with an average bubble size of 1.5 mm at superficial liquid velocity (J_l) equal to 0.38 cm/s. This compares favorably with the maximum gas velocity of 3.60 cm/s reported by Xu et al. [19, 20] with reference to loss of interface. Indeed these authors did report that loss of interface and loss of bubbly flow occurred at approximately the same superficial gas velocities. The predicted gas holdup at $J_{g,max}$ is equal to 20.1% which compares favorably with the maximum gas holdup of 20 to 24% reported by Dobby et al. [44].

The radial gas holdup profile at $J_{g,max}$ is shown in Figure 6.15 and its corresponding Gas holdup versus Time graph in Figure 6.16. It can be seen that the maximum superficial gas velocity is characterized by a flat gas holdup profile accompanied by moderate gas holdup fluctuations.
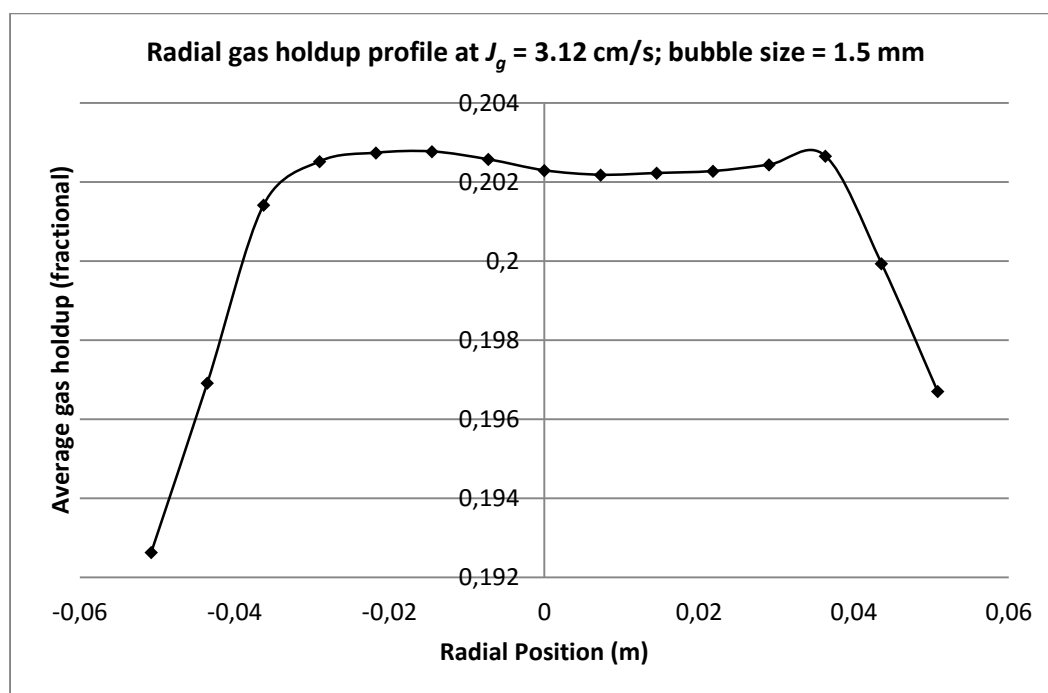
Figure 6.15: Radial gas holdup profile at $J_{g,max}$ (3.12 cm/s).
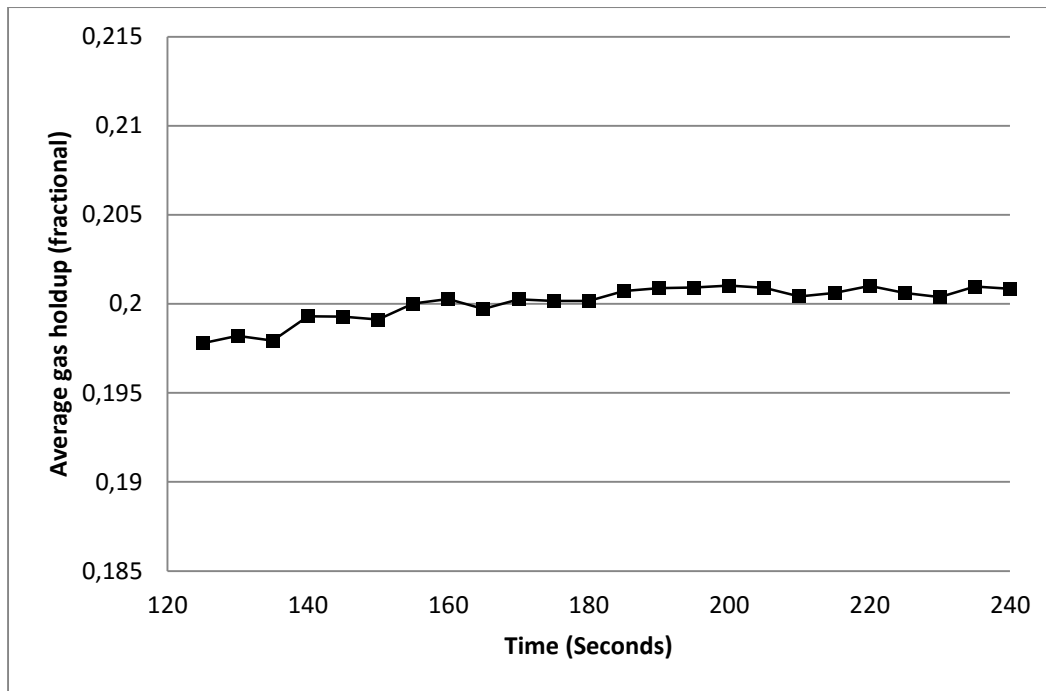
Figure 6.16: Gas holdup versus Time graph for J_g = 3.12 cm/s ($J_{g,max}$); bubble size = 1.5 mm.

In the churn-turbulent regime, steeper parabolic radial gas holdup profiles were observed from J_g = 5.28 cm/s as shown in Figure 6.17. On the other hand, very wide variations in Gas holdup versus Time at J_g = 5.28 cm/s (Figure 6.18) further confirm that the churn-turbulent flow regime was now prevailing in the column. The results from the CFD simulations for 1.5 mm bubble size are summarized in Table 6.4. The progression from bubbly flow conditions to churn-turbulent flow can be clearly seen in the Table.
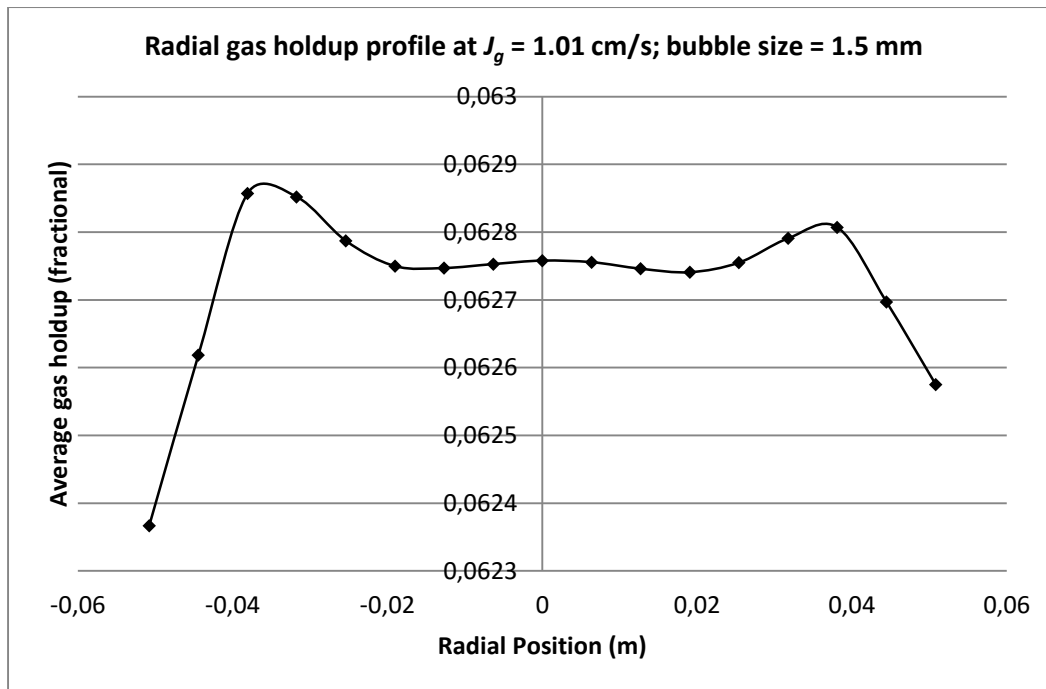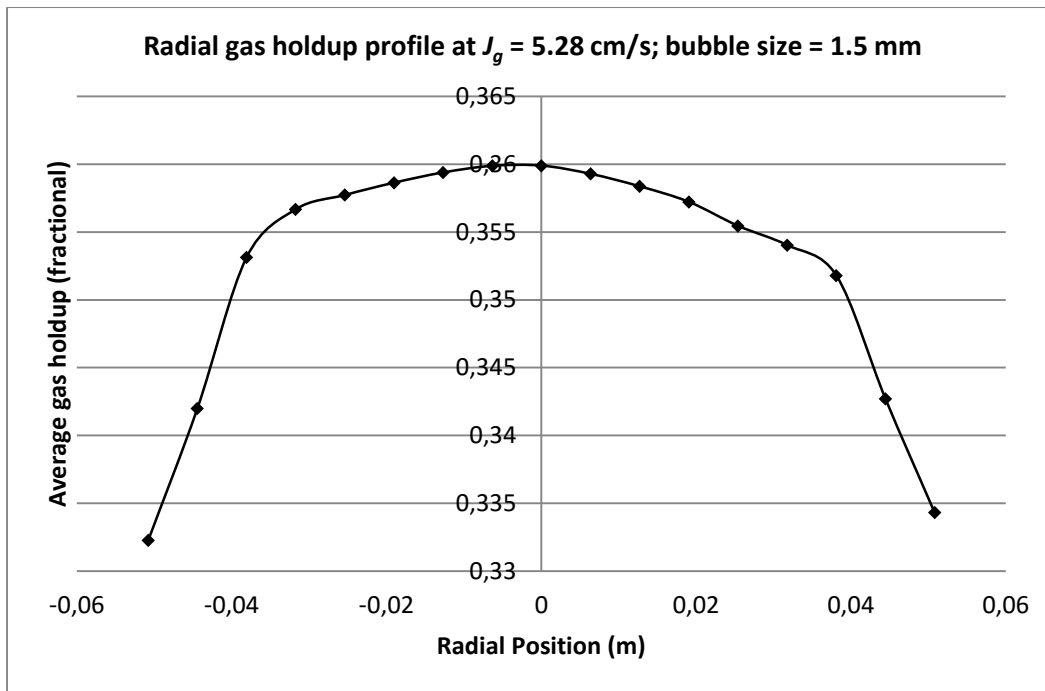
Figure 6.17: Radial gas holdup profile at J_g = 5.28 cm/s (bubble size = 1.5 mm).
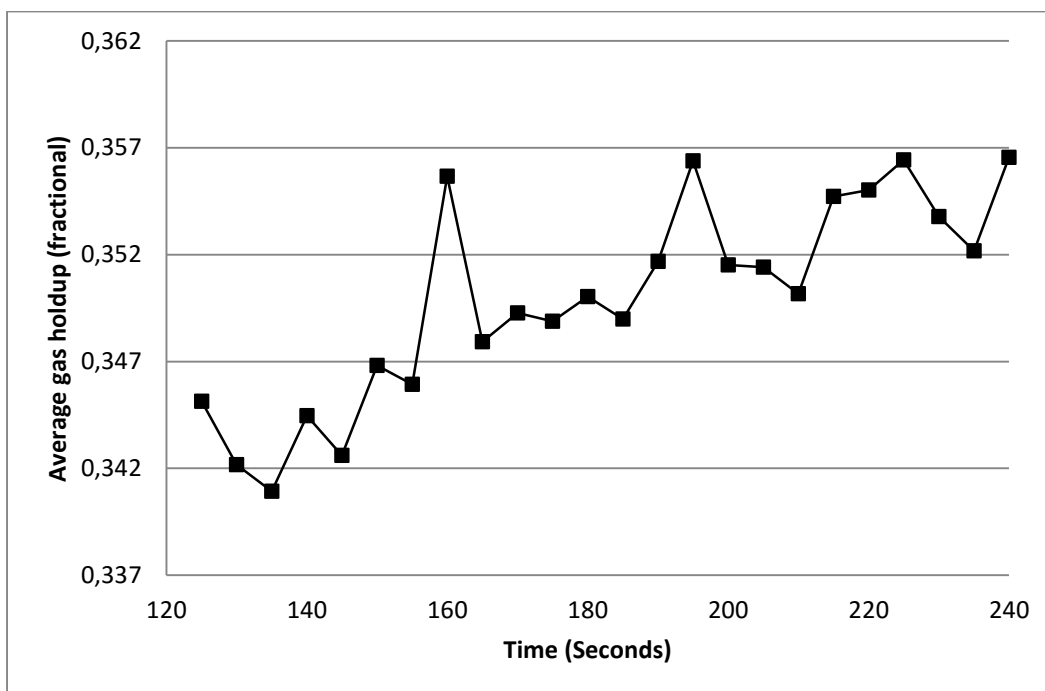
Figure 6.18: Gas holdup versus Time graph for J_g = 5.28 cm/s (bubble size = 1.5 mm).

130

Table 6.4: Summary of CFD simulation results for 1.5 mm bubble size.

J_g (cm/s)	Gas Holdup (%)	Radial gas holdup profile	Gas holdup versus time	Flow regime
1.01	6.27	Saddle shaped with three peaks	Constant	Bubbly flow
1.54	9.66	Saddle shaped with three peaks	-	Bubbly flow
1.84	11.60	Saddle shaped with two peaks	Very small variations	Bubbly flow
2.28	14.47	Saddle shaped with two peaks	Moderate fluctuations	Bubbly flow
2.73	17.46	Saddle shaped with two peaks	Moderate fluctuations	Bubbly flow
3.12	20.10	Flat intermediate between saddle and parabolic profiles	Moderate fluctuations	Bubbly flow (J_{gmax})
3.60	23.23	Flat profile	Larger fluctuations	Transition
4.03	26.27	Parabolic profile	Larger fluctuations	Transition
4.44	29.05	Parabolic	Large variations	Transition
5.28	35.51	Steep parabolic	Very large variations	Churn-turbulent flow

6.5.4   Liquid Velocity vectors

Two different flow patterns were observed depending on superficial gas velocity and bubble size. With increasing superficial gas velocity the well-known 'gulf-stream' circulation pattern in which the liquid rises in the centre of the column and descends near the column wall was observed. In contrast, an 'inverse' circulation flow pattern in which the liquid rises near the column wall but descends in the centre and adjacent to the wall occurred at lower superficial gas velocities. This is the first study to report such an inverse flow pattern in column flotation. However, similar flow reversals have been observed in experimental work on fluidized bed reactors [125].

The inverse circulation pattern has been theoretically investigated in bubble columns and is associated with fully developed saddle-shaped radial gas holdup profiles [51, 126]. In the present study, the inverse circulation pattern was observed at $J_g = 1.01$ cm/s and $J_g = 1.54$ cm/s for simulations with bubble size = 1.5 mm and superficial liquid velocity = 0.38 cm/s. Prominent saddle shaped gas holdup profiles with two distinct peaks near the walls of the column were also present under these conditions. The liquid velocity vector plots obtained from CFD simulations are presented in Figure 6.19 and Figure 6.20 for the two circulation patterns.

Clark et al. [126] have described the sequence of events that may initiate liquid circulation in bubble columns. In general, liquid circulation in bubble columns is initiated by density differences in the gas-liquid mixture depending on the prevailing radial gas holdup profile. If the concentration of air bubbles is higher in the central part of the column compared to the outer annular region, the mean mixture density will be lower near the centre of the column than in the outer annulus. The hydrostatic pressure head will therefore be higher in the outer annulus hence a radial pressure difference is set up inside the column. This will cause an inward radial movement of liquid and initiate liquid circulation. The inverse circulation pattern will occur if the concentration of bubbles is higher in the outer annular region as happens in the case of saddle-shaped gas holdup profiles.
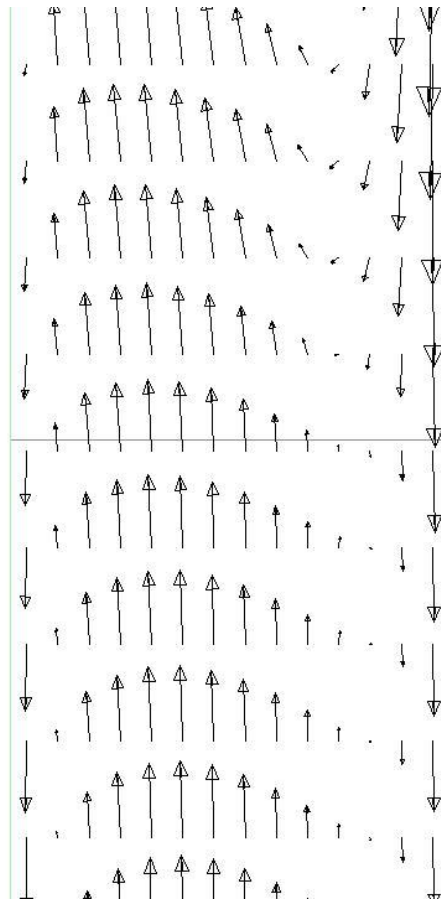
Figure 6.19: Liquid velocity vectors at mid-height in the collection zone for J_g = 4.03 cm/s (Gulf-stream circulation pattern).
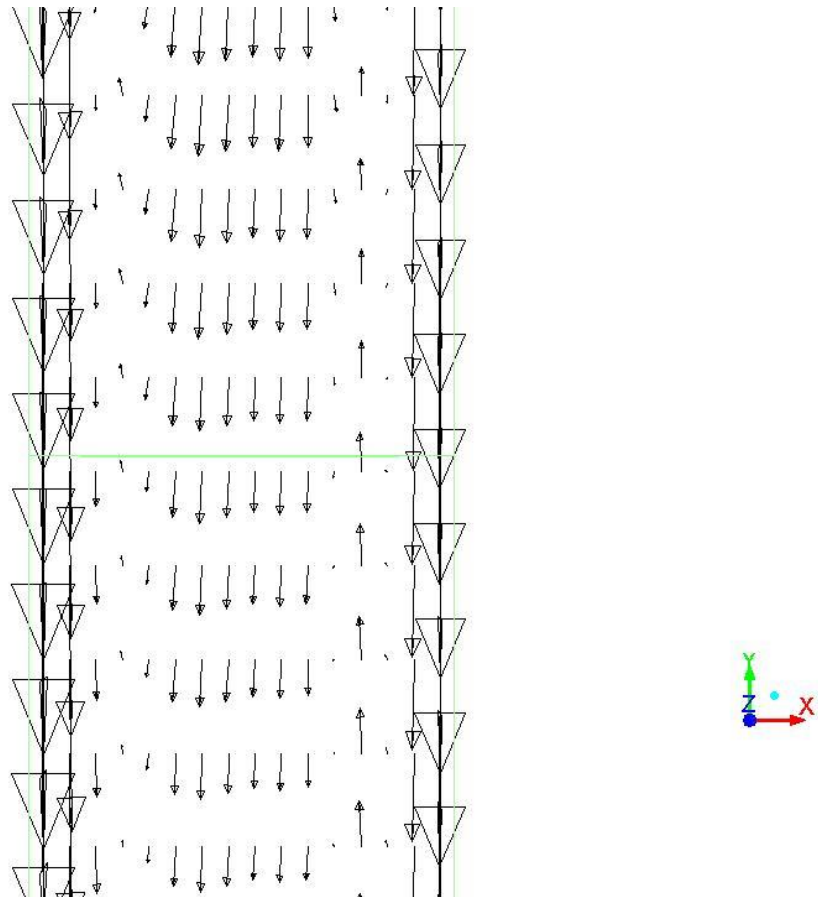
Figure 6.20: Liquid velocity vectors at mid-height in the collection zone for J_g = 1.54 cm/s (Inverse circulation pattern).

6.5.5   Effect of interphase turbulent dispersion on radial gas holdup profile

The CFD results discussed in this work so far did not consider the interphase turbulent dispersion forces in the simulations. However, turbulent dispersion, if taken into account, might have an influence on the shape of the simulated radial gas holdup profiles. This is because when turbulent dispersion forces are included in the simulations, turbulent fluctuations will cause additional dispersion of phases from regions of high volume fraction to regions of low volume fraction. In other words, the dispersed phase particles (or bubbles) will be moving from areas of high concentration to low concentration areas. Turbulent dispersion is therefore expected to have an effect on radial gas holdup profiles in the column.

The above concerns were addressed in this work by running some simulations in which the model of Lopez de Bertodano [127] was used to determine the effect of turbulent dispersion on the predicted radial gas holdup profile. The results are presented in Figure 6.21. Apart from a small reduction of the peak gas holdup values near the column wall, it can be seen that the turbulent dispersion did not have a significant influence on the shape of the gas holdup

134

profile. Therefore, neglecting turbulent dispersion forces does not adversely affect the CFD simulation results in this research.
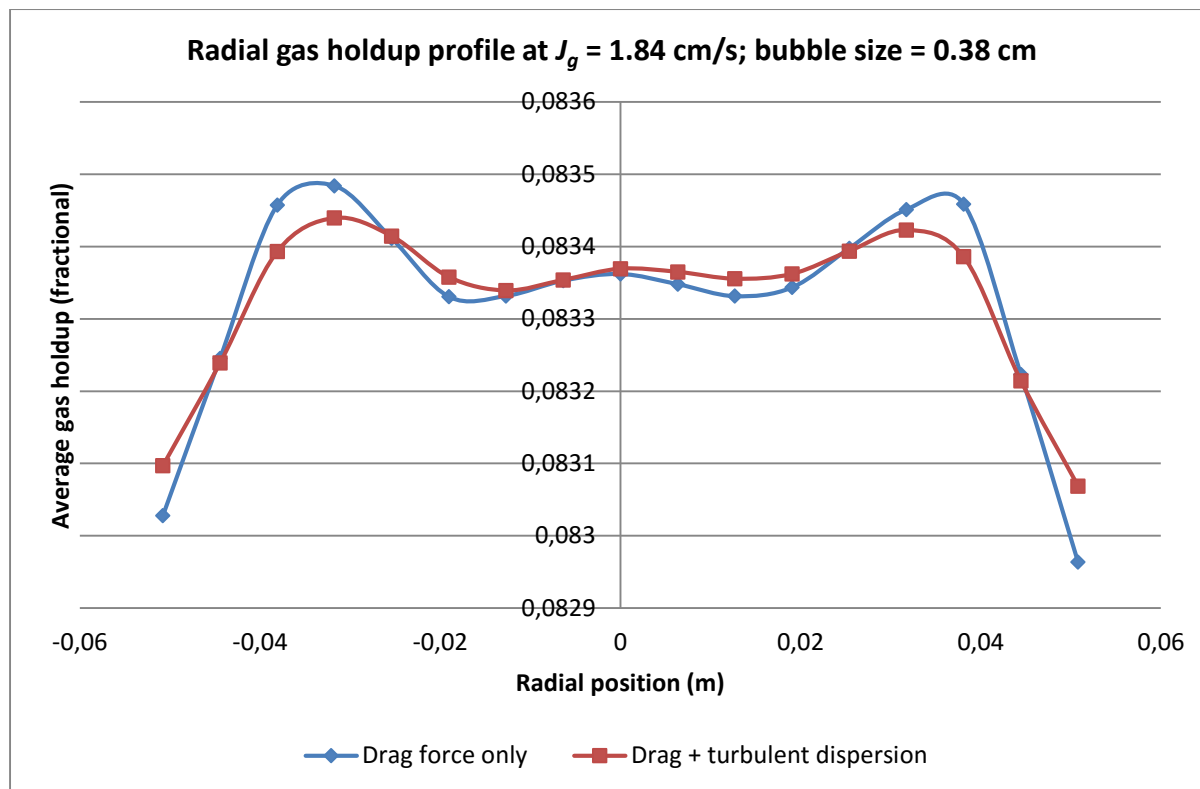
Figure 6.21: Effect of turbulent dispersion on the simulated radial gas holdup profile.

6.5.6 Applicability of radial gas holdup profiles for flow regime characterization in large diameter columns

The CFD simulation results presented in this work are for a 10 cm diameter column. The question that arises then is whether radial gas holdup profiles could also be used to distinguish the prevailing flow regime in large scale bubble/flotation columns. To answer this question, it is instructive to compare the results obtained in the present work against radial gas holdup profiles reported in the literature for large diameter columns.

Some previous studies exist in which conductivity methods were used to measure radial gas distribution in a 50 cm diameter laboratory column and a 91 cm diameter pilot column [114]. Different types of gas holdup profiles were reported depending on the superficial gas velocity. For the 50 cm column, the gas holdup profile was relatively flat at low superficial gas velocities while parabolic profiles were observed at higher superficial gas velocities. At a given height along the column, the highest gas holdup was found above the location of the spargers at low superficial gas velocity. However, this maximum shifted to the centre of the column as the superficial gas velocity increased.

For the pilot column (91 cm diameter), radial gas holdup profiles were studied for J_g 0.60, 0.90, and 2.15 cm/s. The gas holdup profiles at low superficial gas velocities (J_g 0.60 and 0.90 cm/s) had a'W' shape with highest values observed near the column wall. The gas holdup profiles then became saddle shaped as the superficial gas velocity increased to $J_g = 2.15$ cm/s.

From the above discussion, it is clear that there is a relationship between superficial gas velocity and the shape of the radial gas holdup profile in the column. This relationship can be employed to determine the prevailing flow regime in the column as has been demonstrated in the present research.

6.6   Conclusions

In this study, the evolution of the shape of the radial gas holdup profile in a pilot scale flotation column was studied using CFD to delineate the maximum gas velocity for loss of bubbly flow. With increasing superficial gas velocity, the gas holdup profile undergoes different stages which can be used to define the prevailing flow regime in the column. The different flow regimes were also verified by the intensity of the local variations of the gas holdup.

In the bubbly flow regime, saddle shaped and flat radial gas holdup profiles were obtained. These profiles were accompanied by little to moderate gas holdup variations in the column.

The transition regime was gradual and characterised by flat to parabolic gas holdup profiles. The parabolic profiles progressively became steeper as the superficial gas velocity increased. The corresponding Gas holdup versus Time graphs in the transition regime showed moderate to wide variations in gas holdup.

On the other hand, the churn-turbulent flow regime was distinguished by steep parabolic gas holdup profiles with very wide variations in Gas holdup versus Time.

For conditions relevant to column flotation, the maximum superficial gas velocity was determined for a column operating with an average bubble size of 1.5 mm and superficial liquid velocity equal to 0.38 cm/s. The maximum superficial gas velocity was found to be equal to 3.12 cm/s. The corresponding maximum gas holdup value was 20.1%.

Two possible flow patterns were revealed in the simulated column in this study, the gulf-stream circulation pattern and an inverse circulation pattern. The latter was observed only in the presence of fully developed saddle shaped radial gas holdup profiles.

Chapter 7   Conclusions and Recommendations

7.1   Research summary

The purpose of this research was to apply Computational Fluid Dynamics (CFD) to study gas dispersion and mixing in industrial and pilot scale flotation columns. These two themes had not been adequately addressed by previous CFD literature pertaining to column flotation. The term gas dispersion combines three variables in minerals flotation: superficial gas velocity, bubble size, and gas holdup. In addition, the bubble surface area flux, a fourth parameter derived from the three, is used to characterize the flotation process. On the other hand, the mixing processes in the column also affect its performance in terms of grade and recovery.

The CFD simulations in this research were performed using the Eulerian-Eulerian multiphase model in which the different phases are considered separately as interpenetrating continua. The Eulerian-Eulerian approach was selected among other models considering its lower computational cost compared with other models such as the Eulerian-Lagrangian. These other models are limited to simulating systems in which the dispersed phase volume fractions are considerably low (less than 10% for Eulerian-Lagrangian model). The interaction between the phases in the Eulerian-Eulerian model was accounted for by means of the drag force only while other forces such as virtual mass and lift force were assumed to be negligible based on literature evidence.

In the CFD simulations, the flow variables are calculated by solving the Reynolds averaged momentum and continuity equations. In addition, the turbulence model is solved in order to account for the effects of turbulence fluctuations on the mean flow. The turbulence in the continuous liquid phase in the columns was modelled using the Realizable k-ϵ turbulence model. On the other hand, previous CFD models of column flotation in the literature have used the Standard k-ϵ model while others have assumed laminar flow conditions. It would therefore be necessary to investigate the effect of using different turbulence models on the simulated flow variables. However, this aspect was not studied in the present research in the context of column flotation due to lack of experimental data against which to compare the models.

An important aspect of the research involves the definition of a suitable computational domain for the flotation column CFD model. Due to the differences in flow patterns and turbulence characteristics between the collection zone and the froth zone, it still remains a

challenge to formulate CFD simulations that combine the two zones. The focus of this research was therefore the collection zone of the column while the froth phase was not included in the model.

Further simplifications were achieved in this research by excluding the spargers from the model geometry. Instead, the air bubbles were introduced into the column over the entire column cross section at the bottom of the vessel. Considering the uniform gas holdup distributions that are achievable with flotation column spargers, introducing air bubbles over the entire column section is a reasonable albeit simplified representation of the actual sparging mechanism.

The formulated CFD methodology was subsequently used to study the following three aspects of column flotation:

- Gas holdup and its axial variation along the column
- Mixing characteristics of the collection zone, and
- Flow regime transition in the column

The main conclusions of the research are summarized in the next section within the context of these three issues. The axial gas holdup variation in the column was achieved by imposing compressibility effects on the bubbles using the Ideal Gas law. The actual hydrostatic expansion of the bubbles was not modelled. The CFD model therefore accounts for changes in bubble density in response to the local hydrostatic pressure value while the bubble size remains constant throughout the column. However, the results obtained compared favourably with experimental data.

The mixing characteristics of the liquid phase (water) in industrial flotation columns were simulated using the Species model available in the Ansys Fluent CFD solver. On the other hand, the particle (solids) mean residence time was determined scalar transport equation that computes the age of particles to give their spatial age distribution in the column. The mean residence time is then obtained as the area weighted average age of the particles at the outlet. This method has been used to predict mean residence time in the chemical engineering literature. However, this research is the first to apply the method for column flotation studies. An advantage of using this particle age equation is that it has less computational cost compared to other methods such as Lagrangian particle tracking. In addition, this method

provides further insights into the effects of liquid recirculation on particle residence time in the column.

The final part of this research investigated flow regime transition in a pilot scale column cell. The well-known method in which the superficial gas velocity is plotted against gas holdup was used to predict flow regime transition for a system with water and air only (without frother). However, the method could not be applied to model a system with frother due to the unavailability of methods to calculate the mean bubble sizes that could be used in the simulations for the column in the churn-turbulent regime. The effect of superficial gas velocity on radial gas holdup profiles was therefore studied in order to distinguish the flow regime on the basis of the gas holdup profiles under conditions relevant to column flotation. A CFD model coupled with a Bubble Population Balance model might be more suitable for simulating columns in the churn-turbulent regime because bubble size distributions can then be incorporated in the model.

7.2 Conclusions

7.2.1 Gas holdup and its distribution in the column

Gas holdup was observed to increase with height along the column as reported in the literature. The gas holdup increased by more than 100% from the bottom to the top part of the column over a height of 13.5 m. An axial profile of bubble velocity was observed in which bubble velocity increased rapidly to a maximum value and then began to decrease with height to a terminal velocity. This study attributes the axial decrease in bubble velocity to a possible increase in drag force resulting from increasing gas holdup along the column height. It is also argued that the decrease in bubble velocity will further increase the gas holdup profile due to increased bubble residence time. This study therefore proposes that the axial increase in gas holdup maybe inter-related with the axial bubble velocity reduction observed along the column axis.

7.2.2 Mixing characteristics of the collection zone in column flotation

In terms of mixing in the column, the formulated CFD model was used to simulate the liquid RTDs in order to determine the mixing parameters (the vessel dispersion number and the mean residence time) for the column. The model was capable of predicting mixing parameters comparable with experimental data for both square and cylindrical industrial columns. This research further investigated the effect of liquid circulation on the particle residence time. It was found that the spatial age distribution of the particles in the column is

related to the prevailing liquid circulation flow pattern. The effects of solids particle size and bubble size on the liquid dispersion in the column were also studied. The CFD simulation results showed that the liquid dispersion is affected by particle size and bubble size. Increasing the particle size of the solids resulted in a decrease in the liquid vessel dispersion number. On the other hand, a decrease in bubble size resulted in an increase in the liquid vessel dispersion number.

7.2.3   Flow regime identification using CFD

Flow regime transition was identified for a water and air system (without frother) using gas holdup versus superficial gas velocity graphs derived from CFD simulations. Radial gas holdup profiles were then studied for the delineated flow regimes in order to determine whether gas holdup profiles could be used to indicate the prevailing flow pattern in the column. In this regard, the bubbly flow regime can be characterized by three distinct radial gas holdup profiles as follows:

- saddle shaped profiles with three peaks at lower superficial gas velocities
- Saddle shaped profiles with two near wall peaks and a central minimum as the superficial gas velocity increases
- Flat gas holdup profiles just before transition towards churn turbulent flow. In some cases the profiles appear to have intermediate features between saddle and parabolic gas holdup profiles

The transition regime was characterized by flat profiles that evolved into parabolic profiles as the superficial gas velocity increased. The transition regime was therefore seen to be gradual which would make it difficult to use radial gas holdup profiles to determine the maximum gas velocity in column flotation. However, parabolic radial gas holdup profiles would certainly indicate that the column is operating under churn turbulent flow conditions.

The prevailing flow patterns in the column were further confirmed using gas holdup versus time graphs. The two extreme conditions of bubbly flow and churn turbulent flow were easier to distinguish. In this case, the gas holdup remained constant in the bubbly flow regime while churn turbulent flow was characterized by wide variations in the gas holdup. The transition regime was again gradual in which the gas holdup versus time graphs show moderate to wide fluctuations as the superficial gas velocity increases.

Another important observation emerging from this research was that different radial gas holdup profiles could result in opposite liquid flow patterns. For example, a liquid circulation pattern with upward flow in the centre and downward flow near the column walls was always present when the gas holdup profile is parabolic. On the other hand, an inverse flow pattern was observed in which the liquid rises near the column wall but descends in the centre and adjacent to the wall. This profile was accompanied by corresponding saddle shaped gas holdup profiles.

7.3   Recommendations

The following recommendations can be considered for future research:

- For the work on gas holdup and its distribution in the column, it is recommended for future research to incorporate the actual bubble expansion as a function of height or hydrostatic pressure inside the column. This aspect was neglected in the present research in order to achieve a simplified CFD model and also to reduce the computational effort required to perform the simulations.

- The present research has investigated the relationship between radial gas holdup profiles and the prevailing flow pattern in a 0.1 m diameter column. It would be important in future studies to find out whether radial gas holdup profiles can be used to distinguish flow regimes in industrial flotation columns. Radial gas holdup profiles should therefore be studied in larger columns in the context of flow regime characterization.

- The CFD simulations in the present study assumed a constant average bubble size for all the columns. However, for the churn turbulent regime, a bubble size distribution exists which could have an effect on the hydrodynamics of the column. On the other hand, a bubble population balance model can be used to predict bubble size distributions in the column. It is therefore recommended for future research to apply CFD models coupled with bubble population balance models when simulating different flow regimes in the column.

- Some of the CFD models in the literature have used the standard k-ϵ model to account for turbulence while others have assumed laminar conditions. It would be helpful to compare the different turbulence models in terms of their prediction of flow variables in future studies.

References

References

1. Wheeler D. In: Column flotation-the original column. Proceedings of 2nd latin american congress in froth flotation (SH castro, J. alvarez eds.); ; 1985. p. 19-23.

2. Finch JA, Dobby GS. Column flotation. Oxford, England: Pergamon Press; 1990.

3. Finch J, Hardie C. An example of innovation from the waste management industry: Deinking flotation cells. Minerals Eng. 1999;12(5):467-75.

4. Hernandez H, Gomez C, Finch J. Gas dispersion and de-inking in a flotation column. Minerals Eng. 2003;16(8):739-44.

5. Finch J, Xiao J, Hardie C, Gomez C. Gas dispersion properties: Bubble surface area flux and gas holdup. Minerals Eng. 2000;13(4):365-72.

6. Matiolo E, Testa F, Yianatos J, Rubio J. On the gas dispersion measurements in the collection zone of flotation columns. Int J Miner Process. 2011;99(1):78-83.

7. Ityokumbul M. A new modelling approach to flotation column desing. Minerals Eng. 1992;5(6):685-93.

8. Yianatos J, Finch J. Gas holdup versus gas rate in the bubbly regime. Int J Miner Process. 1990;29(1):141-6.

9. Mavros P. Mixing in flotation columns. part I: Axial dispersion modelling. Minerals Eng. 1993;6(5):465-78.

10. Mavros P, Daniilidou A. Mixing in flotation columns. part II. liquid-phase residence time distributions studies. Minerals Eng. 1993;6(7):707-19.

11. Deng H, Mehta R, Warren G. Numerical modeling of flows in flotation columns. Int J Miner Process. 1996;48(1):61-72.

12. Koh P, Schwarz M, Zhu Y, Bourke P, Peaker R, Franzidis J. In: Development of CFD models of mineral flotation cells. Third international conference on computational fluid dynamics in the minerals and process industries, melbourne, australia; ; 2003. p. 171-5.

13. Koh P, Schwarz M. In: CFD models of microcel and jameson flotation cells. Seventh international conference on CFD in the minerals and process industries, CSIRO, melbourne, australia; ; 2009.

14. Chakraborty D, Guha M, Banerjee P. CFD simulation on influence of superficial gas velocity, column size, sparger arrangement, and taper angle on hydrodynamics of the column flotation cell. Chem Eng Commun. 2009;196(9):1102-16.

15. Xia Y, Peng F, Wolfe E. CFD simulation of alleviation of fluid back mixing by baffles in bubble column. Minerals Eng. 2006;19(9):925-37.

16. Nadeem M, Ahmed J, Chughtai IR, Ullah A. CFD-based estimation of collision probabilities between fine particles and bubbles having intermediate reynolds number. Nucleus. 2009;46(3):153-9.

17. Rehman A, Nadeem M, Zaman M, Nadeem B. Effect of various baffle designs on air holdup and mixing in a flotation column using CFD. . 2011.

18. Gomez C, Uribe-Salas A, Finch J, Huls B. Gas holdup measurement in flotation columns using electrical conductivity. Can Metall Q. 1991;30(4):201-5.

19. Xu M, Uribe-Salas A, Finch J, Gomez C. In: Gas rate limitation in column flotation. Processing of complex ores: Proceedings of the international symposium on processing of complex ores, halifax, august 20-24, 1989; Elsevier; 1989. p. 397.

20. Xu M, Finch J, Uribe-Salas A. Maximum gas and bubble surface rates in flotation columns. Int J Miner Process. 1991;32(3):233-50.

21. Langberg D, Jameson G. The coexistence of the froth and liquid phases in a flotation column. Chemical engineering science. 1992;47(17):4345-55.

22. Schallenberg J, Enß JH, Hempel DC. The important role of local dispersed phase hold-ups for the calculation of three-phase bubble columns. Chemical engineering science. 2005;60(22):6027-33.

23. Cilliers J. In: Understanding froth behaviour with CFD. 5th international conference on CFD in the process industries CSIRO, melbourne; ; 2006.

24. Dobby GS. A fundamental flotation model and flotation column scale-up [dissertation]. Montreal, Canada: McGill University; 1985.

25. Dobby G, Finch J. Column flotation: A selected review, part II. Minerals Eng. 1991;4(7):911-23.

26. Harach PL, Redfearn MA, Waites DB, inventors; Cominco Ltd. V, Canada, assignee. United States patent 4,911,826. 1990 .

27. Xu M, Finch J, Huls B. Measurement of radial gas holdup profiles in a flotation column. Int J Miner Process. 1992;36(3):229-44.

28. Paleari F, Xu M, Finch J. Radial gas holdup profiles: The influence of sparger systems. Minerals and Metallurgical Processing. 1994;11(2):111-7.

29. Yianatos J, Bergh L, Sepulveda C, Núñez R. Measurement of axial pressure profiles in large-size industrial flotation columns. Minerals Eng. 1995;8(1):101-9.

30. Zhou Z, Egiebor N. Prediction of axial gas holdup profiles in flotation columns. Minerals Eng. 1993;6(3):307-12.

31. Sam A, Gomez C, Finch J. Axial velocity profiles of single bubbles in water/frother solutions. Int J Miner Process. 1996;47(3):177-96.

32. Michele V, Hempel DC. Liquid flow and phase holdup—measurement and CFD modeling for two-and three-phase bubble columns. Chemical engineering science. 2002;57(11):1899-908.

33. Baléo J, Le Cloirec P. Validating a prediction method of mean residence time spatial distributions. AIChE J. 2000;46(4):675-83.

34. Baléo J, Humeau P, Le Cloirec P. Numerical and experimental hydrodynamic studies of a lagoon pilot. Water Res. 2001;35(9):2268-76.

35. Ghirelli F, Leckner B. Transport equation for the local residence time of a fluid. Chemical engineering science. 2004;59(3):513-23.

36. Liu M, Tilton J. Spatial distributions of mean age and higher moments in steady continuous flows. AIChE J. 2010;56(10):2561-72.

146

37. Simcik M, Ruzicka M, Mota A, Teixeira J. Smart RTD for multiphase flow systems. Chem Eng Res Design. 2012;90(11):1739-49.

38. Ityokumbul M. Maximum gas velocity in column flotation. Minerals Eng. 1993;6(12):1279-86.

39. Dobby G, Finch J. Particle collection in columns—gas rate and bubble size effects. Can Metall Q. 1986;25(1):9-13.

40. Finch JA, Dobby GS. Column flotation: A selected review. part I. Int J Miner Process. 1991;33(1):343-54.

41. Leichtle GF. Analysis of bubble generating devices in a deinking column [dissertation]. McGill University; 1998.

42. López-Saucedo F, Uribe-Salas A, Pérez-Garibay R, Magallanes-Hernández L. Gas dispersion in column flotation and its effect on recovery and grade. Can Metall Q. 2012;51(2):111-7.

43. Massinaei M, Kolahdoozan M, Noaparast M, Oliazadeh M, Yianatos J, Shamsadini R, et al. Hydrodynamic and kinetic characterization of industrial columns in rougher circuit. Minerals Eng. 2009;22(4):357-65.

44. Dobby G, Amelunxen R, Finch J. In: Column flotation: Some plant experience and model development. Symposium on automation for mineral development; ; 1985. p. 9-11.

45. Gomez C, Uribe-Salas A, Finch J, Huls B. Axial gas holdup profiles in the collection zones of flotation columns. Minerals and Metallurgical Processing. 1995;12(1):16-23.

46. Serizawa A, Kataoka I, Michiyoshi I. Turbulence structure of air-water bubbly flow—II. local properties. Int J Multiphase Flow. 1975;2(3):235-46.

47. Bennett M, Luke S, Jia X, West R, Williams R. In: Analysis and flow regime identification of bubble column dynamics. 1st world congress on industrial process tomography, buxton, greater manchester; ; 1999. p. 14-7.

48. Hills J. Radial non-uniformity of velocity and voidage in a bubble column. Trans.Inst.Chem.Eng. 1974;52(1):1-9.

49. Freedman W, Davidson J. Hold-up and liquid circulation in bubble columns. Transactions of the Institution of Chemical Engineers and the Chemical Engineer. 1969;47(8):T251.

50. Devanathan N, Moslemian D, Dudukovic M. Flow mapping in bubble columns using CARPT. Chemical Engineering Science. 1990;45(8):2285-91.

51. Clark N, Atkinson C, Flemmer R. Turbulent circulation in bubble columns. AIChE J. 1987;33(3):515-8.

52. Dobby G, Yianatos J, Finch J. Estimation of bubble diameter in flotation columns from drift flux analysis. Can Metall Q. 1988;27(2):85-90.

53. Yianatos J, Finch J, Dobby G, Xu M. Bubble size estimation in a bubble swarm. J Colloid Interface Sci. 1988;126(1):37-44.

54. Banisi S, Finch JA. Technical note reconciliation of bubble size estimation methods using drift flux analysis. Minerals Eng. 1994 12;7(12):1555-9.

55. López-Saucedo F, Uribe-Salas A, Pérez-Garibay R, Magallanes-Hernández L, Lara-Valenzuela C. Modelling of bubble size in industrial flotation columns. Can Metall Q. 2011;50(2):95-101.

56. Luttrell G, Mankosa M, Yoon R. In: Design and scale-up criteria for column flotation. XVIII international mineral processing congress; ; 1993. p. 785-91.

57. Rice R, Oliver A, Newman J, Wiles R. Reduced dispersion using baffles in column flotation. Powder Technol. 1974;10(4):201-10.

58. Dobby G, Finch J. Mixing characteristics of industrial flotation columns. Chemical Engineering Science. 1985;40(7):1061-8.

59. Laplante A, Yianatos J, Finch J. On the mixing characteristics of the collection zone in flotation columns. Column flotation. 1988;88:69-80.

60. Mavros P, Lazaridis N, Matis K. A study and modelling of liquid-phase mixing in a flotation column. Int J Miner Process. 1989;26(1):1-16.

61. Goodall C, O'Connor C. Residence time distribution studies in a flotation column. part 1: The modelling of residence time distributions in a laboratory column flotation cell. Int J Miner Process. 1991;31(1):97-113.

62. Goodall C, O'Connor C. Residence time distribution studies in a flotation column. part 2: The relationship between solids residence time distribution and metallurgical performance. Int J Miner Process. 1992;36(3):219-28.

63. Mankosa M, Luttrell G, Adel G, Yoon R. A study of axial mixing in column flotation. Int J Miner Process. 1992;35(1):51-64.

64. Xu M, Finch J. Solids mixing in the collection zone of flotation columns. Minerals Eng. 1992;5(9):1029-39.

65. Yianatos JB, Bergh LG. RTD studies in an industrial flotation column: Use of the radioactive tracer technique. Int J Miner Process. 1992;36(1):81-91.

66. Yianatos JB, Bergh LG, Díaz F, Rodríguez J. Mixing characteristics of industrial flotation equipment. Chemical Engineering Science. 2005;60(8):2273-82.

67. Massinaei M, Kolahdoozan M, Noaparast M, Oliazadeh M, Sahafipour M, Finch J. Mixing characteristics of industrial columns in rougher circuit. Minerals Eng. 2007;20(15):1360-7.

68. Schwarz M. Flow simulation in minerals engineering. Minerals Eng. 1991;4(7):717-32.

69. Napier-Munn TJ, Lynch A. The modelling and computer simulation of mineral treatment processes—current status and future trends. Minerals Eng. 1992;5(2):143-67.

70. Anderson JD. Computational fluid dynamics. McGraw-Hill; 1995.

71. Versteeg HK, Malalasekera W. An introduction to computational fluid dynamics: The finite volume method. Prentice Hall; 2007.

72. Andersson B, Andersson R, Håkansson L, Mortensen M, Sudiyo R. Computational fluid dynamics for engineers. Cambridge University Press; 2011.

73. Yianatos J, Bergh L, Sepulveda C, Núñez R. Measurement of axial pressure profiles in large-size industrial flotation columns. Minerals Eng. 1995;8(1):101-9.

74. Sato Y, Sekoguchi K. Liquid velocity distribution in two-phase bubble flow. Int J Multiphase Flow. 1975;2(1):79-95.

75. Sarhan A, Naser J, Brooks G. CFD simulation on influence of suspended solid particles on bubbles' coalescence rate in flotation cell. Int J Miner Process. 2016;146:54-64.

76. Brito-Parada P, Neethling S, Cilliers J. The advantages of using mesh adaptivity when modelling the drainage of liquid in froths. Minerals Eng. 2012;33:80-6.

77. Sasic S, Sibaki EK, Ström H. Direct numerical simulation of a hydrodynamic interaction between settling particles and rising microbubbles. European Journal of Mechanics-B/Fluids. 2014;43:65-75.

78. Andersson B, Andersson R, Håkansson L, Mortensen M, Sudiyo R, van Wachem B. Computational fluid dynamics for engineers. Cambridge University Press; 2011.

79. Ranade VV. Computational flow modeling for chemical reactor engineering. Academic press; 2001.

80. Delnoij E, Kuipers JAM, van Swaaij WPM. Computational fluid dynamics applied to gas-liquid contactors. Chemical Engineering Science. 1997 11;52(21–22):3623-38.

81. Zhang D. Eulerian modeling of reactive gas-liquid flow in a bubble column. University of Twente; 2007.

82. Akhtar A. Two-fluid eulerian simulation of bubble column reactors with distributors. J Chem Eng Japan. 2006;39(8):831-41.

83. Chen P, Sanyal J, Dudukovic M. CFD modeling of bubble columns flows: Implementation of population balance. Chemical Engineering Science. 2004;59(22):5201-7.

84. Chen P, Duduković M, Sanyal J. Three-dimensional simulation of bubble column flows with bubble coalescence and breakup. AIChE J. 2005;51(3):696-712.

85. Chen J, Yang N, Ge W, Li J. Computational fluid dynamics simulation of regime transition in bubble columns incorporating the dual-bubble-size model. Ind Eng Chem Res. 2009;48(17):8172-9.

86. Sahbaz O, Ercetin U, Oteyaka B. Determination of turbulence and upper size limit in jameson flotation cell by the use of computational fluid dynamic modelling. Physicochemical Problems of Mineral Processing. 2012;49(2):535-46.

87. Yan X, Liu J, Cao Y, Wang L. A single-phase turbulent flow numerical simulation of a cyclonic-static micro bubble flotation column. International Journal of Mining Science and Technology. 2012;22(1):95-100.

88. Mavros P, Daniilidou A, Papatsiotsou F. Internal recirculation and mixing in flotation columns. Trans IChemE. 1995;73(Part A).

89. Karthik T, Durst F. Turbulence models and their applications. Department of Mechanical Engineering, Indian Institute of Technology, Madras, India. 2011.

90. Launder BE, Spalding D. The numerical computation of turbulent flows. Comput Methods Appl Mech Eng. 1974;3(2):269-89.

91. Laborde-Boutet C, Larachi F, Dromard N, Delsart O, Schweich D. CFD simulation of bubble column flows: Investigations on turbulence models in RANS approach. Chemical Engineering Science. 2009;64(21):4399-413.

92. Pfleger D, Gomes S, Gilbert N, Wagner H. Hydrodynamic simulations of laboratory scale bubble columns fundamental studies of the Eulerian–Eulerian modelling approach. Chemical Engineering Science. 1999;54(21):5091-9.

93. Pfleger D, Becker S. Modelling and simulation of the dynamic flow behaviour in a bubble column. Chemical Engineering Science. 2001 2;56(4):1737-47.

94. NI K. Multiphase flow dynamics, vol. 2 thermal and mechanical interactions. 2nd ed. Berlin, Germany: Springer; 2005.

95. Schiller L, Naumann A. A drag coefficient correlation. Vdi Zeitung. 1935;77:318-20.

96. Morsi S, Alexander A. An investigation of particle trajectories in two-phase flow systems. J Fluid Mech. 1972;55(2):193-208.

97. Zhou Z, Egiebor N. Technical note a gas-liquid drift-flux model for flotation columns. Minerals Eng. 1993;6(2):199-205.

98. Yianatos J, Bergh L, Durán O, Diaz F, Heresi N. Measurement of residence time distribution of the gas phase in flotation columns. Minerals Eng. 1994;7(2):333-44.

99. Prince MJ, Blanch HW. Bubble coalescence and break-up in air-sparged bubble columns. AIChE J. 1990;36(10):1485-99.

100. López-Saucedo F, Uribe-Salas A, Pérez-Garibay R, Magallanes-Hernández L, Lara-Valenzuela C. Modelling of bubble size in industrial flotation columns. Can Metall Q. 2011;50(2):95-101.

101. Nicklin D. Two-phase bubble flow. Chemical engineering science. 1962;17(9):693-702.

102. Zhou Z, Egiebor N, Plitt L. Frother effects on bubble motion in a swarm. Can Metall Q. 1993;32(2):89-96.

103. Mills P, Yianatos J, O'Connor C. The mixing characteristics of solid and liquid phases in a flotation column. Minerals Eng. 1992;5(10):1195-205.

104. Yianatos JB, Bergh LG, Díaz F, Rodríguez J. Mixing characteristics of industrial flotation equipment. Chemical Engineering Science. 2005;60(8):2273-82.

105. Ityokumbul M. A new modelling approach to flotation column desing. Minerals Eng. 1992;5(6):685-93.

106. Mills P, O'Connor C. The modelling of liquid and solids mixing in a flotation column. Minerals Eng. 1990;3(6):567-76.

107. Levenspiel O. Chemical reaction engineering. Wiley Eastern Limited; 1972.

108. Chen J, Gupta P, Degaleesan S, Al-Dahhan MH, Duduković MP, Toseland BA. Gas holdup distributions in large-diameter bubble columns measured by computed tomography. Flow Meas Instrum. 1998;9(2):91-101.

109. Delnoij E. Fluid dynamics of gas-liquid bubble columns [dissertation]. Universiteit Twente; 1999.

110. Wen C, Yu Y. In: Mechanics of fluidization. Chem. eng. prog. symp. ser. ; 1966. p. 100-11.

111. Ring T, Wang B, Sang-Choi B, Dhanasekharan K. Predicting residence time distribution with FLUENT. Fluent News. 2004;31.

112. Streng M, Wünsch O. Numerical simulation of the residence time distribution in flotation cells. PAMM. 2007;7(1):4090003-4.

113. Yianatos J, Díaz F. Hydrodynamic characterization of industrial flotation machines using radioisotopes. INTECH Open Access Publisher; 2011.

114. Xu M. Radial gas holdup profile and mixing in the collection zone of flotation columns. 1990.

115. Finch JA, Dobby GS. Column flotation: A selected review. part I. Int J Miner Process. 1991;33(1):343-54.

116. Kobayasi K, Iida Y, Kanegae N. Distribution of local void fraction of air-water two-phase flow in a vertical channel. Bulletin of JSME. 1970;13(62):1005-12.

117. Shen G. Bubble swarm velocities in a flotation column [dissertation]. Montreal, Canada: McGill University; 1994.

118. Finch JA, Dobby GS. Column flotation. Oxford: Oxford : Pergamon; 1990.

119. Mecklenburg MM. Hydrodynamic study of a downwards concurrent bubble column [dissertation]. Montreal, Canada: McGill University; 1992.

120. Summers AJ. A study of the operating variables of the jameson cell [dissertation]. Montreal, Canada: McGill University; 1995.

121. Lockett M, Kirkpatrick R. Ideal bubbly flow and actual flow in bubble columns. Transactions of the Institution of Chemical Engineers. 1975;53:267-73.

122. Ruzicka M, Zahradnık J, Drahoš J, Thomas N. Homogeneous–heterogeneous regime transition in bubble columns. Chemical Engineering Science. 2001;56(15):4609-26.

123. Vial C, Poncin S, Wild G, Midoux N. A simple method for regime identification and flow characterisation in bubble columns and airlift reactors. Chemical Engineering and Processing: Process Intensification. 2001;40(2):135-51.

124. Shaikh A, Al-Dahhan MH. A review on flow regime transition in bubble columns. International Journal of Chemical Reactor Engineering. 2007;5(1).

125. Lin J, Chen M, Chao B. A novel radioactive particle tracking facility for measurement of solids motion in gas fluidized beds. AIChE J. 1985;31(3):465-73.

126. Clark N, Van Egmond J, Nebiolo E. The drift-flux model applied to bubble columns and low velocity flows. Int J Multiphase Flow. 1990;16(2):261-79.

127. de Bertodano, Martin Aurelio Lopez. Turbulent bubbly two-phase flow in a triangular duct. 1992.

Appendix 1: Mass and momentum source terms for the simulations in Chapter 4 .

This Appendix presents the mass and momentum source terms calculated from superficial gas velocities using equations *(3.1)* and *(3.2)*as described in Chapter 3.

Superficial Gas Velocity (cm/s)	Superficial Gas Velocity (m/s)	Mass Source term (kg/ m^3 - s)	Momentum Source term (N/ m^3)
0.72	0.0072	8.82E-01	6.35E-03
0.93	0.0093	1.14E+00	1.06E-02
1.22	0.0122	1.49E+00	1.82E-02
1.51	0.0151	1.85E+00	2.79E-02
1.67	0.0167	2.05E+00	3.42E-02

Appendix 2: User defined function for the source term used in particle age transport equation

This Appendix outlines the user defined function (UDF) that was used to calculate the source term in the particle age user defined scalar (UDS) equation described in Chapter 5, equation (5.18)).

```
#include "udf.h"

DEFINE_SOURCE(my_scalar_source,c,t,ds,eqn)

{

real source;

real rho_p = C_R(c,t);

real vof_p = C_VOF(c,t);

source = rho_p*vof_p;

ds[eqn] = 0;

return source;

}
```

Appendix 3: Mass and momentum source terms for the simulations in Chapter 6.

This Appendix presents the mass and momentum source terms calculated from superficial gas velocities using equations *(3.1)* and *(3.2)* as described in Chapter 3.

Superficial Gas Velocity (cm/s)	Superficial Gas Velocity (m/s)	Mass Source term (kg/ m^3 - s)	Momentum Source term (N/ m^3)
1.01	0.0101	1.24E+00	1.25E-02
1.54	0.0154	1.89E+00	2.91E-02
1.84	0.0184	2.25E+00	4.15E-02
2.28	0.0228	2.79E+00	6.37E-02
2.73	0.0273	3.34E+00	9.13E-02
3.12	0.0312	3.82E+00	1.19E-01
3.6	0.036	4.41E+00	1.59E-01
4.03	0.0403	4.94E+00	1.99E-01
4.44	0.0444	5.44E+00	2.41E-01
5.28	0.0528	6.47E+00	3.42E-01
6.12	0.0612	7.50E+00	4.59E-01

Appendix 4: Drag coefficient calculations used for the C_D versus Re graphs in Figure 4.6.

A. Schiller Naumann	
Re	C_D ; $C_D = \frac{24}{Re}(1 + 0.15Re^{0.687})$
50	1,538095554
100	1,091731091
150	0,910215334
200	0,805614687
250	0,735362673
300	0,68389794
350	0,64402356
400	0,611896606
450	0,585254147
500	0,562665302
550	0,543174879
600	0,526117392
650	0,511012886
700	0,497505194
750	0,485323596
800	0,474258079
850	0,46414283
900	0,454844909
950	0,446256291
1000	0,43828814

B. Morsi Alexander		Constants for $100 \leq Re < 1000$
Re	C_D; $C_D = \frac{A}{Re} + \frac{B}{Re^2} + C$	
50	1,2198	A = 98,33
100	0,7055	B = -2778
150	0,532066667	C = 0,3644
200	0,4222	
250	0,348872	
300	0,2969	
350	0,258265306	
400	0,2284625	
450	0,204792593	
500	0,185548	
550	0,169598347	
600	0,156166667	
650	0,144701775	
700	0,134802041	
750	0,126168	
800	0,118571875	
850	0,11183737	
900	0,105825926	
950	0,100427147	
1000	0,095552	

C. Universal drag: Viscous region (0 ≤ Reb < 1000)	
Re	C_D; $C_{DVis} = \frac{24}{Re}(1 + 0.1Re^{0.75})$
50	1,382544742
100	0,998946638
150	0,845785703
200	0,758195508
250	0,699568046
300	0,656674739
350	0,623445244
400	0,596656315
450	0,574417783
500	0,555538206
550	0,539224121
600	0,524923721
650	0,51223959
700	0,500877116
750	0,49061254
800	0,481272371
850	0,472719681
900	0,464844713
950	0,457558285
1000	0,450787058

Appendix 5: Predicted turbulence quanties at mid-height position for the column (0.91 m diameter) simulated in Chapter 4.

Turbulent Viscosity (water)

Effective Viscosity (water)

163
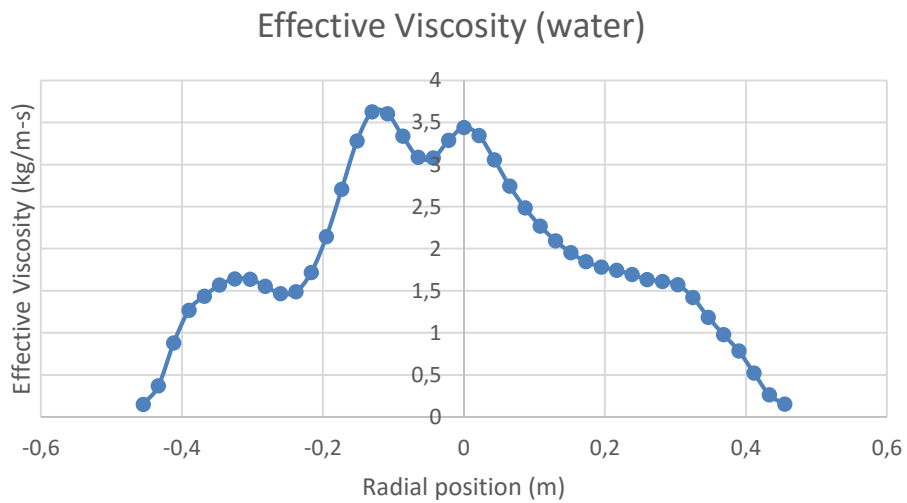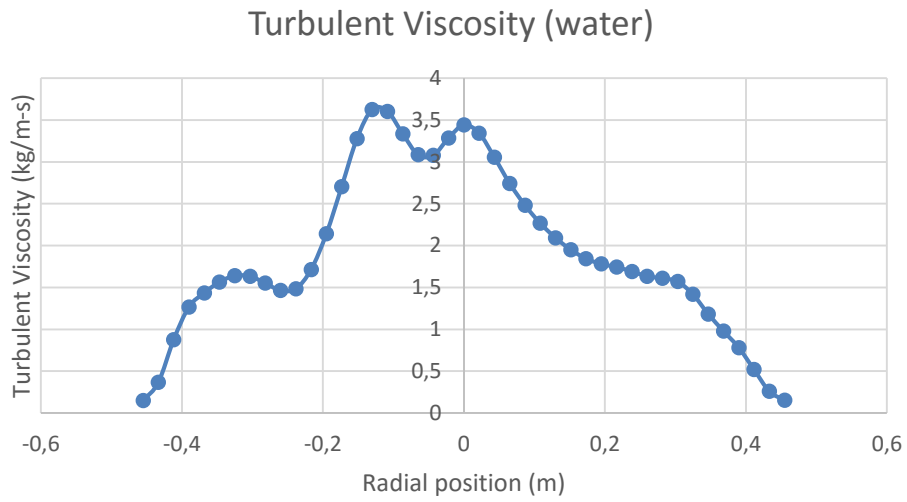
Turbulent Kinetic Energy (water)
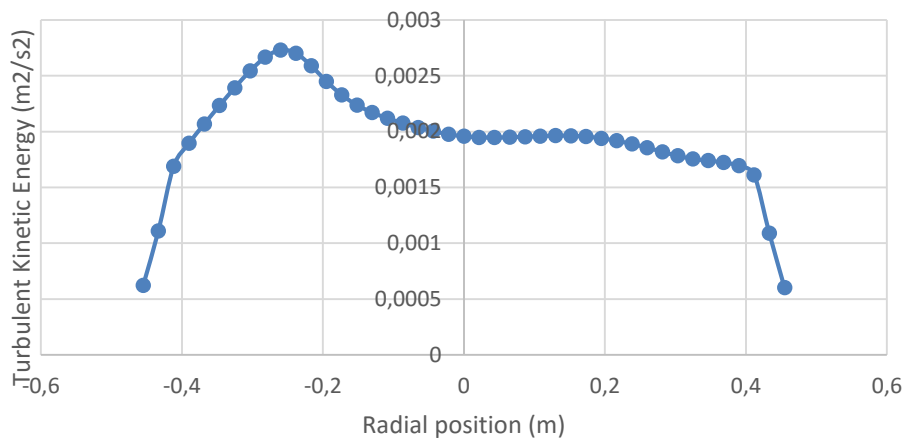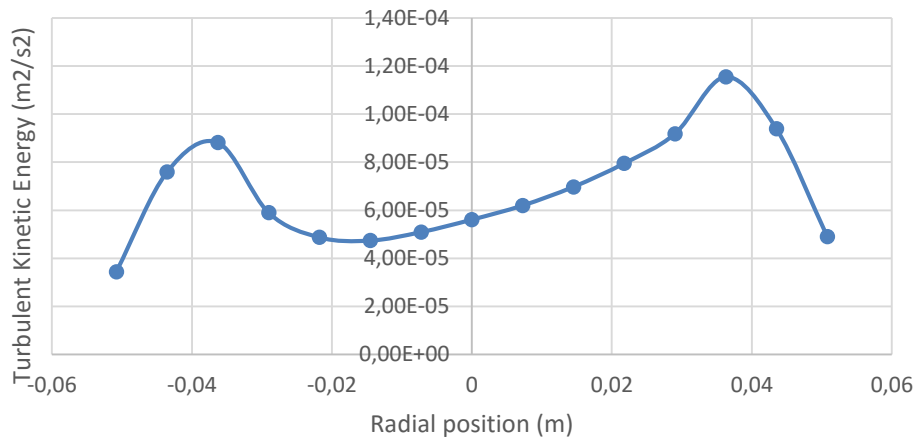

Turbulent Dissipation Rate (water)
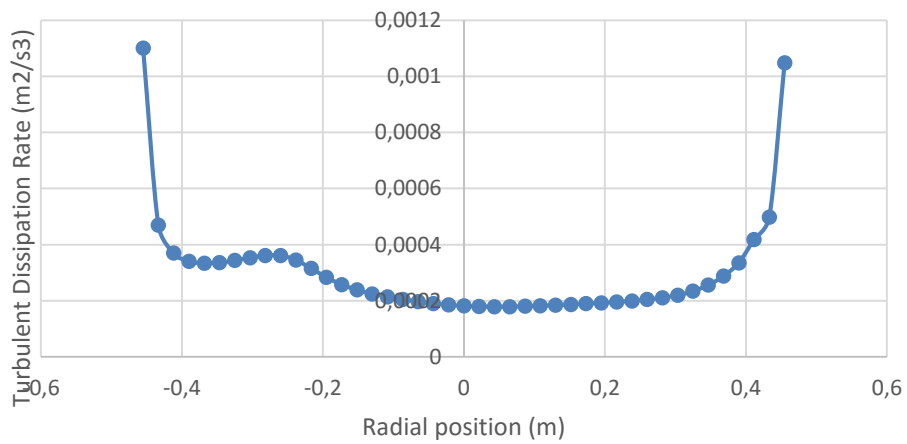
Appendix 6: Some turbulence quantities taken at mid-height position for the column simulated in Chapter 6 for bubbly flow and churn-turbulent flow conditions.
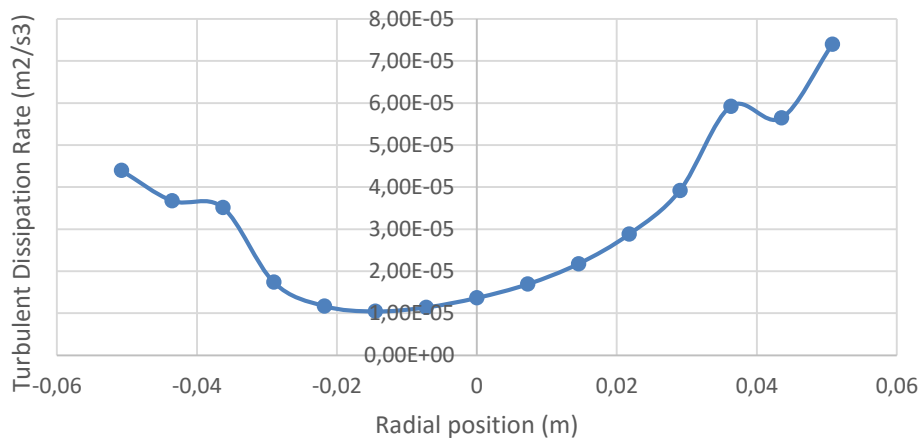
Bubbly flow (J_g = 1.54 cm/s; d_B = 1.5 mm)
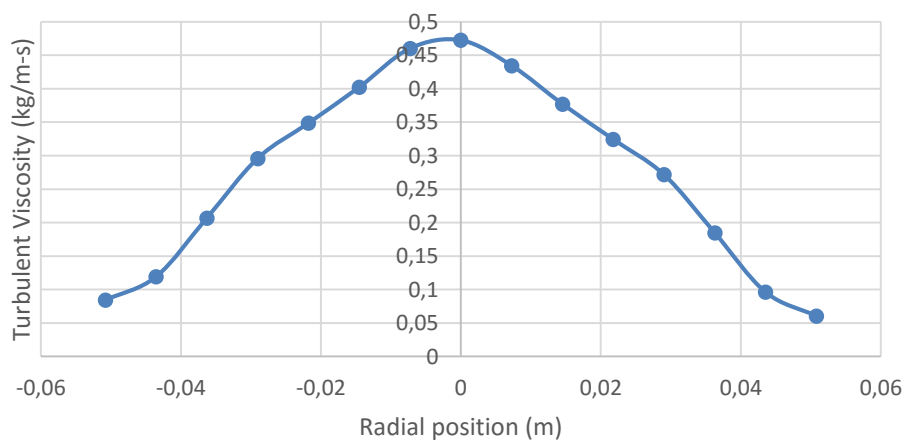
Turbulent viscosity (water)

Effective Viscosity (water)

165
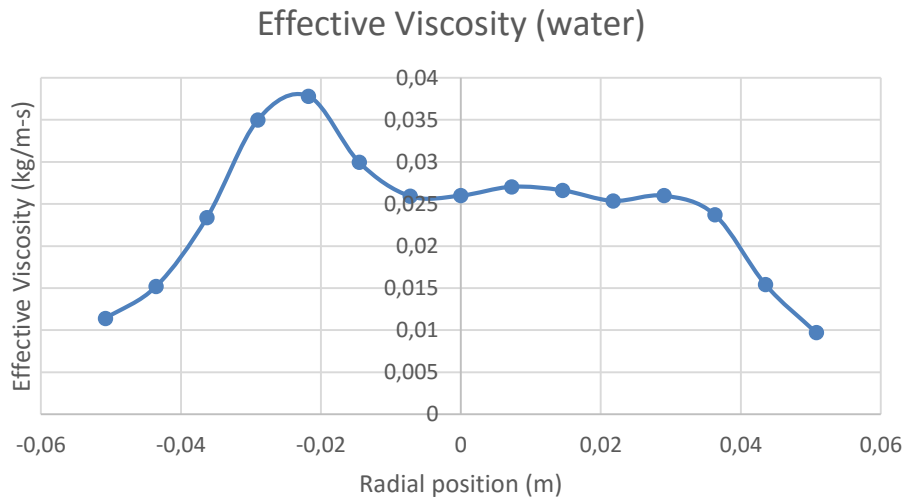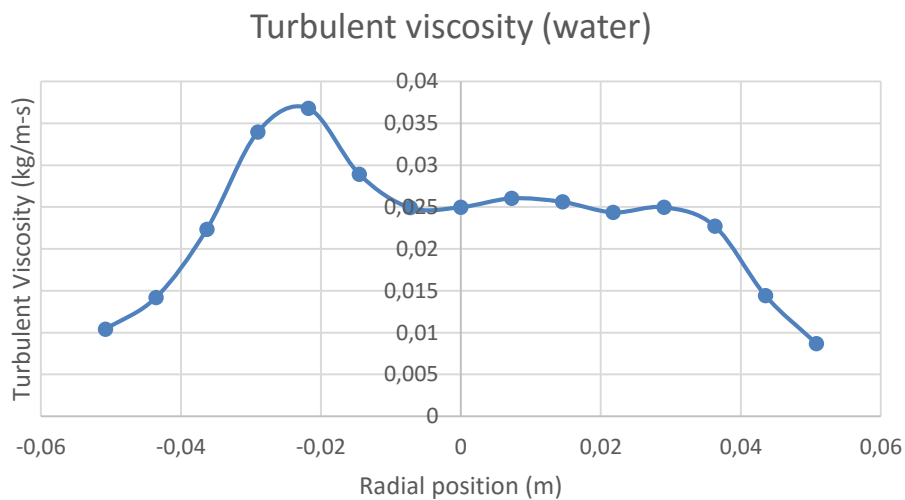
Turbulent Kinetic Energy (water)
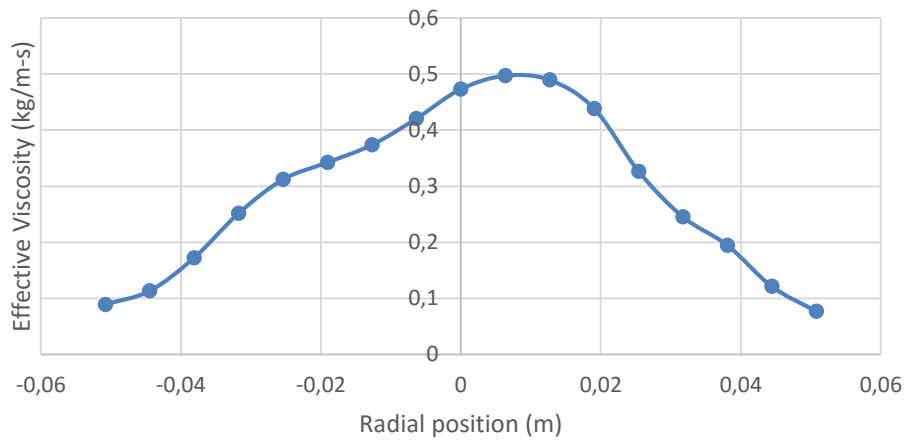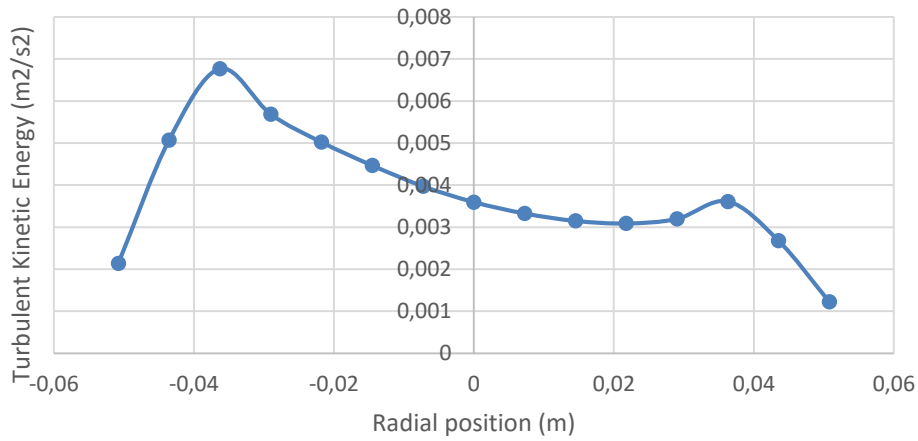

Turbulent dissipation Rate (water)

Churn-turbulent flow (J_g = 5.28 cm/s; d_B = 1.5 mm)

turbulent Viscosity (water)

166

Effective Viscosity (water)

Turbulent Kinetic Energy (water)

Turbulent Dissipation Rate (water)

167